**Title**
DIPOLE MOMENTS OF ALKALI HALIDES BY THE ELECTRIC DEFLECTION METHOD



**Author**
Story, Troy Lee

**Publication Date**
1968-09-01

# University of California

# Ernest O. Lawrence Radiation Laboratory

DIPOLE MOMENTS OF ALKALI HALIDES BY THE ELECTRIC DEFLECTION METHOD

Troy Lee Story, Jr.

(Ph. D. Thesis)

September 1968

## DISCLAIMER

UCRL-18484

UNIVERSITY OF CALIFORNIA

Lawrence Radiation Laboratory
Berkeley, California 94720

AEC Contract No. W-7405-eng-48

# DIPOLE MOMENTS OF ALKALI HALIDES BY THE ELECTRIC DEFLECTION METHOD

Troy Lee Story, Jr.
(Ph.D. Thesis)

September 1968

# DIPOLE MOMENTS OF ALKALI HALIDES BY THE ELECTRIC DEFLECTION METHOD

## Contents

UCRL-18484

# DIPOLE MOMENTS OF ALKALI HALIDES BY THE ELECTRIC DEFLECTION METHOD

Troy Lee Story, Jr.

Lawrence Radiation Laboratory
University of California
Berkeley, California 94720

September 1968

## ABSTRACT

The radio-frequency Stark spectra and the microwave spectra of $^{6}Li^{35}Cl$ and $^{6}Li^{37}Cl$ are investigated by the molecular-beam electric-resonance method of spectroscopy. Observations of transitions of the type $(J,M_J) \rightarrow (J,M_J \pm 1)$ and $(J+1,M_J) \rightarrow (J,M_J)$ have allowed a determination of dipole moments, rotational constants, and chlorine quadrupole and spin-rotation interaction constants for several vibrational states of these molecules.

A method of determining dipole moments by deflecting a beam of velocity selected molecules with an electric field is presented. Dipole moments of KI, RbBr, RbI, CsBr, and CsI have been determined by this method. Deflection analyses of CsOH and $LaF_3$ are carried out, and implications concerning the geometrical configurations of these molecules are given. The design and construction of the velocity selector which was used in the deflection experiments is presented.

# I. INTRODUCTION

During the past 21 years, the molecular-beam electric-resonance (MBER) method of spectroscopy has proved to be a useful tool for the investigation of the radio-frequency Stark spectra of diatomic molecules. Most of the investigations in the past have been focused on obtaining information about the alkali halides since these are most easily studied. At this point, the various investigators using the MBER technique are attempting to expand the horizons of the method to the study of other kinds of systems than alkali halides and a few other molecules, by improving the technology of the method.

In this laboratory, we have, in the past, attempted to obtain very accurate measurements of alkali halide dipole moments.[16] This information has been particularly useful for ascertaining the worth of various ionic models of molecules which attempt to predict reasonable values of molecular constants.[1,2] Part of this thesis presents an accurate determination of the dipole moments of $^{6}Li^{35}Cl$ and $^{6}Li^{37}Cl$ as a continuation of the high-resolution molecular-beam electric-resonance studies of the alkali halides which have been performed in this laboratory.

Due to the complexity of the spectra and beam intensity considerations, five alkali halides, KI, RbBr, RbI, CsBr, and CsI, have eluded analysis by the practitioners of the MBER method. Previous molecular beam experiments have indicated that determining dipole moments by analysis of the deflection characteristics of molecular beams is a viable method.[3,4] This thesis presents the determination

of the dipole moments of KI, RbBr, RbI, CsBr, and CsI by a deflection analysis of velocity selected molecular beams. A deflection analysis of CsOH is presented as an attempt to apply the deflection method to linear triatomic molecules with low bending frequencies. The design and construction of the velocity selector which was used in the deflection experiments, is presented.

Starting with the work of Wharton et al.[5] on $Li_2O$, deflection experiments have been used for qualitative determinations of the geometry of molecules. Some geometry studies have revealed variations in molecular structure within a closely related series of molecules.[5,49,53] This thesis presents a deflection analysis of $LaF_3$. The purpose of this analysis is to obtain qualitative information about the structure of this molecule. Although the electron diffraction work of Akishin et al.[51] indicated that all the La trihalides are planar, the inherent limitations of high-temperature electron diffraction experiments suggested the need for re-examination of the problem by a different method.

# II. THE MOLECULAR BEAM ELECTRIC RESONANCE SPECTRA OF LiCl

## A. Introduction

The molecular beam electric resonance method of spectroscopy allows a study of polar molecules by making use of the deflection properties of molecular beams in inhomogeneous electric fields. The amount of deflection depends on the rotational state, J, and the absolute value of the spatial orientation state, $M_J$. Two inhomogeneous electric fields are arranged to focus a particular $(J,M_J)$ state onto a detector. Between the inhomogeneous fields, a homogeneous Stark field is placed. Transitions of the type $(J,M_J) \rightarrow (J,M_J \pm 1)$ are induced by a radio-frequency field which is perpendicular to the homogeneous field. By application of microwave frequencies at a given radio-frequency, transitions of the type $(J+1,M_J) \rightarrow (J,M_J)$ are induced. Resonances are observed as changes in the beam intensity at the detector.

The dipole moment of a molecule is accurately determined by measuring the transition frequency and the applied electric field. Accurate rotational constants are obtained from measurement of the rotational transition frequencies. The hyperfine structure of the spectrum, which results from the coupling of nuclear and electronic motions, permits a determination of nuclear electric quadrupole interactions, spin-rotation interactions, and magnetic dipole-dipole interactions. These parameters can be measured in several vibrational states.

In this section, spectra of $^{6}Li^{35}Cl$ and $^{6}Li^{37}Cl$ are obtained for the J = 1 rotational level in the first three vibrational states. The

dipole moments, rotational constants, and chlorine quadrupole and spin-rotation interaction constants, are determined.

## B. The Spectrometer

### 1. Theory of Operation

Figure 1 is a diagram of a typical molecular-beam electric-resonance spectrometer. Molecules effuse from the source, move through the apparatus, and strike the detector at the end. In the middle of the apparatus are two inhomogeneous electric fields A and B, and a homogeneous electric field, C. Superimposed upon the C field, at right angles to the C field and molecular beam, are sources of radio-frequency and microwave power. In the inhomogeneous field regions, the molecules experience a force of magnitude

$$F = -(\partial W/\partial E) \cdot (\partial E/\partial X)$$

where $(\partial E/\partial X)$ is the field gradient perpendicular to the direction of the beam, $(\partial W/\partial E)$ is a term which arises due to the Stark effect, and $W$ is the energy of the molecule. Since the interaction of the permanent electric dipole moment, $\mu$, with the electric field, E, removes the $|M_J|$ degeneracy of rotational states by increasing or decreasing the energy of a particular $(J,|M_J|)$ state, then the term $(\partial W/\partial E)$ may be positive or negative. It follows that the force exerted on a molecule may be with or against the field gradient according to the state of space quantization. Figure 2 illustrates the field and rotational

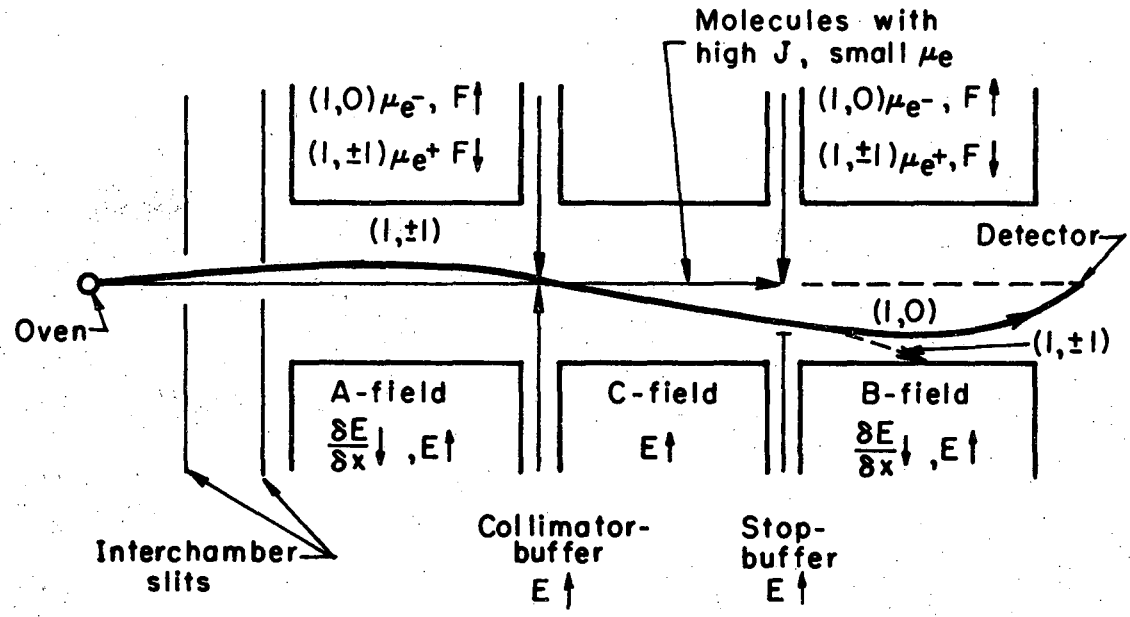


MU-28374-D

Fig. 1. A diagram of a typical molecular-beam electric-resonance spectrometer set-up for doing flop-in experiments.

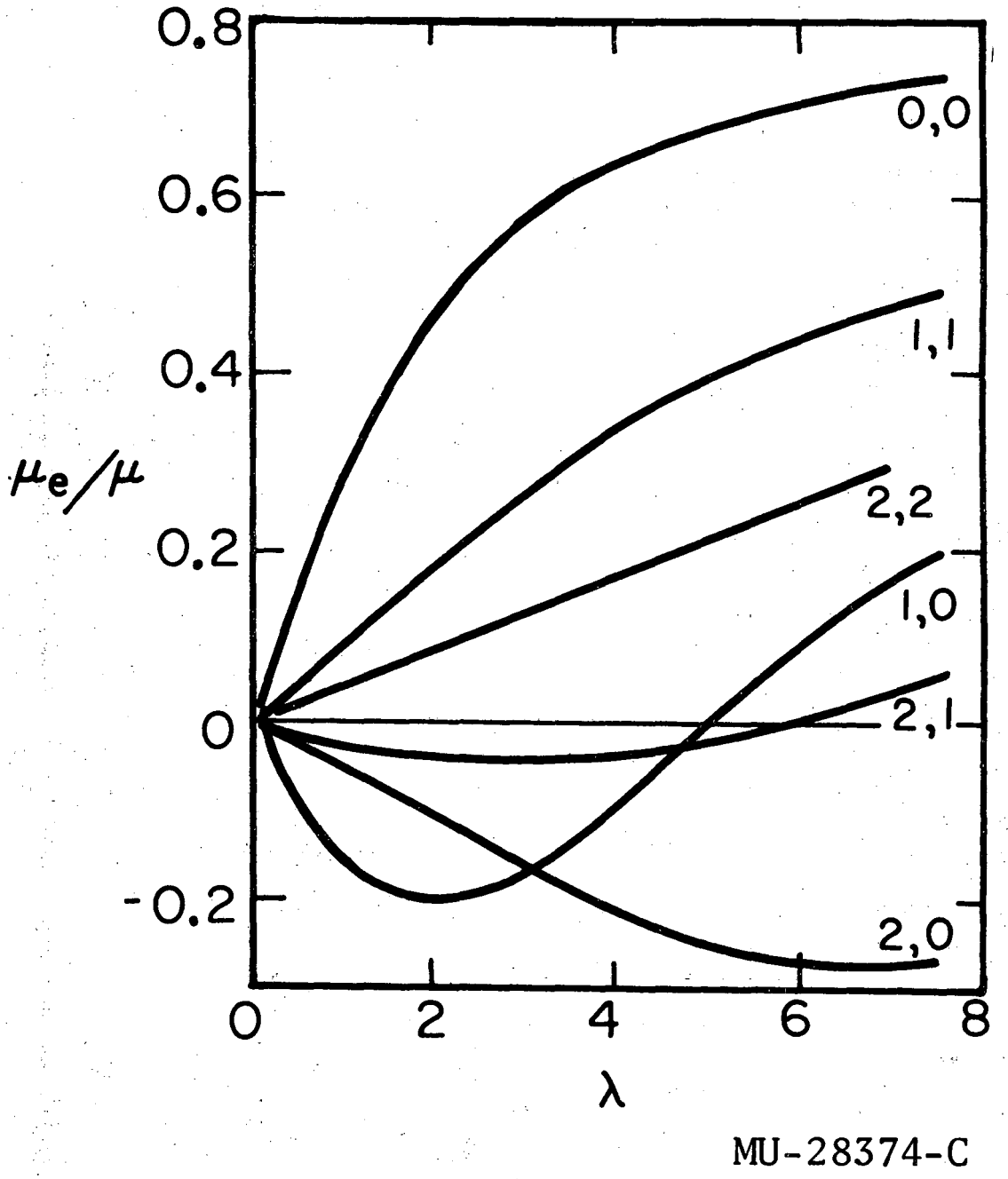


Fig. 2. The effective electric dipole moment, $\mu_e$, for deflection of a diatomic molecule with a permanent dipole moment, $\mu$. The numbers at the right of each curve represent the $(J,|M_J|)$ states. The dimensionless parameter $\lambda$ is equal to $\mu E/B$, where $E$ is the electric field strength and $B$ is the rotational constant.

state dependence of $(\delta W/\delta E)$ with a plot of $\mu_e/\mu$ versus $\lambda$, where

$\mu_e$ = effective dipole moment = $-(\delta W/\delta E)$

$\lambda = \mu E/B$, B = rotational constant .

In the present experiments the A and B fields are arranged to select molecules in the state $(J=1,M_J=\pm 1)$ and refocus molecules in the state $(J=1,M_J=0)$, only if a transition of the type $(J=1,M_J=\pm 1) \rightarrow (J=1,M_J=0)$ has occurred. Therefore, resonances are observed as increases of the beam intensity at the detector. In the absence of hyperfine structure, a single Stark transition would be observed; however, the addition of hyperfine structure splits the $|M_J|$ levels and several transitions are observed. Transitions of the type $(J=1,M_J=0) \rightarrow (J=0,M_J=0)$ are also observed. These are discussed in Section D-3.

## 2. Details of the Spectrometer

Source and Detector. The molecular beam oven is a 20% iridium - 80% platinum tube with a 0.953 cm outer diameter and a 0.0254 cm wall. The oven slit is 0.63 cm high × 0.0127 cm wide. Detection is by surface ionization on a 0.0165 cm wide × 0.00254 cm thick tungsten ribbon. Positive ions are accelerated out of the main chamber, and focused through a mass-analyzing magnet into a 14-stage electron multiplier.

Stark Field. The C field consists of glass optical flats upon which an aluminum film has been evaporated. The electrodes are parallal to 1/8 $\lambda$ of helium light for a 1 cm gap. This corresponds to

an uncertainty of 1 part in $10^5$ along the 25 cm transition region. All components of the earth's magnetic field and fringe magnetic fields from the mass analyzer were reduced to less than 50 milligauss along the C field transition region. The applied voltage is measured with a resistance bridge and a Rubicon potentiometer, in conjunction with an Eppley standard cell. The uncertainty in electric field is 1 part in $10^4$ with a reproducibility of the field of an order of magnitude better.

Radio-frequency and Microwave Equipment. Radio-frequency is applied across one of the C field electrodes. Hewlett-Packard 606A and 608C radio-frequency generators are used to produce signals from 50 kHz to 65 MHz and from 10 MHz to 480 MHz, respectively. Radio-frequency signals are monitored with a H-P 5245L-5253A electronic counter. Pulses from the electron-multiplier, which are a direct measure of beam intensity, are amplified and fed into a H-P 5245L-5253B electronic counter. The radio-frequency count is fed into seven channels of a H-P 562A digital recorder, and the beam intensity is fed into the remaining four channels. In addition, the first three digits of the beam intensity count are converted into a voltage and fed into a Leeds and Northrup chart recorder for graphic representation of the data. One second counts are simultaneously taken of the beam intensity at a fixed radio-frequency, then the frequency is changed, and the counting cycle is restarted.

Microwave power is introduced into the electric field transition region by means of a sectoral horn which is 35.56 cm long and has an apex of 20°. Microwave frequency is obtained by using a Hewlett-Packard

940A frequency doubler with the fundamental frequency generated by a "P band" Varian X-12 klystron. The klystron is phase-locked with a H-P DY 2650 A-M5 oscillator synchronizer to a H-P 608C signal generator. The fundamental frequency is monitored with a H-P 540 B transfer oscillator and a H-P 5245L-5253A frequency counter. Final frequency determinations are made with the 608C signal generator output.

Figure 3 is a schematic diagram of the present apparatus. Further details of the apparatus are given in the thesis of A. J. Hebert,[6] who designed and constructed the spectrometer. The apparatus is now equipped with an improved C field voltage monitoring system and a multichannel analyzer data retrieval system.[55,56]

## C. The Theory

### 1. The Hamiltonian

The Hamiltonian which describes the observable interactions in the electric-resonance spectra of a polar diatomic molecule in a $^1\Sigma$ electronic ground state is[7,8]

$$\mathcal{H} = B\underset{\sim}{J}^2 - \underset{\sim}{\mu}\cdot\underset{\sim}{E} - eq_1Q_1 \frac{3(\underset{\sim}{I}_1\cdot\underset{\sim}{J})^2 + 3/2\,(\underset{\sim}{I}_1\cdot\underset{\sim}{J}) - (\underset{\sim}{I}_1{}^2\,\underset{\sim}{J}^2)}{2I_1(2I_1 - 1)\,(2J - 1)\,(2J + 3)}$$

$$- eq_2Q_2 \frac{3(\underset{\sim}{I}_2\cdot\underset{\sim}{J})^2 + 3/2\,(\underset{\sim}{I}_2\cdot\underset{\sim}{J}) - (\underset{\sim}{I}_2{}^2\,\underset{\sim}{J}^2)}{2I_2(2I_2 - 1)\,(2J - 1)\,(2J + 3)} + c_1(\underset{\sim}{I}_1\cdot\underset{\sim}{J}) + c_2(\underset{\sim}{I}_2\cdot\underset{\sim}{J})$$

$$+ c_3 \frac{3(\underset{\sim}{I}_1\cdot\underset{\sim}{J})\,(\underset{\sim}{I}_2\cdot\underset{\sim}{J}) + 3(\underset{\sim}{I}_2\cdot\underset{\sim}{J})\,(\underset{\sim}{I}_1\cdot\underset{\sim}{J}) - 2(\underset{\sim}{I}_1\underset{\sim}{I}_2)\,J(J + 1)}{(2J - 1)\,(2J + 3)}$$

$$+ c_4\,(\underset{\sim}{I}_1\cdot\underset{\sim}{I}_2)$$

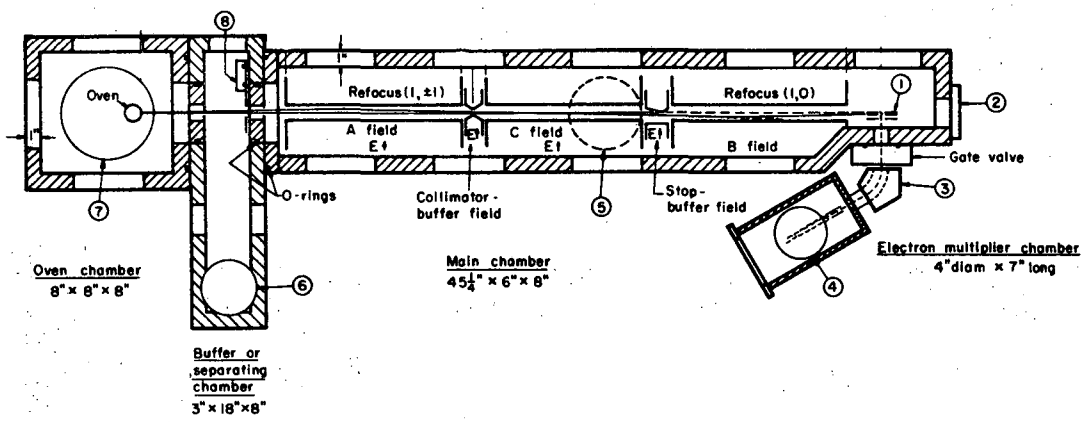


Fig. 3. Schematic diagram (top view) of the electric-resonance apparatus. Field lengths and displacements are to scale. Field gaps and beam displacements are exaggerated. Unshaded areas in chamber walls represent access ports.

1) Hot wire and ion accelerator
2) Glass cover port for optical alignment
3) Permanent magnet, 60°, 1-cm gap
4),5),6), and 7) Outlets to liquid nitrogen traps and oil diffusion pumps
8) Gate valve and beam flag

The first term in the above expression is the observable for the rotational energy of the molecule, where $B$ is the rotational constant and $J$ is the rotational angular momentum operator. The second term gives the interaction of the permanent electric dipole moment, $\mu$, with the applied external electric field, $E$. The remaining terms represent the hyperfine interactions of the molecule, where the subscripts distinguish between the two nuclei with spins $I_1$ and $I_2$. These hyperfine interactions arise from the coupling of nuclear and electronic motions. The interactions of the nuclear electric quadrupole moments, $Q$, with the field gradients at the nuclei, $q$, are given by the third and fourth terms. The fifth and sixth terms represent the interaction of the nuclear magnetic moments with the magnetic fields at the nuclei that arise from molecular rotation. The seventh and eighth terms represent the tensor and scalar components of the spin-spin interaction, respectively.

## 2. Energy Calculations

A computer program was used to calculate the matrix elements of $\mathcal{H}$ in a $(J, I_1, I_2, M_J, M_{I_1}, M_{I_2})$ representation, where $M_J$, $M_{I_1}$, $M_{I_2}$, are the projections of $J$, $I_1$, and $I_2$, respectively, on the direction of the electric field $E$.[9] The program computes the energy eigenvalues, spectral line positions, and relative intensities according to the selection rule $\Delta M_F = 0, \pm 1, \pm 2, \ldots$, where $M_F$ is the projection of the total angular momentum on the direction of the electric field. Since $M_F$ is a good quantum number at all values of the field strength, the

matrix is diagonal in $M_F$. The input to the computer program are coupling constants, which are varied to obtain a best fit to the observed spectra.

The first term in the Hamiltonian is diagonal in J. The last four terms are small, and only matrix elements diagonal in J are included for them. The non-zero matrix elements of the Stark interaction are of the form $(J,M_J|\mu\cdot E|J\pm1,M_J)$. Since the matrix is infinite in J, only the first four J states are included in the matrix for J = 1 calculations, only the first five J states for J = 2 calculations and similarly for higher J state calculations. This procedure is better than a fourth-order perturbation treatment of the problem. The quadrupole terms have matrix elements diagonal in J and also elements connecting J with J + 2. The quadrupole operator in the Hamiltonian given above can be used only to calculate matrix elements diagonal in J. Formulae derived by Fano were used to calculate the off-diagonal matrix elements for the quadrupole operator. This procedure is better than a second-order perturbation treatment of the quadrupole interaction energy. The line intensities are calculated from the matrix elements of the dipole moment operator using the computed wave functions.

## D. The Spectra

### 1. Introduction

Radio-frequency and microwave spectra of $^6Li^{35}Cl$ and $^6Li^{37}Cl$ have been measured by the molecular-beam electric-resonance method. This investigation was concerned with radio-frequency transitions of the type $(J=1,M_J=\pm1) \rightarrow (J=1,M_J=0)$ and microwave transitions of the

type $J=1 \rightarrow J=0$, where $J$ is the rotational angular momentum quantum number and $M_J$ is the projection of $J$ on the direction of the electric field. Values were obtained for the electric dipole moment, the chlorine quadrupole interaction constant, and the chlorine spin-rotation interaction constant, in the first three vibrational states of $^6Li^{35}Cl$ and $^6Li^{37}Cl$. Microwave spectra of $^6LiCl$ were obtained for the first time. Observations of rotational transitions in the $v = 0$, 1, and 2 vibrational states of $^6Li^{35}Cl$ and the $v = 0$ vibrational state of $^6Li^{37}Cl$, in conjunction with the $\omega_e$ and $\omega_e x_e$ values reported by Klemperer et al.,[10] allowed a determination of the Dunham coefficients $Y_{01}$, $Y_{11}$, and $Y_{21}$.[11]

Prior to the present work, radio-frequency spectra of $^6Li^{35}Cl$ and $^6Li^{37}Cl$ were observed with a molecular-beam electric-resonance spectrometer by Marple and Trischka.[12] In addition, Lide, Cahill, and Gold[13] have used conventional microwave methods to obtain molecular constants for $^7Li^{35}Cl$ and $^7Li^{37}Cl$. Klemperer et al.[10] have reported the results of an infrared analysis of $^7LiCl$.

The present $^6LiCl$ microwave results agree with the previous $^7LiCl$ results of Lide, Cahill, and Gold when appropriate isotope corrections are made. Although the hyperfine constants agree with the values reported by Marple and Trischka, the dipole moments are significantly higher than theirs.

2. Radio-frequency Spectra

The $(J=1, M_J=\pm 1) \rightarrow (J=1, M_J=0)$ radio-frequency transitions were obtained at a field strength of 400 volts/cm. The spectrum for a given vibrational state consists of six major lines, as predicted by the following selection rules:

$$\Delta J = 0$$
$$\Delta M_F = 0, \pm 1, \pm 2, \ldots$$

where $M_F = M_J + M_{I_1} + M_{I_2}$, and $M_I$ is the projection of the nuclear spin, I, on the direction of the electric field. $I_1$ refers to the lithium nucleus and $I_2$ refers to the chlorine nucleus. All of the observed lines were of approximately equal intensity.

The nuclear quadrupole and spin-rotation interactions of the chlorine nucleus alone were adequate for the interpretation of the radio-frequency observations. The present signal-to-noise ratios, and line widths of 4.5 kHz, prevented the resolution of splittings and small line shifts which are expected to arise from the much smaller hyperfine interactions of the $^6$Li nucleus. The $^6$Li quadrupole interaction constant was calculated from the ratio $Q^6Li/Q^7Li$ given by Hollowell[1] and the value of $(eqQ)^7Li$ given by Gold[14] to be 5.13 kHz. This interaction is expected to cause line splittings of the order of 2 kHz in each of the observed 6 major lines. The $^6$Li spin-rotation interaction is expected to cause even smaller effects which are also unresolved. The calculated value of the magnetic dipole-dipole interaction constant[15] is approximately 42 Hz for $^6Li^{35}Cl$. Initial calculations indicated that the effect

of this term is negligible and it has not been used in the subsequent calculations. Figure 4 is an energy level diagram for $^{6}$LiCl showing the observed transitions.

The full-width at half-maximum intensity of the radio-frequency lines was approximately 4.5 kHz and the signal-to-noise ratio was approximately 20 to 1 for the v = 0 vibrational state of $^{6}Li^{35}Cl$. This indicates a line position uncertainty of 0.23 kHz.

### 3. Microwave Spectra

The $J=1 \rightarrow J=0$ microwave transitions were observed by setting the Stark field and radio-frequency to give a maximum signal for a prominent line in the reorientation spectrum, i.e., a $(J=1,M_J=\pm1) \rightarrow (J=1,M_J=0)$ transition. The microwave frequency was then swept and the resonant frequency was observed as a decrease in the radio-frequency "flop in" signal due to a depletion of the final state by rotational transitions of the type $(J=1,M_J=0) \rightarrow (J=0,M_J=0)$. The "flop in" Stark signal decreased by approximately 50%, and the line full-widths at half-maximum intensity were about 70 kHz at transition frequencies near 48 GHz.

## E. Results and Discussion

### 1. Radio-frequency Data

Tables I and II list the observed and calculated line frequencies at an electric field strength of 400 volts/cm. No experimental line frequencies are given in cases where lines from different vibrational states overlapped considerably, or when the line was not satisfactorily

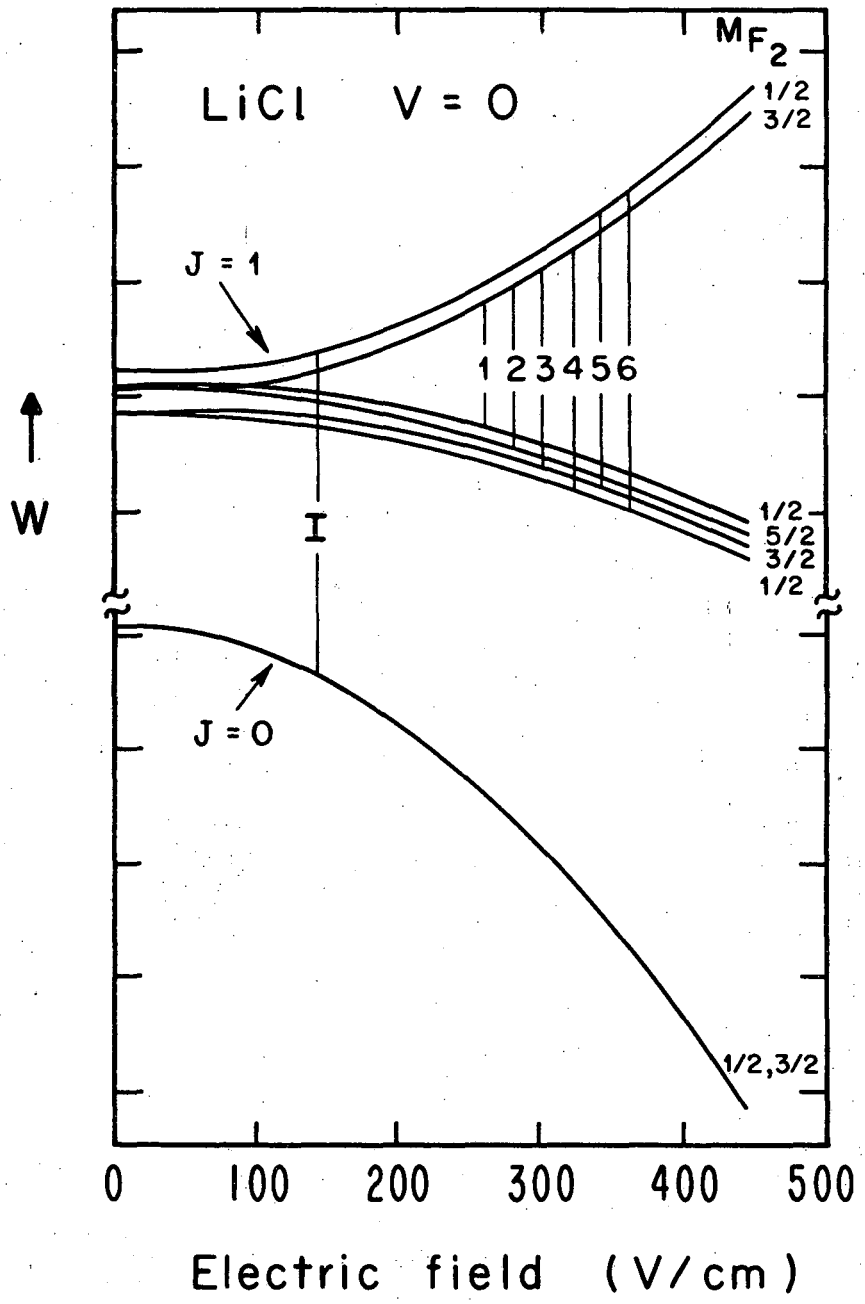


XBL689-3875

Fig. 4. The energy levels of $^{6}Li^{35}Cl$ with respect to electric field strength. Arabic numerals refer to observed radio-frequency transitions. The Roman numeral refers to the observed microwave transition. $M_{F_2} = M_J + M_{I_2}$

Table I. Observed and calculated line positions for the radio-frequency spectra of $^{6}Li^{35}Cl$. All values are given in kHz.

| Line No. | Observed | Calculated | Differences |
|---|---|---|---|
| | $(1,\pm1) \rightarrow (1,0)$, $v = 0$, $E_c = 400$ V/cm | | |
| 1 | 12054.09±0.21 | 12054.07 | -0.02 |
| 2 | 12441.22±0.19 | 12441.23 | +0.01 |
| 3 | 12667.51±0.21 | 12667.55 | +0.04 |
| 4 | 13157.93±0.25 | 13157.93 | 0.00 |
| 5 | 13375.39±0.20 | 13375.49 | +0.10 |
| 6 | 13771.51±0.06 | 13771.42 | -0.09 |
| | $(1,\pm1) \rightarrow (1,0)$, $v = 1$, $E_c = 400$ V/cm | | |
| 1 | 12425.41±0.24 | 12425.42 | +0.01 |
| 2 | 12864.11±0.02 | 12864.08 | -0.03 |
| 3 | 13120.17±0.18 | 13120.05 | -0.12 |
| 4 | 13674.79±0.38 | 13675.07 | +0.28 |
| 5 | 13922.70±0.26 | 13922.70 | 0.00 |
| 6 | 14369.71±0.14 | 14369.70 | -0.01 |
| | $(1,\pm1) \rightarrow (1,0)$, $v = 2$, $E_c = 400$ V/cm | | |
| 1 | ---- | 12818.75 | ---- |
| 2 | 13307.05±0.31 | 13307.05 | 0.00 |
| 3 | 13592.24±0.13 | 13592.03 | -0.21 |
| 4 | 14209.43±0.24 | 14209.67 | +0.24 |
| 5 | 14486.47±0.92 | 14486.42 | -0.05 |
| 6 | 14982.95±0.18 | 14982.95 | 0.00 |

Table II. Observed and calculated line positions for the radio-frequency spectra of $^{6}Li^{37}Cl$. All values are given in kHz.

| Line No. | Observed | Calculated | Differences |
|---|---|---|---|
| | $(1,\pm1) \rightarrow (1,0)$, v = 0, $E_C$ = 400 V/cm | | |
| 1 | 12330.76±0.11 | 12330.79 | +0.03 |
| 2 | 12637.32±0.33 | 12637.31 | -0.01 |
| 3 | 12814.47±0.25 | 12814.36 | -0.11 |
| 4 | 13201.23±0.12 | 13201.23 | 0.00 |
| 5 | ---- | 13371.59 | ---- |
| 6 | 13684.78±0.34 | 13684.79 | +0.01 |
| | $(1,\pm1) \rightarrow (1,0)$, v = 1, $E_C$ = 400 V/cm | | |
| 1 | 12727.12±0.16 | 12727.12 | 0.00 |
| 2 | 13073.97±0.11 | 13073.97 | 0.00 |
| 3 | 13274.22±0.43 | 13274.31 | +0.09 |
| 4 | 13712.21±0.28 | 13711.98 | -0.23 |
| 5 | 13905.70±0.35 | 13905.44 | +0.26 |
| 6 | 14259.17±0.17 | 14259.17 | 0.00 |
| | $(1,\pm1) \rightarrow (1,0)$, v = 2, $E_C$ = 399.958 V/cm | | |
| 1 | ---- | 13141.18 | ---- |
| 2 | 13527.8 ±0.4 | 13527.79 | -0.01 |
| 3 | 13750.7 ±0.1 | 13750.73 | +0.03 |
| 4 | ---- | 14238.15 | ---- |
| 5 | 14455.8 ±0.4 | 14454.46 | -1.34 |
| 6 | 14847.7 ±0.9 | 14847.70 | 0.00 |

observed. The molecular constants which give a best fit to the spectra are listed in Tables III and IV.

The dipole moments were found to fit quadratic expressions for the variation of the dipole moment with vibrational state. Dipole moments and derived expressions are given in Table III along with the previous values reported by Marple and Trischka.[12] The present dipole moments are significantly higher and are expected to be accurate to ±1 part in $10^4$ and reproducible to an order of magnitude better. Previous determinations of the dipole moments of alkali halides by Street et al.,[16] using the same apparatus, are in good agreement with those of other investigators.[16,17]

Table IV lists the values of $(eqQ)_{Cl}$ and $c_{Cl}$ for $^6$LiCl in the v = 0, 1, and 2 vibrational states. These values are in agreement with those of Marple and Trischka[12] within the combined experimental errors. The internal consistency of the data is made evident by the negligible variation of the ratio

$$(eqQ)_{Cl^{35}}/(eqQ)_{Cl^{37}}$$

for different vibrational states, when it is corrected to a common vibrational energy. The average ratio is

$$\left[(eqQ)_{Cl^{35}}\right]/\left[(eqQ)_{Cl^{37}}\right] = 1.2643 \pm 0.0021$$

This ratio is in agreement with the more precise determinations by Wang et al.[19] Table IV also gives values of the coefficients in the following expression for the variation of the quadrupole interaction constants with vibrational state:

$$(eqQ)_v = (eqQ)_e + (eqQ)_I (v+1/2) + (eqQ)_{II} (v+1/2)^2$$

The function given by Marple and Trischka[20] is incorrectly calculated, but when corrected, it agrees with the present results.

2. Microwave Data

The observed microwave transition frequencies were corrected to zero field frequencies in the absence of hyperfine interactions, with the molecular constants obtained from analysis of the radio-frequency Stark spectra. Table V lists the observed transition frequencies, $\nu$, the Stark and hyperfine corrections, and the zero-field transition frequencies, $\nu_o$.

Centrifugal distortion constants for a given vibrational state, $D_v$, were calculated from the results of Klemperer et al. The following equation was then used to determine the Dunham coefficients, $Y_{01}$, $Y_{11}$, and $Y_{21}$:

$$\nu_o = 2Y_{01} + 2Y_{11} (v+1/2) + 2Y_{21} (v+1/2)^2 - 4D_v$$

Table VI lists values of $B_e$, $Y_{01}$, $Y_{11}$, $Y_{21}$, and $B_v$ for $^6Li^{35}Cl$ and $B_o$ for $^6Li^{37}Cl$. Spectroscopic constants for $^7LiCl$ were calculated from the present $^6LiCl$ results and are compared with the results of Lide, Cahill, and Gold in Table VII. The agreement is excellent.

Table III. Dipole moments and dipole moment functions for $^{6}LiCl$. All values are in Debye units.

| | Present Results[a] | Marple and Trischka[b] |
|---|---|---|
| $^{6}Li^{35}Cl$ | ---Dipole Moments--- | |
| $\mu_o$ | 7.12887±0.00005 | 7.1195±0.0006 |
| $\mu_1$ | 7.21683±0.00006 | 7.2069±0.0008 |
| $\mu_2$ | 7.30591±0.00010 | 7.2964±0.0012 |
| $^{6}Li^{37}Cl$ | | |
| $\mu_o$ | 7.12866±0.00006 | 7.1192±0.0008 |
| $\mu_1$ | 7.21627±0.00007 | 7.2071±0.0012 |
| $\mu_2$ | 7.30516±0.00012 | 7.2972±0.0014 |
| | ---Dipole Moment Functions--- | |
| | $\mu_v = \mu_e + \mu_I (v+1/2) + \mu_{II} (v+1/2)^2$ | |
| $^{6}Li^{35}Cl$ | | |
| $\mu_e$ | 7.08532±0.00128 | 7.0766±0.0034 |
| $\mu_I$ | 0.08683±0.00039 | 0.0853±0.0048 |
| $\mu_{II}$ | 0.00056±0.00014 | 0.0011±0.0017 |
| $^{6}Li^{37}Cl$ | | |
| $\mu_e$ | 7.08533±0.00133 | 7.0761±0.0047 |
| $\mu_I$ | 0.08635±0.00045 | 0.0857±0.0066 |
| $\mu_{II}$ | 0.00064±0.00016 | 0.0011±0.0023 |

[a] All dipole moments have an uncertainty of ±0.001 Debye due to an uncertainty in the absolute value of the electric field. The listed uncertainties correspond to the observed precision.

[b] An additional systematic error of ±0.0022 Debye is given in Ref. 4. The coefficients listed were derived from the dipole moment data.

Table IV. Chlorine quadrupole-coupling constants, $(eqQ)_v$, and spin-rotation constants, $(c_{Cl})_v$, for $^6LiCl$.

| | $^6Li^{35}Cl$ | | $^6Li^{37}Cl$ | |
|---|---|---|---|---|
| v | $(eqQ)_{Cl}$ (kHz) | $c_{Cl}$ (kHz) | $(eqQ)_{Cl}$ (kHz) | $c_{Cl}$ (kHz) |
| 0 | -3072.12±1.1 | 2.34±0.19 | -2420.81±1.4 | 1.75±0.23 |
| 1 | -3478.69±1.2 | 2.26±0.20 | -2739.56±1.5 | 1.82±0.25 |
| 2 | -3872.86±2.1 | 2.26±0.36 | -3051.90±2.7 | 1.77±0.45 |

$$(eqQ) = (eqQ)_e + (eqQ)_I\,(v+1/2) + (eqQ)_{II}\,(v+1/2)^2$$

| | $^6Li^{35}Cl$ | $^6Li^{37}Cl$ |
|---|---|---|
| $(eqQ)_e$ | -2864.18±2.8 | -2259.03±3.6 |
| $(eqQ)_I$ | - 418.98±3.3 | - 325.16±4.3 |
| $(eqQ)_{II}$ | 6.20±2.1 | 3.21±2.6 |

Table V. Observed microwave transition frequencies and corrections for $^{6}LiCl$ at E = 50 V/cm.

| Vibrational state | Observed transition frequencies $\nu$(MHz) | J=1 and J=0 Stark shift and hyperfine corrections (MHz) | Zero field frequencies $\nu_o$(MHz) |
|---|---|---|---|
| | ---$^{6}Li^{35}Cl$--- | | |
| 0 | 47942.646±0.006 | 1.0014 | 47941.645±0.006 |
| 1 | 47365.425±0.006 | 1.1107 | 47364.314±0.006 |
| 2 | 46794.384±0.012 | 1.2174 | 46793.167±0.012 |
| | ---$^{6}Li^{37}Cl$--- | | |
| 0 | 47563.554±0.011 | 0.8464 | 47562.708±0.011 |

Table VI. Spectroscopic constants of $^{6}$LiCl. All values are in MHz.

| | |
|---|---|
| $^{6}Li^{35}Cl$ | |
| $B_e$ | 24116.74 ±0.30 |
| $Y_{01}$ | 24116.582±0.033 |
| $Y_{11}$ ($\approx -\alpha_e$) | -291.760±0.045 |
| $Y_{21}$ ($\approx \gamma_e$) | 1.546±0.016 |
| $B_o$ | 23971.088±0.006 |
| $B_1$ | 23682.420±0.007 |
| $B_2$ | 23396.844±0.012 |
| $^{6}Li^{37}Cl$ | |
| $B_o$ | 23781.615±0.009 |

Table VII. Spectroscopic constants of $^{7}LiCl$. All values are in MHz.

| | Lide, Cahill, and Gold[4] | Data calculated[a] from present $^{6}Li^{35}Cl$ results |
|---|---|---|
| | $^{7}Li^{35}Cl$ | |
| $B_e$ | ---- | 21181.27±0.30 |
| $Y_{01}$ ($\approx B_e$) | 21181.1±0.1 | 21181.15±0.03 |
| $-Y_{11}$ ($\approx \alpha_e$) | 240.2±0.2 | 240.15±0.04 |
| $Y_{21}$ ($\approx \gamma_e$) | 1.2±0.2 | 1.19±0.01 |
| | $^{7}Li^{37}Cl$ | |
| $B_e$ | ---- | 20990.05±0.30 |
| $Y_{01}$ ($\approx B_e$) | 20989.9±0.1 | 20989.87±0.003 |
| $-Y_{11}$ ($\approx \alpha_e$) | 236.9±0.2 | 236.90±0.04 |
| $Y_{21}$ ($\approx \gamma_e$) | ---- | 1.17±0.01 |

[a] For comparison with previous LiCl results, the present $^{6}Li^{35}Cl$ measurements were corrected for isotope effects. The atomic masses used were $^{6}Li$ = 6.01513, $^{7}Li$ = 7.01601, $^{35}Cl$ = 34.96885, and $^{37}Cl$ = 36.96590.

# III. VELOCITY DISTRIBUTIONS

## A. Introduction

It has been verified experimentally, that particles at thermal equilibrium inside an isothermal enclosure possess a Maxwellian distribution of velocities.[21,22] In addition, if the aperture of the enclosure imposes effusive flow upon the emerging vapor, the Maxwellian $v^2$ distribution becomes a $v^3$ distribution in the beam. Verification of the Maxwellian $v^2$ distribution can be achieved by velocity selecting a single component beam and measuring the resulting particle intensity. In order that an experiment of this kind be conclusive, the experimental velocity at the maximum intensity must be in close agreement with the most probable velocity calculated from the temperature of the effusive source.

In this section, the design and construction of a molecular beam source, and a slotted disk velocity selector are given. Velocity distributions have been obtained for CsCl and RbCl in order to verify that the molecular beam oven and velocity selector give results as predicted by kinetic theory.

## B. The Molecular Beam Source

### 1. Design Principles

The design and construction of a suitable molecular beam source must be an important part of this work if the results of the experiments performed with the velocity selector are to be conclusive.[21,23]

If a gas is in thermal equilibrium within an isothermal enclosure, the number of particles with velocities in the interval $\nu$ to $\nu + d\nu$ is given by the Maxwell distribution law.

$$N = (4N/\pi^{1/2})(\nu^2/\alpha^3) \exp(-\nu^2/\alpha^2)\, d\nu \qquad (1)$$

where $\alpha = (2kT/m)^{1/2}$, the most probable velocity inside a volume of gas, $k$ is the Boltzman constant, $T$ is the absolute temperature, and $m$ is the mass of the particle. In order that the distribution law be adhered to, the molecular beam oven must be essentially an isothermal enclosure so that the particles within can come to equilibrium at some constant temperature. In order to form a molecular beam which is characteristic of the distribution inside the enclosure, the aperture in the oven must be so small that the thermal equilibrium which exists inside the enclosure, is not affected by the particle flow through the aperture. In addition, the thickness of the aperture must be small compared to the mean free path of the particles. If this latter condition is not fulfilled, the particles would suffer collisions in the neighborhood of the aperture and a cloud formation would result on the exterior of the aperture. This effect would increase the beam width and upset the spatial and velocity distributions which are characteristic of the enclosure. Hence, the following three conditions must exist in order that there be ideal effusion: 1) thermal equilibrium inside the enclosure containing the sample, 2) an aperture so small that this thermal equilibrium is not affected

by the particle flow, and 3) an aperture thickness much smaller than the mean free path of the particles.

Kinetic theory considerations give us some idea of the magnitude of the oven dimensions for ideal effusive flow.[24] Consider a system at dynamic equilibrium within an isothermal enclosure. The number of particles which escape from the condensed phase per unit time is equal to the number which are condensing and this number depends only on the temperature of the system. When the vapor pressure is low, the rate of evaporation does not depend on the presence of a vapor phase above the condensed phase. Hence, it is possible to calculate the rate of evaporation from an isothermal enclosure into a vacuum with the assumption of dynamic equilibrium.

According to the kinetic theory of gases, when the conditions are those described for ideal effusion, the number of particles per unit time, $dN$, which escape from the source slit into a vacuum within the solid angle $d\omega$ at angle $\theta$ relative to the plane containing the slit jaws is

$$dN = (d\omega/4\pi)\, A_s n\bar{\nu} \cos\theta$$

where $n$ is the number of particles per unit volume, $\bar{\nu}$ is the mean particle velocity inside the source, and $A_s$ is the area of the source slit. The total number $N$ of molecules which emerge from the source in all directions is

$$N = \int_0^{\pi/2} (nA_s\bar{\nu}/4\pi)\, 2\pi \sin\theta \cos\theta\, d\theta = nA_s\bar{\nu}/4$$

The mass $G$ of the total number of molecules escaping from a unit surface area per unit time is

$$G = (1/4)\rho\bar{\nu} \tag{2}$$

where $\rho$ is the density of the vapor. According to the ideal gas law,

$$pV = nRT = GRT/M$$

where $M$ is the molecular weight. Therefore,

$$G/V = pM/RT = \rho \tag{3}$$

Observe now that since

$$p = (1/3)\, nm\nu^2 = (1/3)\rho\nu^2$$

where $m$ is the mass of the molecule and $\nu$ is the root mean square velocity, and since

$$\bar{\nu} = \nu(8/3\pi)^{1/2}$$

it follows that

$$\bar{\nu} = (8p/\pi\rho)^{1/2} = (8RT/M\pi)^{1/2} \tag{4}$$

From Eqs. (2), (3), and (4), we obtain $G = p(M/2RT\pi)^{1/2}$ = the mass of sample escaping through the slit per unit surface area per unit time.

Since the above expression holds only when there are no obstacles to dynamic equilibrium and when there is effusive particle flow, consider the following expressions:

1) $G^{I} = K\ p\ A_s\ (M/2RT\pi)^{1/2}$

= the mass of sample escaping through the slit per unit time

where $K$ is Clausing's factor and takes into account the possibility that not every particle which strikes the slit area passes through it. This is due to finite slit thickness.

2) $G^{II} = K\ p_m\ A_s\ (M/2RT\pi)^{1/2}$

= the mass of sample escaping through the slit per unit time with measured vapor pressure $p_m$

3) $G^{III} = S\ p\ (M/2RT\pi)^{1/2}$

= the mass of sample condensing per unit time on the surface of the material of cross-sectional area $S$ within the oven, at the equilibrium vapor pressure $p$

where $\alpha = \dfrac{\text{the measured rate of evaporation in vacuum}}{\text{the hypothetical rate of evaporation calculated at } p}$

= Langmuir coefficient of evaporation (condensation)

$\alpha$ takes into account obstacles to evaporation.

4) $G^{IV} = \alpha S p_m (M/2RT\pi)^{1/2}$

= the mass of sample condensing per unit time on the surface of the material of cross-sectional area S within the oven, at the measured vapor pressure $p_m$

The difference in the measured vapor pressure $p_m$ and the equilibrium vapor pressure $p$ depends on the ratio of the area from which evaporation takes place to the aperture area, and indicates the degree to which the opening in the oven disturbs the dynamic equilibrium. The actual mass of the sample escaping from the oven through the slit is given by

$$G^{II} = G^{III} - G^{IV} = \alpha (p-p_m)(M/2RT\pi)^{1/2}$$

Hence, $A_s K p_m = \alpha S (p-p_m)$

and $$p/p_m = 1 + A_s K/\alpha S \qquad (5)$$

Therefore, if the measured vapor pressure (vapor pressure of the beam) is to differ from the equilibrium vapor pressure (vapor pressure in the sample chamber) by less than 1% it is necessary that the area of the slit opening be 100 times less than the cross-sectional area of the sample chamber. This condition assumes that $\alpha \simeq 1$ and that the slit thickness is much smaller than the mean-free path of the particles. A more precise formulation of Eq. (5) is given by Whitman,[25,26] who used probability theory. However, the Whitman equations are inconvenient and Eq. (5) can be used for most practical purposes.

The present oven design is based upon the above conclusions. For ideal effusion, 1) the ratio of the cross-sectional area of the sample well to the area of the slit opening is of the order of 400 to insure thermal equilibrium, and 2) the slit thickness is much smaller than the mean-free path of the particles studied.

## 2. Construction of the Oven

In order to obtain stable molecular beams, the oven material must be inert with respect to the beam material and have a low vapor pressure at the operating temperature. Since several kinds of solids were to be used in the ovens, it was necessary to construct ovens of two different metals. Stainless steel ovens and slits were used for all the alkali halides, and silver ovens and slits were used for CsOH. A schematic diagram of the oven is given in Fig. 5.

The front face of the oven, the top part of the oven well, and the oven plug, were lapped to prevent leakage of beam material with resulting fluctuation in beam intensity. In order to prevent clogging of the slit due to oven bursts and initial outgassing of the sample, it was desirable to maintain the front part of the oven at a slightly higher temperature than the well containing the sample. To allow this preferential heating, the front part of the oven contains most of the 15 heater coils shown in Fig. 5, and an undercut. The heater coils are wound from 20 mil tantalum wire and are insulated from the oven with alumina tubes. Power is supplied to the heater coils by a 15-ampere Variac which operates from a 115-volt AC regulated line supply.

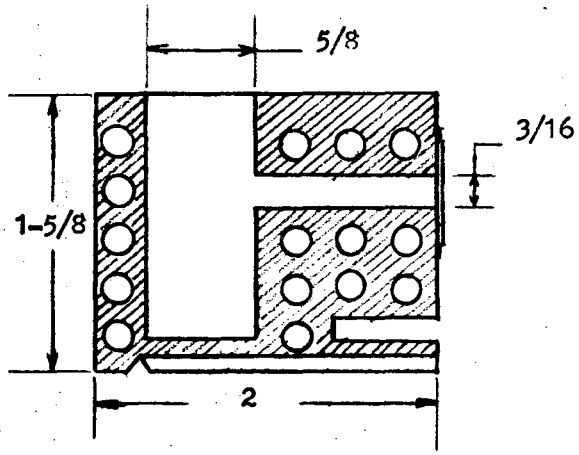


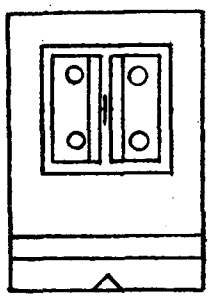

Front view
with slit.

XBL 689-5810

Fig. 5. Diagram of molecular beam source.

A current of 4.5 A at 75 V provides an oven temperature of approximately 550°C. A hole, 0.08" in diameter, was drilled in the oven to a depth of 1/16" from the vapor chamber near the front of the oven, in order to mount a thermocouple. Thermocouple wires (10 mil diameter Pt-10% Rh) are encased in a ceramic tube for insulation and, in order to insure good thermal contact with the oven walls, the hot junction is imbedded in a copper rod. Calibration of the thermocouple entailed periodic comparison with a Hewlett Packard Quartz Thermometer certified with an accuracy of ±0.02%. Measurement of the thermoelectric voltage was accomplished with a Calibration Standards model DC-200 AR precision digital voltmeter previously calibrated with a nanovolt potentiometer. Temperature measurements are believed to be accurate to better than ±1%.

The ratio of the cross-sectional area of the sample well to the area of the aperture is $3.925 \times 10^2$. Since most of the alkali halides are expected to have evaporation coefficients of the order of 1,[27] and since the slit thickness is 1 mil, it is expected that thermal equilibrium exists and the resulting beam is characteristic of an effusive source. An analysis of the beam characteristics of CsOH will be discussed in a later section.

## C. The Velocity Selector

### 1. Introduction

A number of investigators have used mechanical velocity selectors to obtain monoenergetic beams of particles.[21,22,28-33] The most commonly used types are rotating cylinders with helical grooves and the

slotted disk type. Since the rotating cylinder type requires more difficult machining problems and has a larger moment of inertia, the slotted disk type is usually preferred.[29] Both selectors can be designed so that velocity sidebands are eliminated. The resolution and transmission are varied according to the purpose of the selector.

The present velocity selector is the slotted disk type and consists of six disks. The purpose of the selector is to obtain velocity distributions of atoms and molecules, and to velocity select molecules for deflection experiments. It is characterized by a modest transmission of 30.5%, a high maximum rotational speed of 40,000 rpm, and a high resolution of 3.5%. Rotation and transmission is allowed in the forward and reverse directions. This allows the angle of orientation of the rotor axis with the beam axis to be determined, and corrections can be made if there is any misalignment.[31]

## 2. Design Principles

A theoretical analysis of the design of slotted disk velocity selectors has been reported in the literature.[34,35] Although the theoretical treatment would give a suitable selector design, the present design closely follows the design principles given by Hostettler and Bernstein.[29] A diagram of the "unrolled" disks and their relative positions is given in Fig. 6. The path through the maze of slots appears helical in the three dimensional representation, but is a straight line in the diagram. The orientation of the end disks determines the path and velocity of the molecule. Intermediate disks are positioned to block out all trajectories which would lead to sidebands.

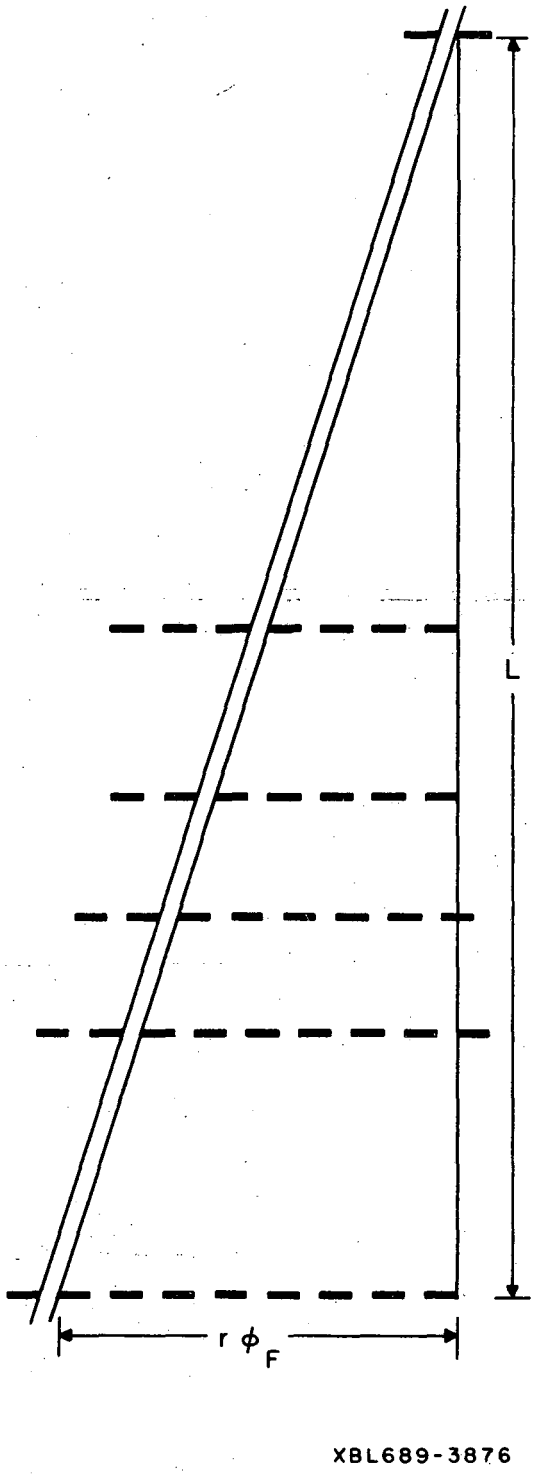


Fig. 6. "Unrolled" disk representation of rotor.

The rotor design is characterized by the three parameters

$$\beta = d/L$$

$$\gamma = l_1/r\phi_o$$

and

$$T_o = l_1/(l_1 + \bar{l}_2) \quad ,$$

where $\gamma - \beta \approx R$ is the half-width at half-maximum intensity, $T_o$ is the fraction of the incident beam that enters any one of the slots, $d$ is the thickness of the disks, $L$ is the length of the rotor, $l_1$ is the slot width, $\bar{l}_2$ is the wall thickness between the slots at the radius $r$, and $\phi_o$ is the angle through which the rotor turns in the time it takes a particle with velocity $v_o$ to traverse a distance $L$. The transmitted velocity $v_o$ is given by

$$v_o = \omega L/\phi_o$$

where $\omega$ is the angular velocity.

The velocity selector can rotate in either the forward or reverse direction, but was designed for use primarily in the forward direction. With this dual range, it is possible to determine the magnitude of the misalignment angle $\theta$ of the rotor axis with the beam axis. This is done without reference to any properties of the beam or oven, or a comparison of the theoretical and experimental temperatures at the maximum intensity. Velocity distributions are taken with the rotor moving in the forward and reverse directions and $\theta$ is determined by taking the ratio of the rotor speeds at the maximum intensity from the following equation:

$$\omega_F/\omega_R = (|\phi_F| - \theta)/(|\phi_R| + \theta)$$

Then, the correct particle velocities are

$$\nu = \omega_F \, L/(|\phi_F| - \theta)$$

$$\nu = \omega_R \, L/(|\phi_R| + \theta)$$

In order to facilitate easy alignment, the disks were oriented so that, if a slot of one of the end disks is projected along a line which is parallel to the rotor axis, an edge of this slot either coincides with other slot edges or coincides with the middle of a tooth. Figure 6 was drawn with the value of $l_2$ at the base of the slot, since this is the least favorable case for the elimination of sidebands. A value of $\phi_F$ was chosen and, using a method of trial and error, intermediate disks were positioned at 6.35, 9.14, 12.01, and 16.01 cm from the leading edge of the first disk in order to block sidebands. Many sidebands are removed from the beam due to the finite thickness of the disks. Some slow velocity molecules are blocked by the sidewalls of the first disk.

In the actual alignment process, the slots were aligned by sighting along the top edge of the slots. Slightly smaller average values of the resolution and transmission result, $\phi_F$ remains the same, and a suitable path is allowed for the reverse direction. Calculation of the rotor parameters proceeds as follows:

a) $l_1 + l_2 = 2\pi/233$

b) $l_1 = \left(\frac{l_1}{l_1 + l_2}\right) \frac{1}{233}$

c) $\phi_F = 8(l_1 + l_2) - l_1$

d) $\phi_R = 2(l_1 + l_2) + (l_1 - \Delta) + \frac{4}{5} l_1$

where $\Delta = l_2^{top}$ (rad.) $- l_2^{base}$ (rad.).

A summary of the rotor parameters is given in Table VIII.

## 3. Resolution and Transmission

Several authors have developed the theory of instrument resolution for a rotating mechanical velocity selector. The present treatment is essentially the same as that of Dash and Sommers,[32] but applied to a slotted disk selector. The treatments of Hostettler and Bernstein,[29] and Miller and Kusch[21] are directly applicable and a number of the relations derived in their work are used here.

Consider Fig. 7 on page 41. During the time it takes the rotor to turn through the angle $\phi_o$, a particle with velocity $v_o$ moves through the distance L. The selected particle velocity is then

$$v_o = \omega L/\phi_o$$

Similarly,

$$v_{min} = (L+d)\omega/(\phi_o + l_1/r) \quad ,$$

$$v_{max} = (L-d)\omega/(\phi_o - l_1/r)$$

Table VIII. Specifications of Velocity Selector.

| | | |
|---|---|---|
| Number of disks | | 6 |
| Number of slots per disk | | 233 |
| Diameter of disks | | 10.16 cm |
| Length of slots (in radial direction) | | 0.8045 cm |
| Slot width, $l_1$ | | 0.0465 cm |
| Wall thickness between slots | | |
| At base of slots | | 0.0688 cm |
| At top of slots | | 0.0905 cm |
| Average value, $l_2$ | | 0.0797 cm |
| Average radius, r | | 4.6777 cm |
| Disk thickness, d | | 0.1568 cm |
| Over-all length of rotor, L + d | | 30.6372 cm |
| | Forward | Reverse |
| $\phi$ | 0.2058 rad | 0.070 rad |
| $\gamma$ (average) | 0.0399 | 0.033 |
| $\beta$ | 0.0051 | 0.0051 |
| $T_o$ (average) | 0.3047 | 0.087 |
| Resolution, R | 0.0348 | 0.028 |

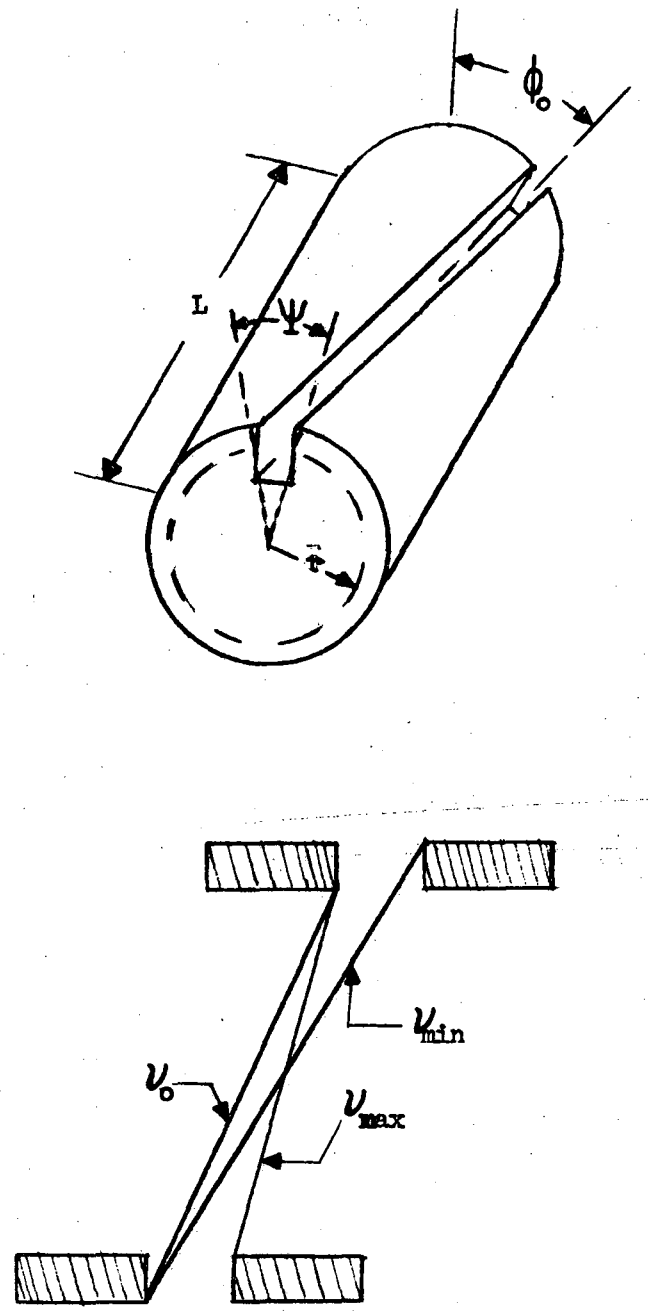


XBL 689-5811

Fig. 7. Diagrams used in deriving transmission function.

Since we set

$$\beta = d/L \quad , \quad \gamma = l_1/r\phi_o$$

then

$$\nu_{min} = \nu_o(1+\beta)/(1+\gamma) \quad ,$$

$$\nu_{max} = \nu_o(1-\beta)/(1-\gamma)$$

The resolution is given by

$$R = \Delta\nu/2\nu_o = (\gamma-\beta)/(1-\gamma^2) \simeq \gamma - \beta$$

The velocity distribution $I(\nu)$ of the particles emerging from the velocity selector is given as the product of the incident beam distribution $I_o(\nu)$ and the selector transmission function $T(\nu)$, integrated over the velocity spread of the mechanical selector, i.e.,

$$I(\nu) = \int_{\nu_{min}}^{\nu_{max}} I_o(\nu)\, T(\nu)\, d\nu \qquad (6)$$

The function $T(\nu)$ will be determined for the following two cases:

Case 1: Helical Path, Finite Rotor Slot Width, Parallel Beam

The velocity selector consists of N identical helical paths of pitch $L/\phi_o$, rotating at constant angular velocity $\omega$, and presenting an angular aperture $\psi$ to the incident beam. The beam is assumed to be directed parallel to the axis of rotation with no angular divergence. The fraction of the incident beam that enters any one of the helical paths, $T_o$, can be expressed as

$$T_o = N\psi/2\pi$$

Particles with velocity $v_o$ travel the length of the helix at a constant distance from the slot walls. Particles with velocity $v$ move a transverse distance $r_o\delta_o$ relative to the slot walls during transit. It follows that the emerging particles must have seen a reduced aperture given by

$$\text{REDUCED APERTURE} = \psi - |\delta\phi| \quad ; \; 0 \leq |\delta\phi| \leq \psi$$

The selector transmission function is then

$$T(v) = N(\psi - |\delta\phi|)/2\pi = T_o(1 - |\frac{\delta\phi}{\psi}|)/2\pi \quad ; \; |\delta\phi| \leq \psi \tag{7}$$

and

$$T(v) = 0 \quad ; \; |\delta\phi| > \psi$$

If we express

$$v_{min} = \omega(L+d)/(\phi+\delta\phi)$$

and

$$v_{max} = \omega(L-d)/(\phi-\delta\phi)$$

then, after some rearrangement, $\delta\phi$ can be expressed as

$$\delta\phi = -\phi_o\left[(v_o/v)(1-\beta) - 1\right] \quad ; \; v_o < v < v_{max} \tag{8}$$

and

$$\delta\phi = +\phi_o\left[(v_o/v)(1+\beta) - 1\right] \quad ; \; v_o > v > v_{min} \tag{9}$$

Upon substitution of Eqs. (8) and (9) into Eq. (7), we obtain

$$T(\nu) = T_o \left\{1 - [(\nu_o/\nu)(1+\beta) - 1]/\gamma\right\} \quad ; \quad \nu_o > \nu > \nu_{min}$$

$$T(\nu) = T_o \left\{1 + [(\nu_o/\nu)(1-\beta) - 1]/\gamma\right\} \quad ; \quad \nu_o < \nu < \nu_{max}$$

$$T(\nu) = 0 \quad ; \quad \nu_{min} > \nu > \nu_{max}$$

where

$$\gamma = \psi/\phi_o$$

From Eq. (6),

$$I(\nu) = \int_{\nu_{min}}^{\nu_{max}} I_o(\nu)\, T(\nu)\, d\nu$$

Calculations of other authors[21] have indicated that little error is introduced if it is assumed that the velocity distribution which enters the aperture of the rotor is invariant over the range of velocities allowed for a given rotor speed $\omega$. Hence, Eq. (6) becomes

$$I(\nu) \simeq I_o(\nu) \int_{\nu_{min}}^{\nu_{max}} T(\nu)\, d\nu \qquad (10)$$

The integration of $T(\nu)$ is piecewise from $\nu_o$ to $\nu_{max}$ and from $\nu_{min}$ to $\nu_o$. Upon integrating,

$$\int_{\nu_o}^{\nu_{max}} T(\nu)\, d\nu = T_o\, \gamma^{-1}\, \nu_o \left\{(1-\beta)\, \ln \frac{(1-\beta)}{(1-\gamma)} + (\gamma-1) \left[\frac{(1-\beta)}{(1-\gamma)} - 1\right]\right\}$$

$$\int_{\nu_{min}}^{\nu_o} T(\nu)\, d\nu = T_o\, \gamma^{-1}\, \nu_o \left\{(1+\beta)\, \ln \frac{(1+\beta)}{(1+\gamma)} + (\gamma+1) \left[1 - \frac{(1+\beta)}{(1+\gamma)}\right]\right\}$$

Finally,

$$I(\nu) = I_o\, \gamma^{-1}\, \nu_o T_o \left[(1+\beta)\, \ln \frac{(1+\beta)}{(1+\gamma)} + (1-\beta)\, \ln \frac{(1-\beta)}{(1-\gamma)}\right]$$

For $\beta$ and $\gamma \ll 1$

$$I(\nu) = I_o(\nu)\, T_o\, \nu_o\, \gamma(1-\beta/\gamma)^2 = G\, \nu_o\, I_o(\nu)$$

where

$$G = T_o\, \gamma(1-\beta/\gamma)^2$$

Hence,

$$I(\nu) = G\, \nu_o\, I_o(\nu) \tag{11}$$

From Maxwell's equation, the number of molecules, dN, within the velocity interval $\nu$ to $\nu + d\nu$ is

$$dN = (4N/\pi^{1/2})(\nu^2/\alpha^3)\, \exp(-\nu^2/\alpha^2)\, d\nu \tag{12}$$

where

$$\alpha = (2\, k\, T/m)^{1/2}$$

In a molecular beam,

$$dN/N = \text{constant}\ (4/\pi^{1/2})(\nu^3/\alpha^3)\, \exp(-\nu^2/\alpha^2)\, d\nu$$

Upon normalization of dN/N,

$$dN/N = (2\nu^3/\alpha^4)\, \exp(-\nu^2/\alpha^2)\, d\nu$$

and

$$I_o(\nu) = (2\nu^3/\alpha^4)\, \exp(-\nu^2/\alpha^2) \tag{13}$$

Equation (13) describes the velocity unselected intensity in the beam. By substituting this equation into Eq. (11), we obtain the velocity selected intensity in the beam.

$$I(\nu) = 2\, G(\nu^4/\alpha^4)\, \exp(-\nu^2/\alpha^2) \qquad (14)$$

where the most probable velocity, $\nu_{pb}$, of the velocity selected beam is

$$\nu_{pb} = (4\, k\, T/m)^{1/2}$$

Case 2: Helical Path, Finite Slot Width, Divergent Beam

Beam divergence can occur in the radial and tangential directions. If the main direction of the beam is parallel to the axis of the rotor, the effect of beam divergence is, for the most part, cancelled by positive and negative deviations. However, if there is a small misalignment of the rotor axis to the beam axis, the transmission and calculated velocity can be seriously in error. Hence, let us now consider the effect of a small misalignment angle $\theta$.

In this case, the transverse distance that the particles move relative to the slot walls is $r_o \delta\phi + L\theta$. The transmission function becomes

$$T'(\nu) = T_o \left(1 - \frac{\delta\phi}{\psi} - \frac{L\theta}{r_o \psi}\right) = T(\nu) - \int_{\nu_{min}}^{\nu_{max}} T_o(\nu)\, \frac{L\theta}{r_o \psi}\, d\nu$$

$$\simeq T(\nu) - \frac{T_o L\theta}{r_o \phi_o \gamma} \left[\frac{2\nu_o}{1-\gamma^2}\ (\gamma-\beta)\right] = T(\nu) - \frac{T_o L\theta}{r_o \phi_o} \left[2\, \nu_o\, (1-\beta/\gamma)\right]$$

The total transmission becomes

$$T'(\nu) = T(\nu)\left[1 - \frac{2L\theta}{r_o\phi_o}\,\frac{1}{\gamma-\beta}\right] \tag{15}$$

The correct velocity after including the effect of misalignment, is

$$\nu = \omega L/(\phi \pm \theta) \tag{16}$$

## 4. Construction of the Velocity Selector

The disks were first machined from 5 × 5 × 1/16-inch plates of rolled 7075-T6 aluminum alloy. Nine such plates were clamped together and a 7/8-inch hole was drilled through the center of the stack. The stack was then placed on a milling shaft and clamped into position. Two 1.8-inch dowel pin holes were drilled 1.06 inches off center at 180° apart. The dowel pins were inserted after each hole was drilled. Disks were then turned to a 4 inch diameter.

A 17 mil high speed steel saw was used to cut the slots. With the disks remaining in the above clamped position, every fourth slot position was milled on each pass around the disk. After each pass, mylar shims were epoxyed in the slots. This procedure was followed until all 233 slots were finished. When the shims were removed, it was found that the resulting slots were curved and out of tolerance. This cutting catastrophe was believed to be due to stresses set up in the material when the plates were rolled and stretched for flatness.

A more successful approach involved first cutting the plates from a five-inch diameter rod of 7075-T6 aluminum alloy. Then the

disks were heat treated to remove stresses. The remaining stresses in the disks would be uniform, since the grain direction is perpendicular to the side of the disks.

Two disks were clamped on a master plate dividing head and an electric discharge machine with a graphite electrode was used to cut the slots. Successive slots were cut and no epoxy or shims were used. A point on the dividing head was marked in order that the disks could be subsequently oriented such that particles could pass through slots cut at the same point. Since the graphite electrode was changed at regular intervals, it is expected that matching a slot cut at this point on the dividing head is equivalent to matching a slot cut through all the disks at once. This would practically eliminate errors arising from cutting some disks at different times. The slots on each finished disk were measured and were found to have a mean width of $18.3 \pm 0.5$ mils.

The disks were aligned optically according to Fig. 6, clamped into position, and 3/8-inch alignment holes were drilled over the dowel pin holes.

The rotor shaft was made of #316 stainless steel. Fafnir ball bearings (type 2 mm 9103 WO-CR, DUL) were mounted on each end of the shaft. These bearings were designed for extremely high speed applications where the centrifugal force of the balls is the principal load on the bearing. It has full shoulders on both sides of the outer race and a low land on both sides of the inner ring. This design permits assembly of bearings with a maximum complement of balls and a one piece retainer which pilots against the precision ground land of the outer ring.

The problem of vacuum lubrication of bearings is adequately discussed in the book Advanced Bearing Technology.[35] The bearings were vacuum impregnated with General Electric Versalube F-50 silicone oil. In order to keep the bearing temperature low, heat sinks were attached to the bearing housings.

On one end of the shaft, the motor and rotor ball bearings were mounted on opposite ends of a motor mount. This arrangement allows the shaft and motor to vibrate and move together, and facilitates easy alignment of the centers of the selector shaft and the motor shaft. The two shafts were connected with a 1.125-inch piece of 31 mil hardened stainless steel wire. This flexible coupling and the motor mount allowed easy assemblage and alignment of the shaft-drive system. Figure 8 is a photograph of the entire system.

The disks were placed on the shaft, held at their assigned positions by #7075-T6 aluminum spacers (which are liquid honed on each end), and aligned with the use of short rods that passed through the disks and large clamping blocks. A spanner wrench was used to lock the end nut tightly in place. The rods and clamping blocks were then removed, and the assembly was balanced and placed in the frame.

In order to contain problems of bearing friction and wear, and mechanical resonances associated with providing a suitable axis of rotation for the rotor, a number of measures were taken. 1) The frame was constructed of a heavy material (#304 stainless steel) in order to dampen, to some degree, expected vibrations, 2) the rotor was balanced to an extreme precision, and 3) the rotor is allowed to find its own

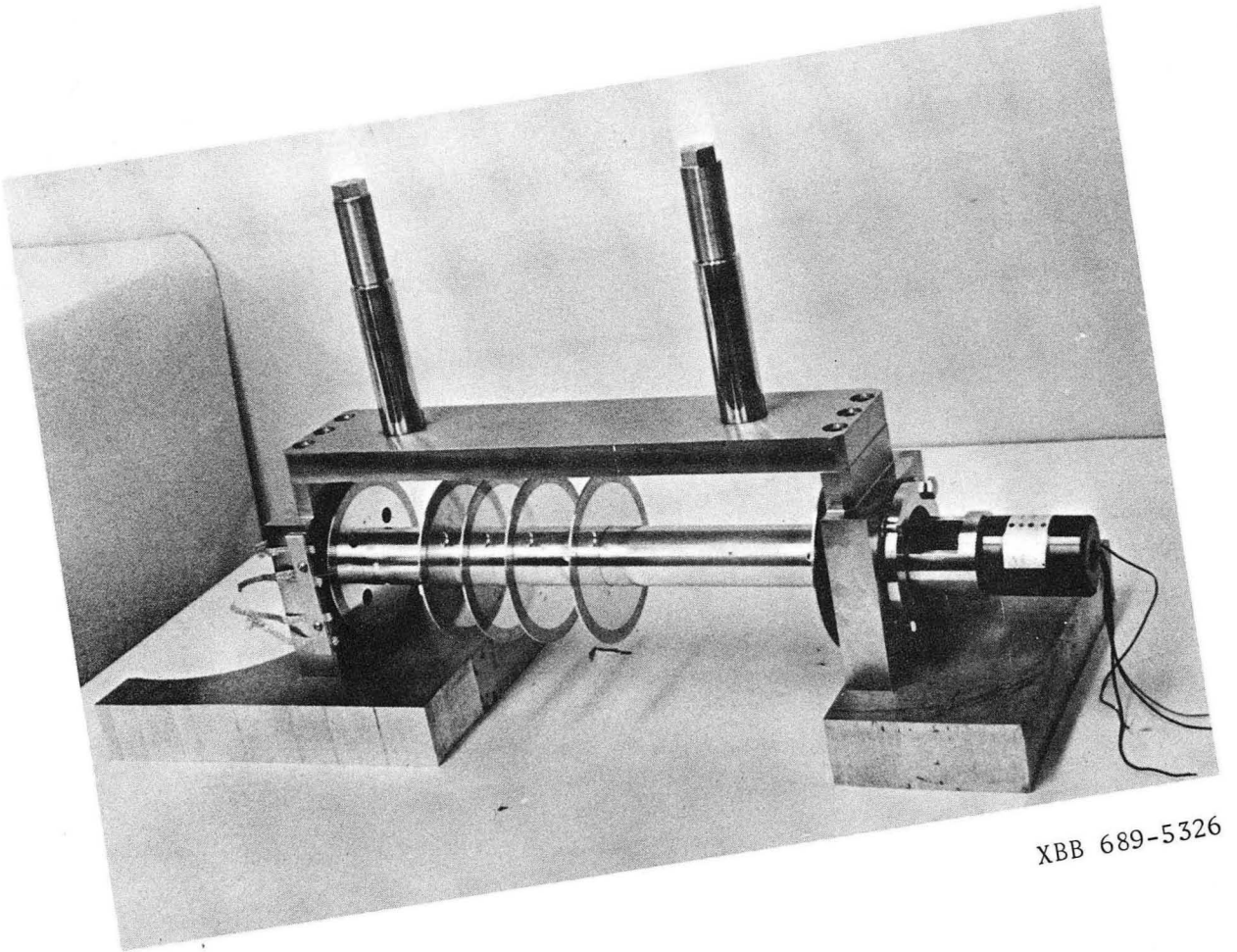


Fig. 8. Photograph of velocity selector.

axis of rotation by mounting the bearing housings inside natural rubber O-rings of 40 Durel hardness. If the rotor had been rigidly supported at both ends, a fundamental resonance would be expected at about 11,500 rpm. By using flexible mountings, the fundamental is raised to approximately 26,450 rpm.[37] The entire assembly was balanced such that there is a residual unbalance of 70 mg-mm at 10,000 rpm with no visible harmonics up to 10,000 rpm.

Approximate calculations of the stresses on the disk material (#7075-T6 aluminum alloy) indicate the existence of a maximum radial stress of $3.5 \times 10^8$ dynes/cm$^2$, and a maximum tangential stress of $1.1 \times 10^9$ dynes/cm$^2$, at 40,000 rpm. These stresses are well below the rated strength of the disk material.

The motor is a Globe Industries Inc. (#75A586) 2 pole, 2 phase, hysteresis synchronous type. A General Radio polyphase oscillator (#1305-A) delivers two-phase variable frequency power to drive a pair Altec power amplifiers (#1570 B, 175 watts each), which are connected to the motor. The speed of rotation of the rotor is determined with the use of a photocell. A small light bulb and a photocell were attached to the frame in a manner such that two pulses per revolution are transmitted to a counter. With this arrangement the instantaneous speed and acceleration of the rotor could be monitored.

Two bars attached to the top of the frame, as shown in Fig. 8, allowed easy positioning of the entire assembly. These bars passed through Wilson seals and can be raised and lowered with a chain-sprocket drive mechanism.

5. Mechanical Performance of the Velocity Selector

Except for a few minor problems, the general performance of the velocity selector was according to the design specifications. The original coupling mechanism of the rotor shaft to the motor shaft consisted of a 1.125-inch piece of music wire with set screws welded on each end of the wire at the tip of the screw. These set screws were then placed into the end of the motor and rotor shafts and turned until the wire was pulled tight. Whenever the motor was accelerated, the rotor shaft would move slightly toward the motor with the result that the assembly would not turn freely. This effect caused unnecessary friction on both the motor and rotor bearings, and eventually led to worn bearings, burned out motors, and broken wires. The situation was remedied by placing locking nuts on the set screws, and by using a piece of hardened stainless steel wire which was hard soldered to the set screws. After performing all of the experiments in this thesis, the original bearings, motor, and wire were still in operational condition.

It was found that whenever the rotor was operated at high speeds for a period of about one hour, the temperature of the motor would increase and cause excessive pressure increases in the main chamber of the apparatus. Excessive pressures in the vacuum system could not be tolerated since this would lead to scattering of the beam. For this reason, the motor was encased in a copper jacket with copper wires leading to the copper baffle of a small liquid nitrogen trap. With this arrangement, the motor temperature did not increase more than

about 3°C, and the pressure within the vacuum system remained constant at about $2 \times 10^{-7}$ mm.

As mentioned earlier, a fundamental resonance was expected at about 26,450 rpm. At the highest rotor speed used, 18,000 rpm, no vibration was evident. In contrast to the tendency of rotors to bounce at certain speeds when the bearings are supported by compliant coil springs,[30] the present method of using rubber O-rings for flexible supports, allowed no bouncing at any speed.

The bearing lubricant (G.E. Versalube F-50) appears to be an excellent vacuum lubricant. Rotor bearings were lubricated only a few times during the entire period of operation.

The entire assembly performs so well that, at any frequency, the rotor speed remains constant to better than 0.1 Hz/min.

## D. Experimental Techniques

### 1. The Apparatus

The apparatus used in these experiments is essentially the same as the one in Sect. I of this thesis, with a number of modifications. Figure 9 is a schematic diagram of the present arrangement. The A and C fields, and the collimator were removed in order to mount the velocity selector. In the present arrangement, the beam stop serves as the collimator.

The oven used in the electric-resonance experiments on LiCl was quite suitable for that purpose. However, as explained earlier, it was necessary to construct an oven which conformed to the criteria for the ideal oven of kinetic theory in this case.

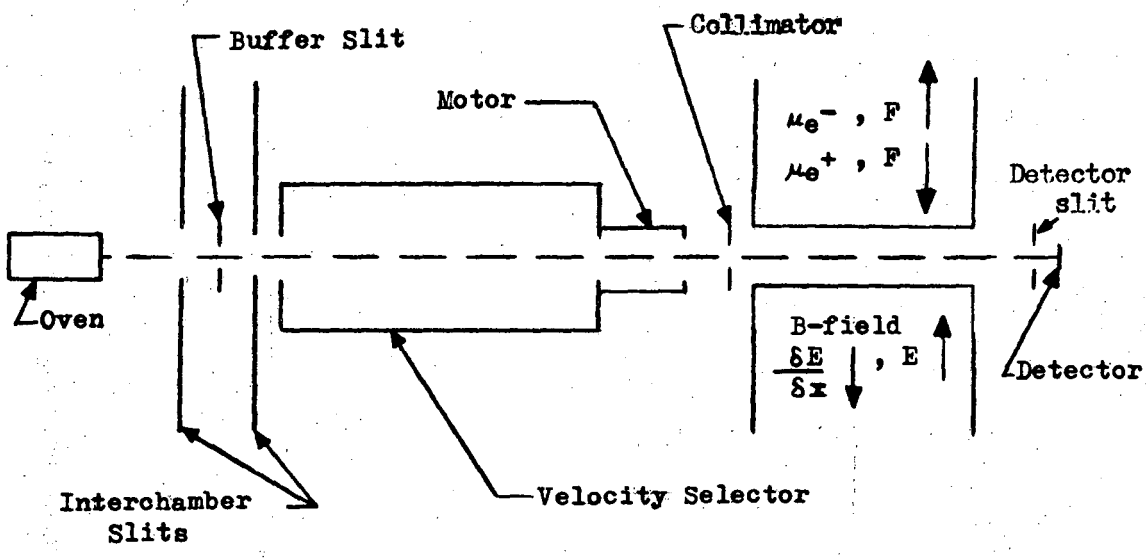


XBL 689-5812

Fig. 9. Schematic diagram of apparatus.

The oven rests atop three tapered pins which are mounted in a molybdenum plate. A lava block is sandwiched between the molybdenum plate and a stainless steel tray in order to reduce heat conduction. The stainless steel rod leading from the tray is locked into a copper bar which passes through a nylon bushing to a power source outside of the vacuum system.

A telemicroscope was used to align the hot-wire detector, the detector slit, the B-field, the main chamber collimator, and the buffer slit. During the assembly of the rotor, a hairline mark was accurately made on each of the disks indicating a straight path along the length of the rotor. Metal shims were placed in the marked slots of the first and last disks to allow sighting along this straight path with the telemicroscope. In this way, the detector, the detector slit, the B-field, the main chamber collimator, the buffer slit, and the velocity selector were placed on a common axis. The oven is placed on this axis by moving the copper bus bar horizontally across this axis and determining the center position. It is estimated that the alignment is accurate to $\pm 0.01$ cm. A misalignment error of this magnitude is expected to cause a $\pm 1\%$ error in the measured velocity. However, since the misalignment error was determined by rotating the velocity selector in the clockwise and then in the counter-clockwise directions, a correction could be made to obtain the true velocity.

Slits are held in place by 0.01588 cm thick strips, whose knife edges extend to within 0.08 cm of the slit edges. The beam is

defined by 0.0127 cm wide × 0.39688 cm high × 0.00254 cm thick oven, buffer, and detector slits, and a 0.0127 cm wide collimator. Molecules are detected on a 0.01651 cm wide × 0.00254 cm thick tungsten surface ionization detector. Although finite source and detector widths produce some beam components which are not parallel to the rotor axis, calculations and the present results indicate that the dimensions used here are sufficiently small as to cause no observable effects on the velocity distributions.

The intensity of the molecular beam was monitored on a chart recorder. Velocity distributions were taken by starting on the low velocity side of the spectrum and increasing the rotor speed until the high velocity side is reached, then decreasing the rotor speed until the low velocity side is reached again. During this procedure, which usually took 10-15 minutes, there was usually no significant change in beam intensity. The resulting data represent average values of the "uphill and downhill" runs. For calibration of the velocity selector, the above procedure was used first for the clockwise direction and then for the counterclockwise direction. The oven temperature remained constant to approximately 0.1% during individual runs.

## 2. The Experiment

Analysis of the Data. As shown earlier in Sect. II-C, the equation which characterizes the velocity distribution in a velocity selected molecular beam is

$$I(v) = I_o(v^4/\alpha^4)\exp(-v^2/\alpha^2) \qquad (17)$$

where $\alpha = (2kT/M)^{1/2}$ and is the most probable velocity within the oven at temperature T. $I_o$ is a constant determined by the geometry of the apparatus, and $I(v)$ is the measured particle intensity at velocity $v$, which is transmitted by the rotor at an angular velocity $\omega$. In order to verify that the velocity selector gives results which are characteristic of the Maxwellian $v^2$ distribution in the oven, it must be demonstrated that the experimental velocity at the maximum intensity of the measured distribution is in close agreement with the most probable velocity calculated from the temperature of the oven. Since a single component beam is needed for this purpose,[22] CsCl was used for the calibration. Equation (17) was used to give a least squares fit of the experimental distribution with $I_o$ and $\alpha$ as parameters. The experimental most probable velocity in the velocity selected beam, $\sqrt{2}\,\alpha$, could then be compared to the theoretical most probable velocity.

A number of investigators have shown that by accurately measuring the velocity distribution of a molecular beam which contains several species, the relative abundance of the individual components can be determined.[22,28,33] This velocity distribution represents a superposition of the Maxwellian distributions of each of the individual components. In cases where there is no information available, a multicomponent system is assumed which gives the best agreement with the experimental results. The CsCl data demonstrates that the experimental arrangement yields results predicted by kinetic theory for a single component beam. Although it is possible to determine thermochemical

data for the various equilibria which exist in the vapor phase,[22,33] it is not of interest here to do so.

Assuming that the molecular beam contains polymers, $(MX)_n$, and that the polymers completely dissociate on the surface ionization detector, n cations will be counted for each $(MX)_n$ molecule.[38] If we call $a_n$ the ratio of the number of $(MX)_n$ molecules to the number of $(MX)_1$ molecules which emerge from the oven slit per unit time, then the ratio of the concentration of $(MX)_n$ to $(MX)_1$ within the source is

$$C_n/C_1 = a_n \sqrt{n} \quad ,$$

and the percentage $(MX)_n$ present in the source is

$$\%(MX)_n = \frac{a_n \sqrt{n}}{a_n \sqrt{n} + 1} \quad (100)$$

The factor $\sqrt{n}$ derives from the greater diffusion rate of light molecules from the oven. Hence, when polymers are present, the expression for the velocity distribution becomes

$$I(v) = I_o \, (v^4/\alpha^4) \exp(-v^2/\alpha^2) \left\{1 + \sum_n a_n \, n^3 \exp\left[-(n-1) \frac{v^2}{\alpha^2}\right]\right\} \quad (18)$$

In this case, $I_o$ and $a_n$ are the parameters in the least squares fit. A Control Data Corporation 6600 computer was used to fit all experimental results.

CsCl Data. Several CsCl velocity distributions were taken with the velocity selector moving in the forward and reverse directions. By taking the ratio of the rotational speeds of the rotor at the maximum intensity of the two runs, the angle of misalignment of the rotor axis with the beam axis was determined, and the most probable velocity in the beam was calculated. It was not necessary to assume the presence of any polymers in order to fit the distributions. The oven slit used in these experiments was 0.0127 cm wide. With a slit of this width, there is good agreement between the experimental and theoretical most probable velocities. The results of these experiments are given in Tables IX through XVI for various rotor-beam alignment angles. Runs #1 and 2 were obtained at the same geometry, run #3 was at a slightly different geometry, and runs #4A and 4B were done at another geometry.

Other investigators[39] have indicated from mass spectrometric studies that CsCl may contain approximately 1.3% dimer.* Since the present method cannot detect polymeric species which are present in a concentration of less than 2%, and since the earlier work by Miller and Kusch supports the results contained here, it appears that the experiments performed with the present beam source and velocity selector give conclusive results within the limitations of the technique.

---

*This number was estimated from dimer to monomer ion ratios using a value of 1.75 for the relative ionization cross sections of dimer to monomer.

The CsCl sample used was obtained from Fisher Chemical Company and was 99.9% pure. Figure 10 gives a comparison of the theoretical and experimental velocity distributions of one of the runs.

RbCl Data. Velocity distributions for RbCl were taken under the same conditions as for CsCl. The sample, obtained from City Chemical Company, was 99.9% pure. In order to fit the RbCl distributions, it was necessary to assume the presence of about 5% dimer. As seen from Table IX, the ratio of dimer to monomer, $a_2$, is in agreement with the results of Miller and Kusch within experimental error. Figures 11 and 12 give the results of the data analysis in graphical form.

Effect of Wide Slit. For the deflection experiments, a 0.01778 cm wide slit was used in order to make the oven position insensitive when obtaining the maximum beam signal. The resulting experimental velocity distributions then appeared to be narrower, indicating that the beam source was no longer effusive. This result is expected since the ratio of the cross-sectional area of the sample chamber to the slit area, in this case, approaches the limits of the conditions for an effusive source.[24] However, the results of the deflection experiments, which were taken at points on the velocity distribution curves where polymer concentrations were small, indicated that the effect of the slight narrowing of the velocity distributions was negligible in comparison to other sources of error.

In order to calculate the molecular beam velocity from the angular velocity of the rotor, it is necessary to multiply the pulses

received at the counter by the factor 488.99. This final number reflects a slight change in the misalignment angle when the entire system was aligned for the final deflection experiments.

Table IX. Summary of CsCl and RbCl results. The theoretical value of the velocity at the maximum intensity was calculated for a beam which consists only of monomers. The oven slit width is 0.0127 cm for all runs except 4A and 4B, where it is 0.01778 cm.

| CsCl | T°K | Theoretical ν (±0.02 cm/sec) | Experimental ν (±0.02 cm/sec) |
|---|---|---|---|
| 3 | 837 | $4.07 \times 10^4$ | $4.07 \times 10^4$ |
| 2 | 851 | $4.10 \times 10^4$ | $4.11 \times 10^4$ |
| 1 | 858 | $4.12 \times 10^4$ | $4.13 \times 10^4$ |
| 4A | 845 | $4.09 \times 10^4$ | $4.04 \times 10^4$ |
| 4B | 845 | $4.09 \times 10^4$ | $4.04 \times 10^4$ |

| RbCl | T°K | $a_2$ (±0.02) | |
|---|---|---|---|
| 2 | 848 | 0.052 | Present results |
| 1 | 869 | 0.051 | |

| RbCl | T°K | $a_2$ (±0.015) | |
|---|---|---|---|
| 167 | 868 | 0.056 | Two runs at comparable temperatures from Miller and Kusch[22] |
| 168 | 879 | 0.058 | |

Table X. CsCl velocity distribution data.

#1 CsCl

T = 858°K

Oven slit = 0.0127 cm

| Forward run | | Reverse run | |
|---|---|---|---|
| Velocity (Hz) | Intensity | Velocity (Hz) | Intensity |
| 31.7 | 2.25 | 14.4 | 14.8 |
| 42.1 | 7.95 | 18.3 | 30.6 |
| 52.7 | 17.70 | 21.3 | 46.2 |
| 62.9 | 27.80 | 25.5 | 68.5 |
| 73.1 | 35.50 | 29.6 | 83.0 |
| 77.2 | 37.30 | 30.6 | 84.9 |
| 81.3 | 38.25 | 31.7 | 86.3 |
| 85.4 | 38.50 | 32.8 | 87.8 |
| 89.5 | 38.15 | 33.8 | 87.0 |
| 93.5 | 37.15 | 34.9 | 86.5 |
| 103.8 | 32.35 | 39.0 | 77.5 |
| 114.0 | 25.75 | 42.1 | 67.6 |
| 124.0 | 19.00 | 46.4 | 31.0 |
| 133.5 | 13.10 | 50.6 | 35.2 |
| 143.9 | 8.30 | 54.8 | 22.2 |
| 153.5 | 4.85 | 59.0 | 13.3 |
| 163.7 | 2.75 | 62.9 | 8.0 |
| 173.2 | 1.80 | 67.0 | 5.0 |

$\omega_F$ = 86.098 Hz at $I_{max}$ $\omega_R$ = 32.871 Hz at $I_{max}$

$\theta$ = +0.00613 rad

Table XI. CsCl velocity distribution data.

#2 CsCl

T = 851°K

Oven slit = 0.0127 cm

| Forward run | | Reverse run | |
|---|---|---|---|
| Velocity (Hz) | Intensity | Velocity (Hz) | Intensity |
| 31.7 | 4.0 | 14.4 | 7.4 |
| 42.1 | 13.9 | 18.3 | 14.7 |
| 52.7 | 29.5 | 21.2 | 21.8 |
| 62.9 | 45.0 | 25.5 | 31.0 |
| 73.1 | 56.0 | 29.6 | 36.8 |
| 83.4 | 60.5 | 30.6 | 37.7 |
| 87.3 | 60.3 | 32.7 | 38.0 |
| 93.4 | 57.9 | 34.8 | 37.2 |
| 103.9 | 50.0 | 36.9 | 36.4 |
| 113.8 | 39.8 | 40.0 | 31.8 |
| 124.0 | 28.9 | 44.2 | 25.1 |
| 133.8 | 19.4 | 48.5 | 18.0 |
| 144.0 | 12.1 | 52.7 | 12.1 |
| 153.5 | 7.0 | 56.9 | 7.7 |
| 163.4 | 3.6 | 61.1 | 4.7 |
| | | 65.0 | 3.4 |

$\omega_F$ = 85.280 Hz at $I_{max}$ $\omega_R$ = 33.093 Hz at $I_{max}$

$\theta$ = +0.00703 rad

Table XII. CsCl velocity distribution data.

#3 CsCl

T = 837°K

Oven slit = 0.0127 cm

| Forward run | | Reverse run | |
|---|---|---|---|
| Velocity (Hz) | Intensity | Velocity (Hz) | Intensity |
| 31.70 | 7.83 | 10.40 | 0.271 |
| 42.20 | 32.88 | 14.40 | 0.849 |
| 52.70 | 67.63 | 18.30 | 1.845 |
| 63.00 | 92.51 | 21.30 | 2.776 |
| 73.20 | 117.45 | 25.50 | 3.960 |
| 79.45 | 122.50 | 29.60 | 4.655 |
| 83.45 | 123.94 | 31.60 | 4.711 |
| 87.40 | 122.86 | 33.80 | 4.763 |
| 93.60 | 118.36 | 37.90 | 4.270 |
| 103.85 | 103.26 | 42.10 | 3.455 |
| 113.90 | 82.79 | 46.30 | 2.556 |
| 124.15 | 60.49 | 50.55 | 1.701 |
| 133.95 | 40.91 | 54.80 | 1.008 |
| 143.90 | 22.17 | 59.00 | 0.679 |
| 153.70 | 11.22 | | |
| 163.50 | 5.68 | | |

$\omega_F$ = 84.806 HZ at $I_{max}$ $\omega_R$ = 32.598 Hz at $I_{max}$

$\theta$ = +0.00651 rad

Table XIII. CsCl velocity distribution data.

#4A CsCl

T = 845°K

Oven slit = 0.01778 cm

| Forward run | | Reverse run | |
|---|---|---|---|
| Velocity (Hz) | Intensity | Velocity (Hz) | Intensity |
| 31.20 | 7.65 | 12.30 | 7.00 |
| 36.40 | 13.80 | 14.25 | 12.00 |
| 41.65 | 22.00 | 16.30 | 19.00 |
| 46.85 | 31.90 | 18.15 | 27.35 |
| 52.10 | 42.80 | 20.20 | 36.75 |
| 57.25 | 53.15 | 21.00 | 40.70 |
| 62.25 | 62.55 | 23.00 | 50.85 |
| 67.25 | 70.65 | 25.10 | 59.25 |
| 72.35 | 76.55 | 27.10 | 68.40 |
| 77.45 | 79.85 | 29.20 | 74.00 |
| 82.50 | 81.10 | 31.25 | 77.75 |
| 87.45 | 80.00 | 33.35 | 78.65 |
| 92.55 | 76.50 | 35.45 | 77.65 |
| 97.90 | 71.15 | 37.45 | 74.10 |
| 102.90 | 64.45 | 39.55 | 70.10 |
| 108.15 | 56.55 | 41.60 | 63.50 |
| 112.85 | 49.55 | 43.70 | 56.55 |
| 116.90 | 43.40 | 45.75 | 49.65 |
| 123.00 | 34.95 | 47.90 | 42.30 |
| 128.15 | 28.00 | 50.05 | 35.05 |
| 132.70 | 23.00 | 52.05 | 28.90 |
| 137.00 | 18.70 | 54.05 | 23.50 |
| 142.80 | 13.85 | 56.20 | 18.70 |
| 148.15 | 10.30 | 58.35 | 14.65 |
| 152.60 | 8.10 | 60.40 | 11.30 |
| $\omega_F$ = 82.597 Hz at $I_{max}$ | | $\omega_R$ = 33.724 Hz at $I_{max}$ | |

$\theta$ = +0.00992 rad

Table XIV. CsCl velocity distribution data.

#4B CsCl

T = 845°K

Oven slit = 0.01778 cm

| Forward run | | Reverse run | |
|---|---|---|---|
| Velocity (Hz) | Intensity | Velocity (Hz) | Intensity |
| 31.25 | 3.34 | 12.30 | 0.96 |
| 36.35 | 6.14 | 14.30 | 1.76 |
| 42.05 | 9.83 | 16.25 | 2.81 |
| 46.65 | 14.22 | 18.20 | 4.06 |
| 52.10 | 19.14 | 20.35 | 5.70 |
| 57.20 | 23.92 | 23.00 | 7.50 |
| 62.10 | 28.22 | 25.10 | 8.85 |
| 67.40 | 31.93 | 27.10 | 10.14 |
| 72.30 | 34.44 | 29.20 | 10.92 |
| 77.60 | 36.05 | 31.25 | 11.53 |
| 82.55 | 36.54 | 33.35 | 11.71 |
| 87.40 | 35.74 | 35.45 | 11.55 |
| 92.65 | 34.51 | 37.45 | 11.13 |
| 97.65 | 32.11 | 39.50 | 10.42 |
| 102.85 | 28.97 | 41.60 | 9.57 |
| 108.05 | 25.35 | 43.70 | 8.51 |
| 112.75 | 22.42 | 45.75 | 7.42 |
| 116.70 | 19.66 | 47.80 | 6.33 |
| 122.90 | 15.76 | 49.95 | 5.28 |
| 128.05 | 12.69 | 52.05 | 4.33 |
| 132.70 | 10.30 | 54.10 | 3.48 |
| 136.80 | 8.44 | 56.20 | 2.74 |
| 142.75 | 6.18 | 58.30 | 2.14 |
| 148.35 | 4.51 | 60.40 | 1.69 |
| 152.50 | 3.48 | | |
| $\omega_F$ = 82.548 Hz at $I_{max}$ | | $\omega_R$ = 33.778 Hz at $I_{max}$ | |

$\theta$ = +0.01001 rad

Table XV. RbCl velocity distribution data.

#1 RbCl

T = 869°K

Oven slit = 0.0127 cm

| #1A | | #1B | |
|---|---|---|---|
| Velocity (Hz) | Intensity | Velocity (Hz) | Intensity |
| 31.60 | 3.80 | 31.60 | 4.05 |
| 42.10 | 11.85 | 42.00 | 11.85 |
| 52.60 | 24.85 | 52.55 | 23.05 |
| 62.75 | 40.05 | 62.70 | 36.80 |
| 72.95 | 55.20 | 72.95 | 50.40 |
| 83.20 | 67.35 | 83.20 | 60.65 |
| 88.25 | 71.55 | 88.20 | 64.35 |
| 93.30 | 73.80 | 93.30 | 66.60 |
| 98.55 | 74.75 | 98.45 | 67.50 |
| 103.75 | 73.85 | 105.65 | 66.45 |
| 113.65 | 69.25 | 113.60 | 62.50 |
| 123.95 | 59.50 | 123.85 | 53.75 |
| 133.60 | 48.80 | 133.60 | 44.40 |
| 143.80 | 37.00 | 143.80 | 33.75 |
| 153.45 | 26.95 | 153.35 | 24.60 |
| 163.65 | 18.60 | 163.30 | 16.90 |
| 173.35 | 12.20 | 172.55 | 11.90 |
| 182.90 | 7.55 | 182.55 | 7.20 |
| 192.90 | 4.20 | 192.90 | 4.20 |

$\nu$(cm/sec) = 480.23 × Velocity (Hz)

Table XVI. RbCl velocity distribution data.

#2 RbCl

T = 848°K

Oven slit = 0.0127 cm

| Velocity (Hz) | Intensity | Velocity (Hz) | Intensity |
|---|---|---|---|
| 31.25 | 0.71 | 112.95 | 10.62 |
| 36.40 | 1.28 | 116.95 | 10.01 |
| 41.60 | 2.09 | 123.00 | 9.02 |
| 46.80 | 3.04 | 128.15 | 8.10 |
| 52.10 | 4.28 | 132.70 | 7.25 |
| 57.20 | 5.56 | 136.90 | 6.38 |
| 62.25 | 6.76 | 143.00 | 5.40 |
| 67.25 | 7.97 | 148.15 | 4.52 |
| 72.35 | 9.19 | 152.60 | 3.86 |
| 77.45 | 10.14 | 156.50 | 3.38 |
| 82.50 | 10.93 | 162.70 | 2.59 |
| 87.55 | 11.42 | 167.90 | 2.04 |
| 92.70 | 11.77 | 172.20 | 1.64 |
| 97.70 | 11.77 | 176.30 | 1.35 |
| 102.85 | 11.56 | 182.10 | 1.00 |
| 107.95 | 11.17 | | |

$\nu$(cm/sec) = 488.99 × Velocity (Hz)

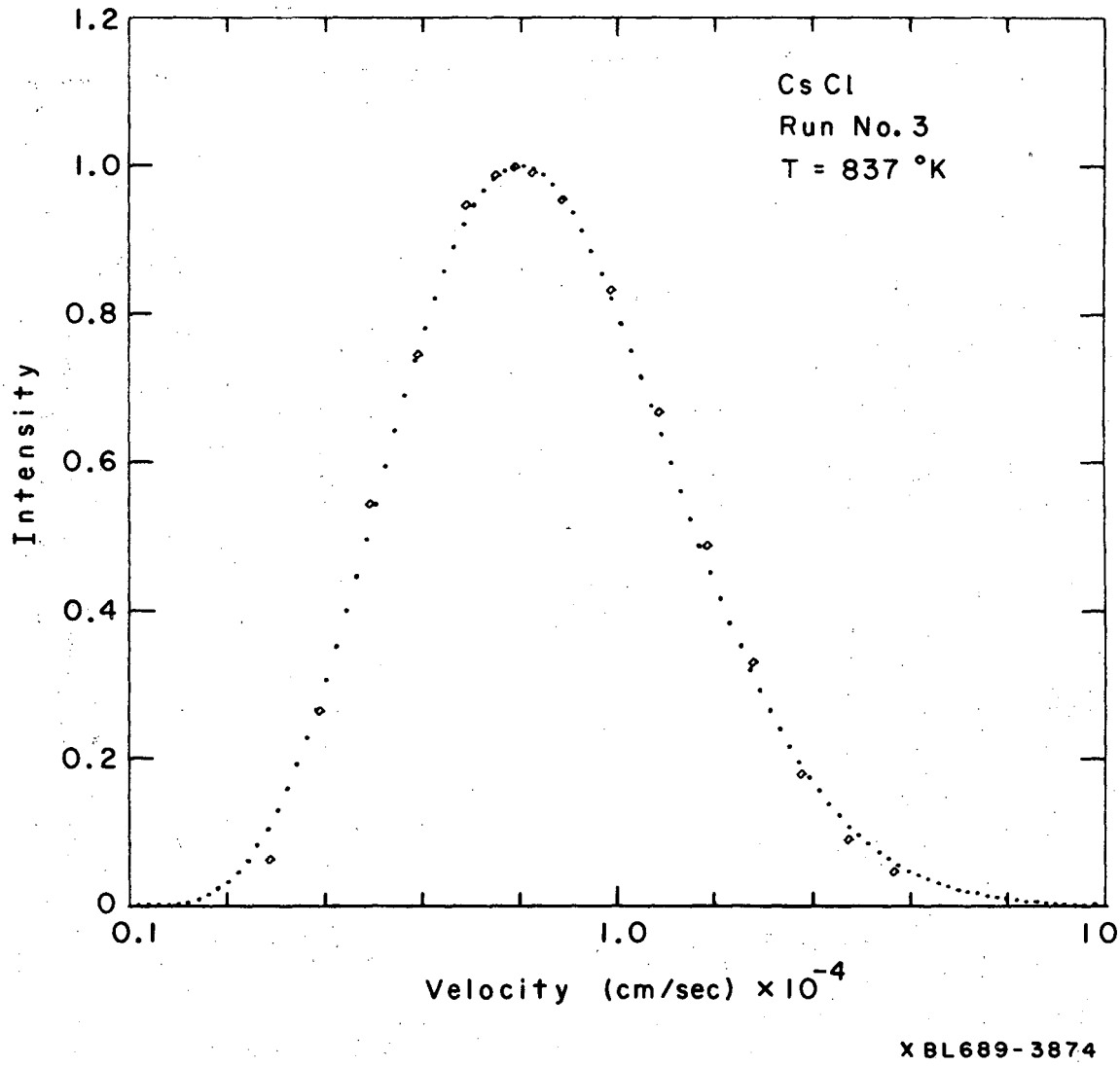


Fig. 10. Comparison of theoretical and experimental velocity distributions of CsCl.

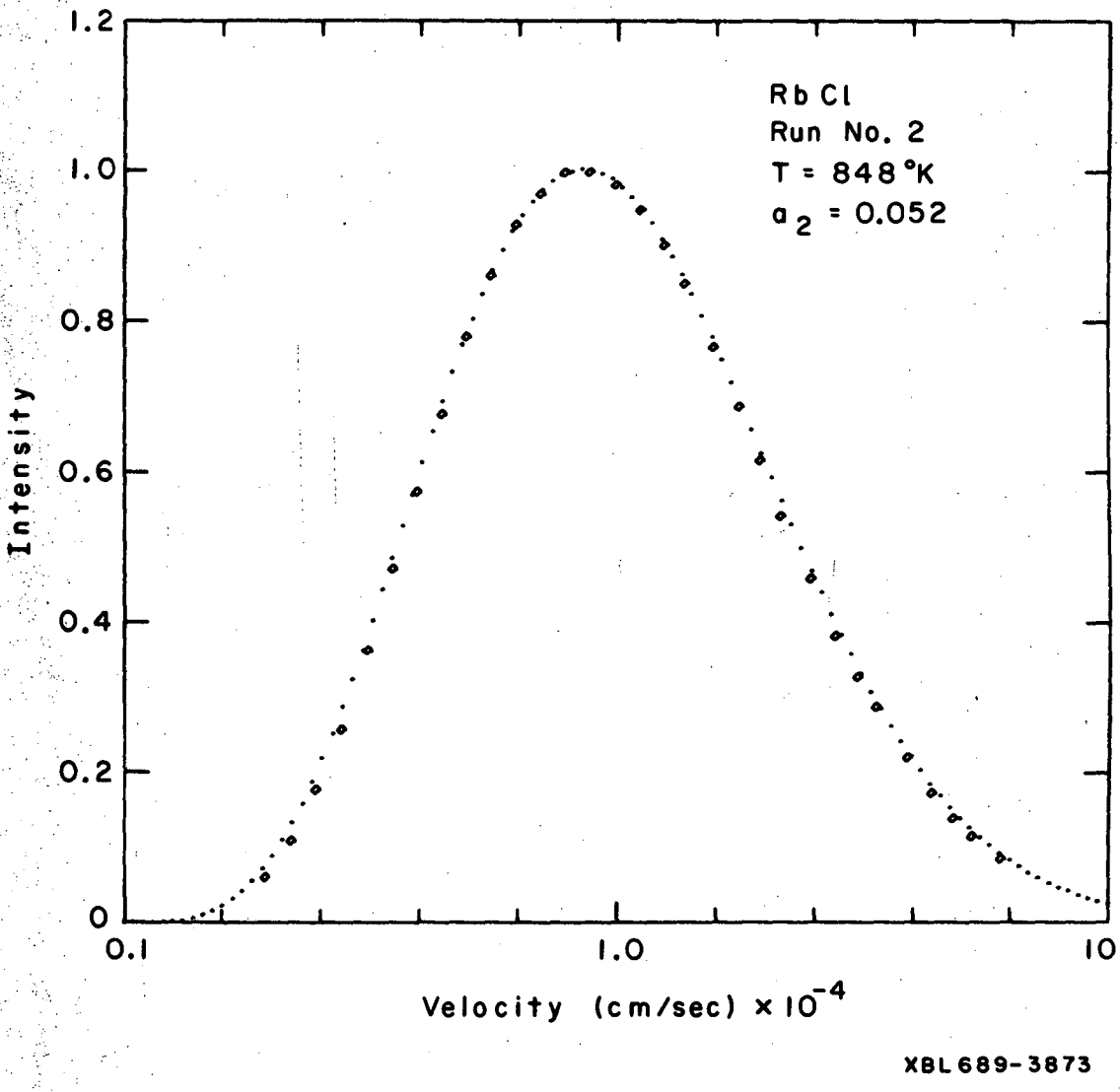


Fig. 11. Comparison of theoretical and experimental velocity distributions of RbCl.

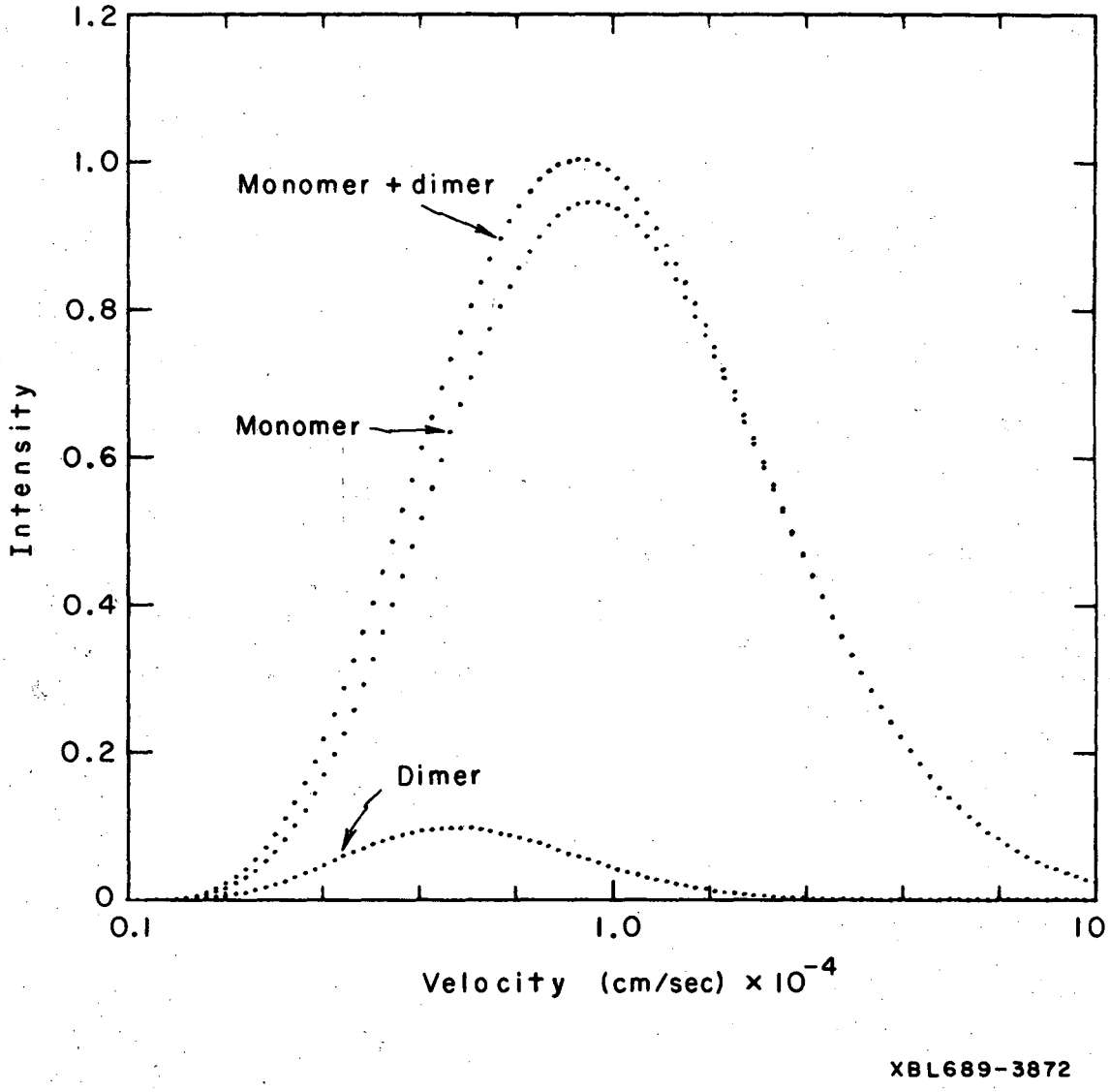


Fig. 12. Components of RbCl velocity distribution for run #2.

# IV. DIPOLE MOMENTS BY ELECTRIC DEFLECTION OF MOLECULAR BEAMS

## A. Introduction

Previous molecular beam experiments have indicated that a determination of dipole moments of molecules by deflecting velocity selected molecular beams is a viable method.[3,4] The method involves first measuring the particle intensity of a velocity selected molecular beam; then, the beam is deflected with an electric field and the resulting particle intensity is measured. The dipole moment is determined by relating the fractional number of molecules which still hit the detector to the distance which the molecules move off the detector. This is done by examining the manner in which the intensity distribution in the deflected beam depends on the dipole moment, the translational energy, the rotational energy, and the inclination of the molecular axis of rotation to the field direction.

In some cases it is possible to gain some information about molecular geometry by observing whether a beam of molecules deflects or not.[5] The absence of deflection indicates that the molecule is non-polar and that a center of symmetry is present. The presence of deflection that is not attributed to polarizability effects indicates that the molecule is polar, and that the molecule is not centrosymmetric.

In this section, theoretical expressions are derived for the intensity distribution in a deflected beam of diatomic and linear triatomic molecules. Dipole moments of KI, RbBr, RbI, CsBr, and CsI are determined. Experimental deflection results are presented for CsOH and $LaF_3$.

## B. Deflection of Linear Molecules

### 1. The Stark Effect

In the absence of an electric field, a linear polar molecule is said to possess a permanent electric dipole moment $\mu$ only in relation to a coordinate system that rotates with the molecule. When no field is present, the average value of the dipole in the laboratory coordinate system vanishes. This result is a consequence of the fact that the dipole moment is along an axis which is perpendicular to the rotational angular momentum $J$ about which the molecule rotates, and hence $\mu$ averages to zero by symmetry. In an electric field, the rotational motion is perturbed such that an admixture of rotational states are present, and there results an effective moment $\bar{\mu}$.

For both the electric resonance and the deflection experiments, it was necessary to work at high source temperatures, in order to obtain an intense enough beam to perform the experiments. At these temperatures, the characteristic rotational temperature is much less than $T$, and it is valid to assume that the distribution of rotational states can be described classically. In the electric resonance experiments, a definite rotational state was selected and refocused in the inhomogeneous field regions. In the deflection experiments, a classical distribution of rotational states is still present since no state selection is made. For the latter case, it is desirable to obtain an expression for the effective dipole moment in the language of classical mechanics.[40] Two cases must be considered, 1) when the axis of rotation is perpendicular to the direction of the electric field,

and 2) when the axis of rotation is parallel to the direction of the electric field.

1) Axis of Rotation is Perpendicular to the Field

Consider Fig. 13 on page 76. At $\psi = 0$, the angular velocity is $\omega_o$, its value in field free space. In the first quadrant, the interaction of the dipole with the field accelerates the rotation of the molecule and $\omega$ is a maximum at $\psi = \pi/2$. In the second quadrant, the rotation is retarded until $\psi = \pi = \omega_o$. In the third quadrant, the rotation is further retarded until $\omega$ is a minimum at $\psi = (3/2)\pi$. In the fourth quadrant, the rotation is once again accelerated and at $\psi = 2\pi$, $\psi$ obtains its initial value of $\omega_o$. Therefore, on the average, the dipole is oriented oppositely to the direction of the field. It follows that

$$\bar{\mu}_1 = \frac{\int_o^T \mu \sin \psi \, dt}{\int_o^T dt} \tag{19}$$

where $T$ is the period of rotation.

The equation of motion for such a system with moment of inertia $I$ is

$$I\ddot{\psi} = |\mu||E| \cos \psi$$

which upon integrating gives

$$\psi = \omega_o \left[1 + (2\mu E/I \omega_o^2) \sin \psi\right]^{1/2}$$

Hence, from Eq. (19)

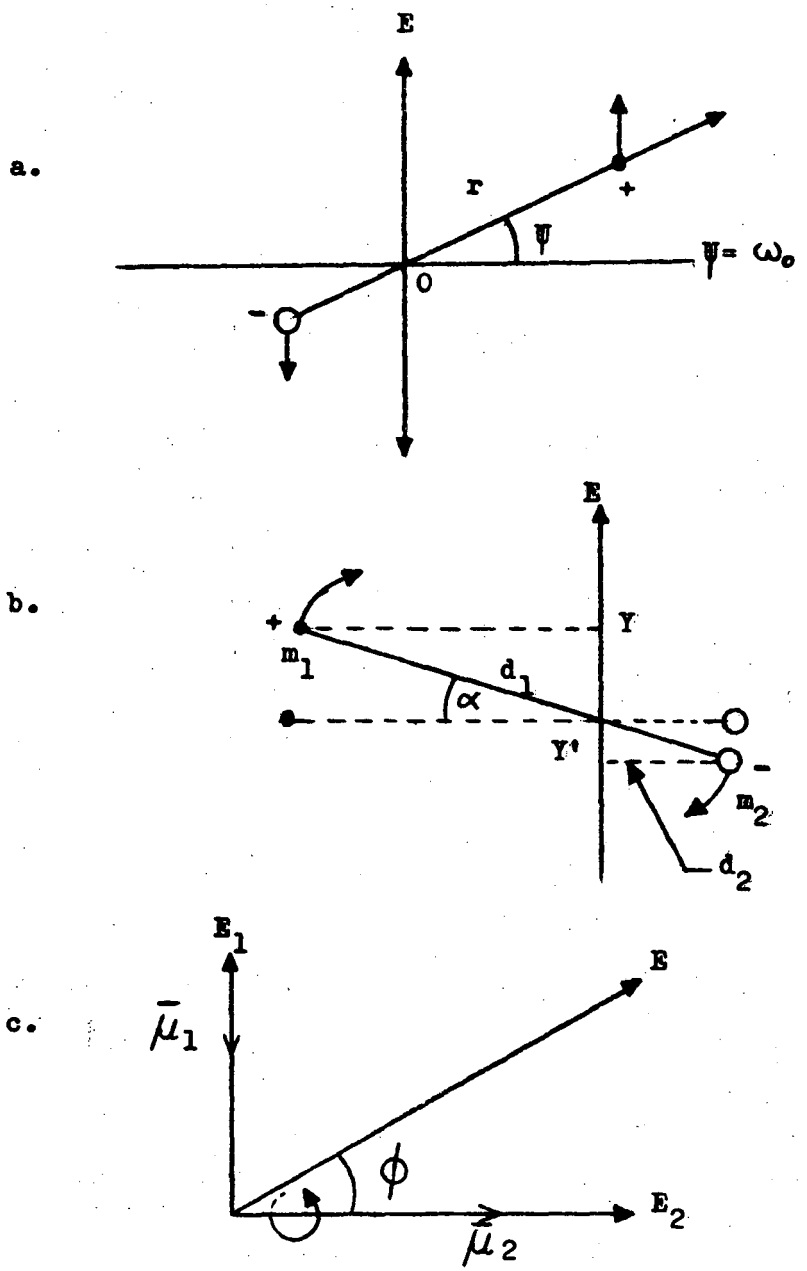


XBL 689-5813

Fig. 13. (a) Axis of molecular rotation perpendicular to field. (b) Axis of molecular rotation parallel to field. (c) Diagram used for obtaining general expression for $\bar{\mu}$.

$$\bar{\mu}_1 = \frac{\mu \int_0^{2\pi} \sin\psi \, [1 + (2\mu E/I\,\omega_o^2) \sin\psi]^{-1/2} \, d\psi}{\int_0^{2\pi} [1 + (2\mu E/I\,\omega_o^2) \sin\psi]^{-1/2} \, d\psi}$$

and when $(2\mu E/I\,\omega_o^2) \ll 1$ (low fields), reduction leads to

$$\bar{\mu}_1 = -\frac{\mu^2 E}{I\omega_o^2} \frac{\int_0^{2\pi} \sin^2\psi \, d\psi}{\int_0^{2\pi} d\psi} = -\frac{\mu^2 E}{2I\omega_o^2} \tag{20}$$

2) Axis of Rotation is Parallel to the Field

In this case the effect of the interaction of the electric dipole moment with the electric field causes the dipole to tilt in the field direction. Hence, the rotational motion is one of precession. From Fig. 13, it is seen that

$$\sin\alpha = \bar{\mu}_2/\mu$$

and when $\alpha$ is small (low fields)

$$\bar{\mu}_2 = \mu\,\alpha \tag{21}$$

Upon equating the centrifugal force with the electrostatic force

$$\cos\alpha \simeq \alpha = \frac{qE}{m_1\omega_o^2 d_1} = \frac{qE}{m_2\omega_o^2 d_2}$$

Since $I = m_1 d_1 (d_1+d_2) = m_2 d_2 (d_1+d_2)$ ,

Eq. (21) becomes

$$\bar{\mu}_2 = \frac{\mu^2 E}{I\omega_o^2} \tag{22}$$

To obtain a general expression for $\bar{\mu}$ as a function of an arbitrary angle of inclination $\phi$ of the axis of rotation with the field axis, $\bar{\mu}$ is written as

$$\bar{\mu} = \bar{\mu}_1 \sin \phi + \bar{\mu}_2 \cos \phi$$

Hence,

$$\bar{\mu} = - \frac{\mu^2 E}{2I\omega_o^2} \sin^2 \phi + \frac{\mu^2 E}{I\omega_o^2} \cos^2 \phi = \frac{\mu^2 E}{2I\omega_o^2} (3 \cos^2 \phi - 1) \qquad (23)$$

2. Intensity Distribution in the Undeflected Beam

The beam profile in the deflection experiments is determined by an apparent source slit, collimator, and detector slit. The apparent source slit and detector slit were introduced in order to maintain the same beam profile in all of the deflection experiments. Consider Fig. 14 on page 79. In the limit where the detector is infinitely narrow, the beam shape is given by the following equations[41,42]:

$$I_o(s) = I_{oo} \frac{d+s}{d-p} \quad ; \quad -d \leq s \leq -p$$

$$I_o(s) = I_{oo} \quad ; \quad -p \leq s \leq p$$

$$I_o(s) = I_{oo} \frac{d-s}{d-p} \quad ; \quad p \leq s \leq d$$

$I_o(s)$ is the beam intensity per unit detector width at the detector position $s$, and $I_{oo}$ is the intensity per unit detector width when

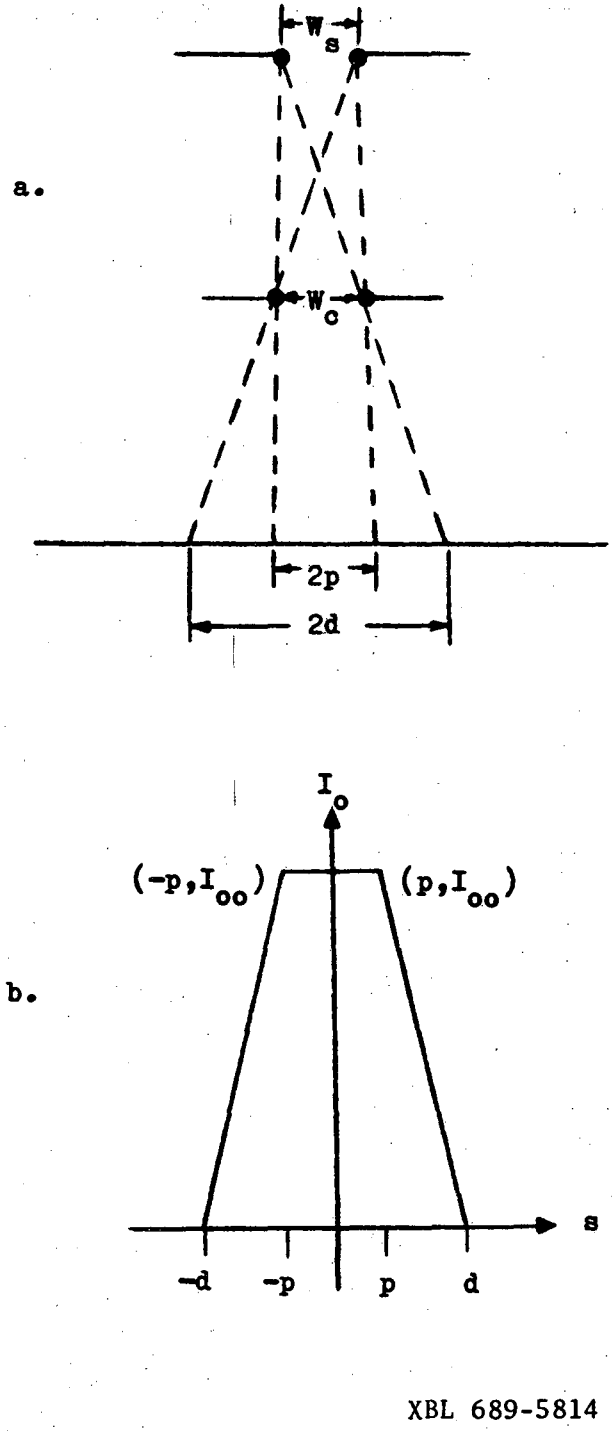


Fig. 14. (a) Relation of source and collimator widths to beam shape. (b) Beam shape with detector of negligible width.

no collimator is present. Constants p and d characterize the profile and are given by

$$p = 1/2 \left| w_c + (w_c - w_s)\, a \right|$$

$$d = 1/2 \left[ w_c + (w_c + w_s)\, a \right]$$

$$a \equiv l_{cd}/l_{sc}$$

$w_c$ = collimator slit width

$w_s$ = apparent source slit width

$l_{cd}$ = distance from collimator to detector slit

$l_{sc}$ = distance from apparent source slit to collimator

The actual beam profile is determined by integration over the present detector width of 0.0127 cm. Experimental profiles were taken by moving the detector across the beam and measuring the particle intensity as a function of detector position. Figure 15 gives a comparison of the calculated and experimental beam profiles.

## 3. Intensity Distribution in the Deflected Beam[3,4,40]

The intensity of the undeflected beam will be diminished upon passage through an inhomogeneous electric field due to the interaction of the electric dipole moment with the electric field. The deflection s suffered by the molecule in the field depends on its translational and rotational distributions, and the orientational distribution of the

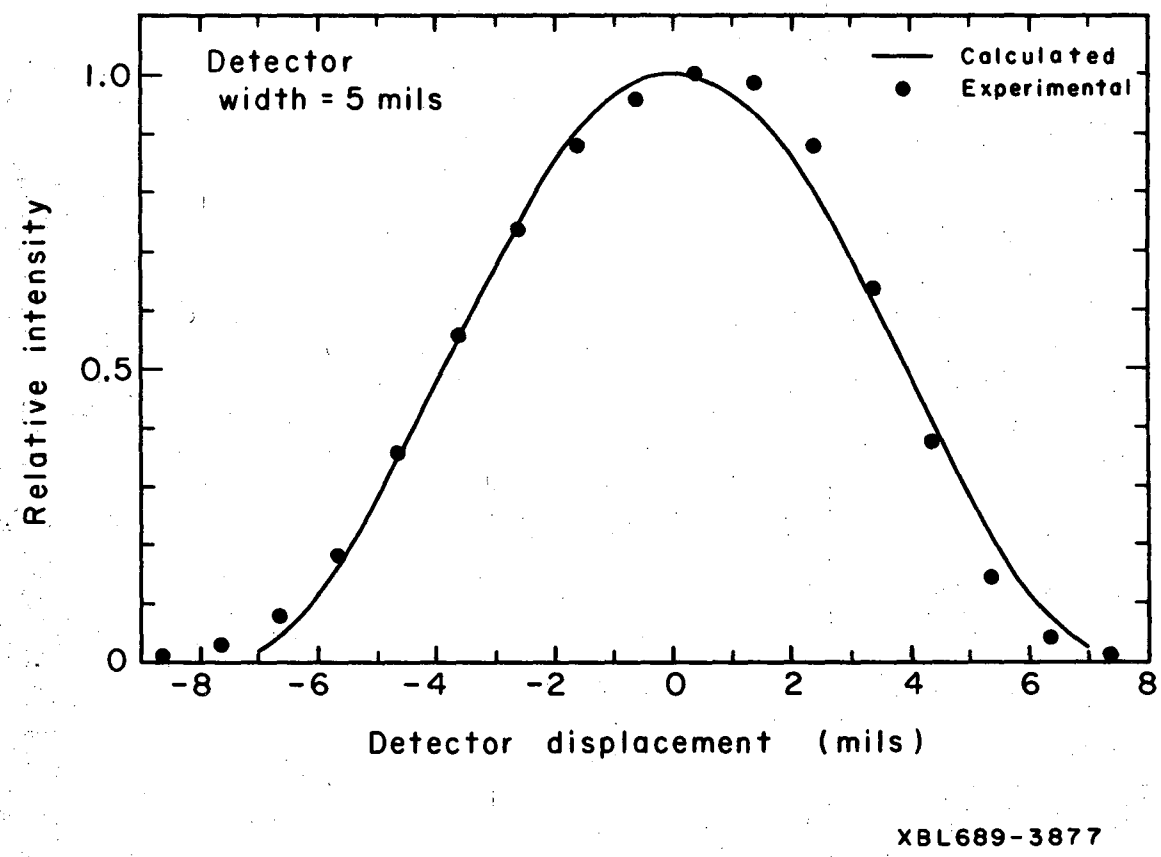


Fig. 15. Comparison of beam profiles.

dipole in the field. The force exerted on the molecule due to the electric field is given by

$$\vec{F} = - \vec{\nabla} W$$

where $W$ is the energy. For the force along the direction of the gradient,

$$F_x = - (\partial W/\partial x) = - (\partial W/\partial E)(\partial E/\partial x) = + \bar{\mu} (\partial E/\partial x)$$

where $\bar{\mu}$ is the effective dipole moment and $E$ is the field strength. The acceleration of the molecule is then

$$a = F/m = \bar{\mu}/m \, (\partial E/\partial x)$$

It follows that the deflection $s$ is given by

$$s = 1/2 \; a \; t^2 = 1/2 \; \bar{\mu}/m \; (\partial E/\partial x) \; \frac{l^2}{v^2} \qquad (24)$$

where $l$ is the length of the trajectory followed by a molecule of velocity $v$. Upon substituting Eq. (23) into Eq. (24), the following expression is obtained:

$$s = \frac{\mu^2 E}{4 I m \omega_o^2} (\partial E/\partial x)(3 \cos^2 \phi - 1) \frac{l^2}{v^2}$$

$$= \frac{\mu^2}{16 \, W_r \, W_v} E(\partial E/\partial x)(3 \cos^2 \phi - 1) \, l^2$$

$$= C \frac{(3 \cos^2 \phi - 1)}{W_r \, W_v} \qquad (25)$$

where

$$C = \frac{\mu^2}{16} E(\partial E/\partial x)\, l^2$$

$$= \frac{2}{16} E(\partial E/\partial x)\, l_B(l_B + 2\, l_2)$$

for a detector placed a distance $l_2$ behind a field of length $l_B$. $W_\nu$ is the translational energy, and $W_r$ is the rotational energy.

Thus, the intensity distribution in the deflected beam must be determined by a consideration of orientational, translational, and rotational effects. In this section, theoretical expressions are derived for the deflected beam shape. First, the deflected beam shape will be given for the case where all three of the above variables are present, and then, it will be shown how elimination of the effect of the translational distribution alters the picture. Finally, the effects of low temperature, molecular polarizability, and transmission of the velocity selector, will be considered. The widths of the beam and detector are assumed to be infinitesimal.

Case 1: Orientational, Rotational, and Translational Distributions

1) For a thermal distribution in velocities, the probability that a molecule in the source will arrive at the detector with a velocity between $\nu$ and $\nu + d\nu$ is given by

$$P(\nu)\, d\nu = 2\, \frac{\nu^3}{\alpha^4} \exp\left(-\frac{\nu^2}{\alpha^2}\right) d\nu \qquad (26)$$

Since $W_\nu = 1/2\ m\ v^2$ , and $\alpha = (2kT/m)^{1/2}$ ,

the probability $P(W_\nu)\ dW_\nu$ that a molecule in the source will arrive at the detector with translational energy between $W_\nu$ and $W_\nu + dW_\nu$ is

$$P(W_\nu)\ dW_\nu = (W_\nu/kT)\ \exp(-W_\nu/kT)\ d(W_\nu/kT) \tag{27}$$

2) For a thermal distribution in rotational energies, the probability $P(W_r)\ dW_r$ that a molecule will arrive at the detector with a rotational energy between $W_r$ and $W_r + dW_r$ is, in the case of high temperatures,

$$P(W_r)\ dW_r = \exp(-W_r/kT)\ d(W_r/kT) \tag{28}$$

3) The probability that $\phi$ lies between $\phi$ and $\phi + d\phi$ is derived from geometrical considerations. The sign of $(3\cos^2\phi - 1)$ determines whether the molecule will be deflected toward or away from the field gradient in an inhomogeneous electric field. Only the values of $\phi$ between 0 and $\pi/2$ need here be considered since the direction of $\bar{\mu}$ is independent of the direction of the rotational motion. Upon taking $s$ to be positive in the direction of increasing field gradient,

$s > 0$ when $1/3 < p^2 \leq 1$

$s < 0$ when $0 \leq p^2 < 1/3$

where $p = \cos\phi$. The probability that $\phi$ lies between $\phi$ and $\phi + d\phi$ is the ratio of the area of the zone of a unit sphere between co-latitudes $\phi$ and $\phi + d\phi$, to half the area of a sphere. Hence

$$P(\phi)\, d\phi = \frac{2\pi \sin\phi}{2\pi}\, d\phi = \sin\phi\, d\phi = -\, dp \tag{29}$$

If $s_o$ is defined as the deflection corresponding to $\phi = 0$ and $\nu = (2kT/m)^{1/2}$, the most probable source velocity, then

$$s_o = 2C/(kT)^2 \tag{30}$$

Upon defining the deflection in terms of a dimensionless variable $\sigma$,

$$\sigma = s/s_o = (kT)^2\, (3p^2-1)/2W_r\, W_\nu \tag{31}$$

Setting $y = W_\nu/kT$ and solving for $W_r$ in terms of $\sigma$,

$$W_r = kT\, (3p^2-1)/2y\sigma$$

and

$$dW_r = -\, kT\, (3p^2-1)/2y\sigma^2\, d\sigma$$

It results that the probability $P(\sigma)\, d\sigma$ that $\sigma$ lies between $\sigma$ and $\sigma + d\sigma$ is

$$P(\sigma)\, d\sigma = \int_{p_1}^{p_2} dp \int_0^\infty \exp\left[-(3p^2-1)/2y\sigma\right] (3p^2-1)/2y\sigma^2 \times y \exp(-y)\, dy\, d\sigma \tag{32}$$

where for $\sigma > 0$ ; $p_1 = 1/3$, $p_2 = 1$

$\sigma < 0$ ; $p_1 = 0$ , $p_2 = 1/3$

The expression $P(\sigma)\, d\sigma$ has been numerically integrated by Feierabend.[40]

As mentioned earlier, several investigators attempted to determine dipole moments of polar molecules by deflecting beams of molecules with both thermal rotational and translational distributions present.[3,4] Quite apart from the difficulties admitted by deflecting such a multitude of states, additional problems result from inadequate knowledge of the composition of the beam under the conditions of the experiments. Assuming that the beam is multi-component and the composition is known, then there is the problem of interpreting data which has an additional distribution (components of the beam) superimposed upon the rotational and translational distributions. Even if a single component beam is analyzed, deflecting different velocity components through different trajectories would smear the beam out, thus yielding results of questionable significance.

Case 2: Orientational and Rotational Distributions

In this case the beam is assumed to be velocity selected. The distribution in $W_\nu$ is no longer present and we are left with only the orientational and rotational distributions. As before

$$P(W_r)\, dW_r = \exp(-W_r/kT)\, d(W_r/kT)$$

$$p(\phi)\, d\phi = -\, dp$$

For the velocity selected beam,

$$s = 1/8 \frac{\mu^2 E}{m} (\partial E/\partial x) \frac{l^2}{\nu^2} \frac{3\cos^2\phi - 1}{W_r} = C \frac{3\cos^2\phi - 1}{W_r} \qquad (33)$$

where

$$C = 1/8 \frac{\mu^2 E}{m} (\partial E/\partial x) \frac{l^2}{\nu^2} \quad .$$

If $s_o$ is now taken to be the deflection corresponding to $\phi = 0$, $\nu = \nu$, and $W_r = kT$, then

$$s_o = 2C/kT \qquad (34)$$

and

$$\sigma = s/s_o = 1/2\ (3\cos^2\phi - 1)/(W_r/kT) \qquad (35)$$

whence

$$W_r = (kT/2) \frac{3p^2 - 1}{\sigma}$$

$$dW_r = -(kT/2) \frac{3p^2 - 1}{\sigma^2} d\sigma$$

Hence, the probability $P(\sigma)\, d\sigma$ that $\sigma$ lies between $\sigma$ and $\sigma + d\sigma$ is

$$P(\sigma)\, d\sigma = \int_{p_1}^{p_2} \exp\left(-\frac{3p^2 - 1}{2\sigma}\right) - \left(\frac{3p^2 - 1}{2\sigma^2}\right) d\sigma\ (-dp) \qquad (36)$$

and

$$p(\sigma) = \int_{p_1}^{p_2} \left(\frac{3p^2 - 1}{2\sigma^2}\right) \exp - \left(\frac{3p^2 - 1}{2\sigma}\right) dp \qquad (37)$$

which is the general expression for $P(\sigma)$ in this case.

Before integrating Eq. (37), let us define $\sigma_{left}$ as the deflection corresponding to $\sigma < 0$. Then

$$\sigma_{left} = s_{left}/s_o = (kT/2)\,\frac{1 - 3p^2}{W_r} \geq 0$$

$$\sigma_{left} = -\sigma = \sigma_L$$

Then

$$W_r = (kT/2)\,\frac{1 - 3p^2}{\sigma_L}$$

and

$$dW_r = -(kT/2)\,\frac{1 - 3p^2}{\sigma_L^2}\,d\sigma_L$$

Hence, for a deflection corresponding to $\sigma < 0$, the expresion for $P(\sigma_L)$ becomes

$$P(\sigma_L) = \int_{p_1}^{p_2} \frac{1 - 3p^2}{2\sigma_L^2} \exp\left(-\frac{1 - 3p^2}{2\sigma_L}\right) dp \quad ; \quad p_1 = 0,\ p_2 = 1/3 \qquad (38)$$

For deflection to the right, i.e., for $\sigma > 0$,

$$\sigma_{right} = s_{right}/s_o = (kT/2)\,\frac{3p^2 - 1}{W_r} \geq 0$$

$$\sigma_{right} = +\sigma = \sigma_R$$

then

$$W_r = (kT/2)\,\frac{3p^2 - 1}{\sigma_R}$$

$$dW_r = -(kT/2)\,\frac{3p^2 - 1}{\sigma_R^2}\,d\sigma_R$$

and $P(\sigma_R)$ becomes

$$P(\sigma_R) = \int_{p_1}^{p_2} \frac{3p^2 - 1}{2\sigma_R^2} \exp\left(-\frac{3p^2 - 1}{2\sigma_R}\right) dp \quad ; \quad p_1 = 1/3,\ p_2 = 1 \qquad (39)$$

Upon integrating Eqs. (38) and (39), we obtain

$$P(\sigma_R) = \frac{1}{\sqrt{12}} \frac{1}{\sigma_R} \left[ \sqrt{\frac{2}{\sigma_R}} (\sigma_R - 1) \frac{\sqrt{\pi}}{2} \left\{ \exp \frac{1}{2\sigma_R} \right\} \right.$$

$$\left. \times \left( \operatorname{erf} \sqrt{\frac{3}{2\sigma_R}} - \operatorname{erf} \sqrt{\frac{1}{2\sigma_R}} \right) - \sqrt{3} \left\{ \exp\left( - \frac{1}{\sigma_R} \right) \right\} + 1 \right] \quad (40)$$

$$P(\sigma_L) = \frac{1}{\sqrt{12}} \frac{1}{\sigma_L} \left[ \sqrt{\frac{2}{\sigma_L}} (\sigma_L + 1) \left( \mathrm{Daw} \sqrt{\frac{1}{2\sigma_L}} \right) - 1 \right] \quad (41)$$

where $\operatorname{erf}(z) = \frac{2}{\sqrt{\pi}} \int_0^z \exp(-t^2)\, dt$

and $\mathrm{Daw}(z) = \exp(-z^2) \int_0^z \exp(t^2\, dt$

Values of $P(\sigma)$ were computed using tables of the error function and Dawson's function and are tabulated in Table XVII. Figure 16 is a plot of $P(\sigma)$ for the second case, and Fig. 17 exhibits a comparison of the deflected beam shape for the two cases. It is seen that the $P(\sigma)$ curve for Case 1 is more localized about the center position ($\sigma = 0$), than the $P(\sigma)$ curve for Case 2, due to the effect of the velocity distribution. In both cases the maximum of the deflected curve is close to the position of the undeflected beam. The area under the curves corresponding to $\sigma > 0$ and $\sigma < 0$ indicate that the average effective dipole moment is larger for those rotational states which have had their rotational energies decreased in the field, i.e., for $\sigma > 0$. The effect observed in a deflection experiment is seen to be a decrease in the intensity of the maximum and a spreading out of the

Table XVII. Results of $P(\sigma)$ calculations for a velocity selected molecular beam.

| $\sigma$ | $P(\sigma)$ | $\sigma$ | $P(\sigma)$ |
|---|---|---|---|
| -0.02 | 0.6024 | 0.02 | 0.5604 |
| -0.03 | 0.6179 | 0.03 | 0.5476 |
| -0.04 | 0.6356 | 0.04 | 0.5362 |
| -0.05 | 0.6570 | 0.05 | 0.5303 |
| -0.06 | 0.6822 | 0.06 | 0.5231 |
| -0.07 | 0.7101 | 0.07 | 0.5141 |
| -0.08 | 0.7386 | 0.08 | 0.5074 |
| -0.09 | 0.7648 | 0.09 | 0.5004 |
| -0.10 | 0.7873 | 0.10 | 0.4947 |
| -0.15 | 0.8370 | 0.15 | 0.4638 |
| -0.20 | 0.7764 | 0.20 | 0.4313 |
| -0.25 | 0.6930 | 0.25 | 0.3967 |
| -0.30 | 0.5991 | 0.30 | 0.3616 |
| -0.35 | 0.5283 | 0.35 | 0.3276 |
| -0.40 | 0.4604 | 0.40 | 0.2965 |
| -0.45 | 0.4030 | 0.45 | 0.2665 |
| -0.50 | 0.3547 | 0.50 | 0.2431 |
| -0.55 | 0.3138 | 0.55 | 0.2208 |
| -0.60 | 0.2791 | 0.60 | 0.2010 |
| -0.65 | 0.2497 | 0.65 | 0.1834 |
| -0.70 | 0.2245 | 0.70 | 0.1679 |
| -0.75 | 0.2029 | 0.75 | 0.1542 |
| -0.80 | 0.1841 | 0.80 | 0.1420 |
| -0.85 | 0.1677 | 0.85 | 0.1311 |
| -0.90 | 0.1534 | 0.90 | 0.1213 |
| -0.95 | 0.1407 | 0.95 | 0.1126 |
| -1.00 | 0.1297 | 1.00 | 0.1047 |
| -1.10 | 0.1110 | 1.10 | 0.0912 |

(continued)

Table XVII. Continued.

| σ | P(σ) | σ | P(σ) |
|---|---|---|---|
| -1.20 | 0.0962 | 1.20 | 0.0801 |
| -1.30 | 0.0840 | 1.30 | 0.0709 |
| -1.40 | 0.0741 | 1.40 | 0.0632 |
| -1.50 | 0.0656 | 1.50 | 0.0566 |
| -1.60 | 0.0587 | 1.60 | 0.0510 |
| -1.70 | 0.0526 | 1.70 | 0.0462 |
| -1.80 | 0.0476 | 1.80 | 0.0420 |
| -1.90 | 0.0432 | 1.90 | 0.0384 |
| -2.00 | 0.0394 | 2.00 | 0.0352 |
| -2.20 | 0.0332 | 2.20 | 0.0299 |
| -2.40 | 0.0282 | 2.40 | 0.0257 |
| -2.60 | 0.0245 | 2.60 | 0.0224 |
| -2.80 | 0.0214 | 2.80 | 0.0196 |
| -3.00 | 0.0187 | 3.00 | 0.0173 |
| -3.50 | 0.0140 | 3.50 | 0.0131 |
| -4.00 | 0.0110 | 4.00 | 0.0103 |
| -4.50 | 0.0086 | 4.50 | 0.0083 |
| -5.00 | 0.0071 | 5.00 | 0.0068 |
| -5.50 | 0.0060 | 5.50 | 0.0057 |
| -6.00 | 0.0050 | 6.00 | 0.0048 |
| -8.00 | 0.0029 | 8.00 | 0.0028 |
| -10.00 | 0.0018 | 10.00 | 0.0018 |
| -12.00 | 0.0013 | 12.00 | 0.0013 |
| -18.00 | 0.0006 | 18.00 | 0.0006 |
| -25.00 | 0.0003 | 25.00 | 0.0003 |

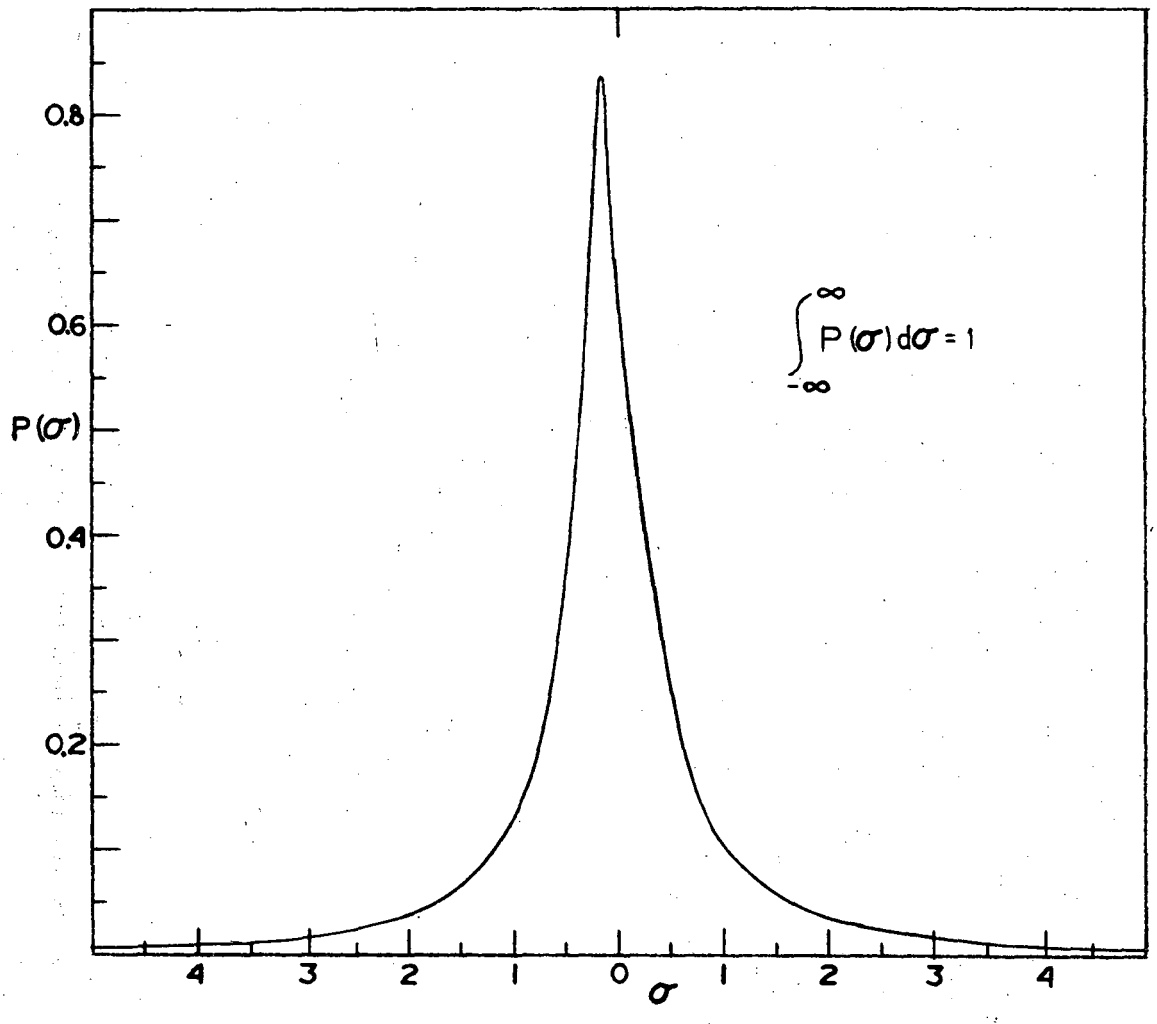


XBL 689-5815

Fig. 16. Plot of $P(\sigma)$ vs $\sigma$ for a velocity selected beam of molecules.

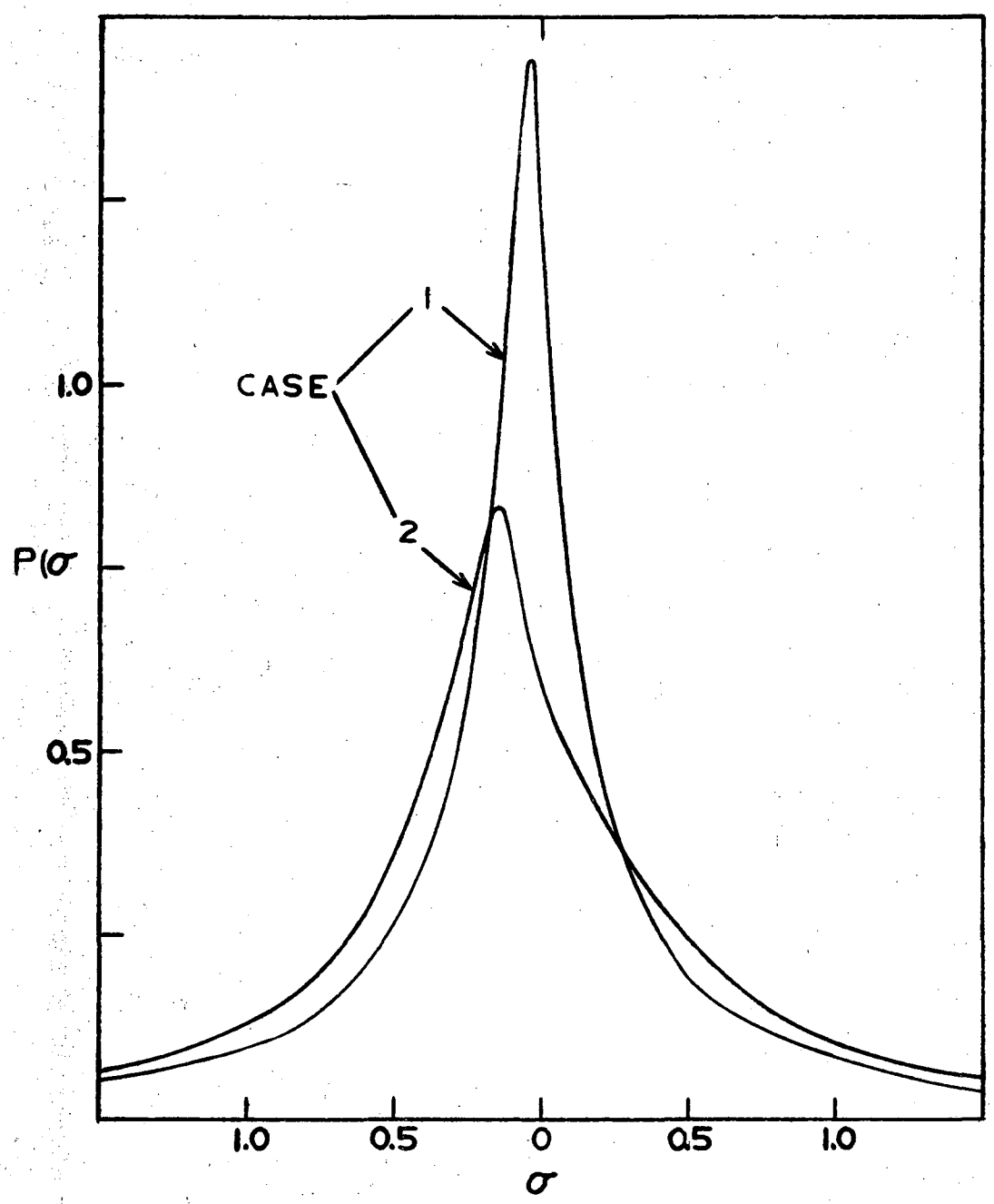


XBL 689-5816

Fig. 17. Comparison of P(σ) distributions for a Maxwellian distribution of velocities (Case 1) and for a velocity selected beam (Case 2).

undeflected beam. Since for Case 2 the translational energy is known from velocity selection and since the diminution in intensity of the undeflected beam is more sensitive to the deflecting field strength, it is expected that the results of a deflection analysis for Case 2 gives more pronounced details of the dipole-electric field interaction, than that for Case 1.

Case 3: Effect of Low Temperatures

At low temperatures, the approximation that the distribution of rotational energy states can be described by the equations of classical mechanics is not valid. The preponderance of rotational states of low energy necessitates a quantum mechanical treatment. The Schroedinger equation for a diatomic molecule in an electric field $E$, in the rigid rotor approximation, is

$$\left(\frac{\hbar^2}{2I} J^2 - \vec{\mu}\cdot\vec{E}\right) \psi = W_r \psi$$

where $J$ is the angular momentum in field-free space. If we let $\vec{E}$ be along the $z$ coordinate, then

$$\left(\frac{\hbar^2}{2I} J^2 - \mu E \cos\theta\right) \psi(\theta,\phi) = W_r \psi(\theta,\phi) \qquad (42)$$

Upon writing $\lambda = \dfrac{\mu E}{\hbar^2/2I}$ and $W = \dfrac{W_r}{\hbar^2/2I}$, then Eq. (42) becomes

$$\left[\frac{1}{\sin\theta}\frac{\partial}{\partial\theta}\left(\sin\theta\,\frac{\partial}{\partial\theta}\right) + \frac{1}{\sin^2\theta}\frac{\partial^2}{\partial\phi^2}\right]\psi + (W - \lambda\cos\theta)\,\psi = 0 \qquad (43)$$

For $\lambda<<1$ (weak electric fields), perturbation theory gives, to second order, the result

$$W^{(2)} = \frac{\lambda^2}{2}\left[\frac{J(J+1) - 3M_J^2}{J(J+1)(2J-1)(2J+3)}\right]$$

Hence,

$$\bar{\mu}(J,M_J) = -\frac{\partial W_r}{\partial E} = \frac{\mu^2 E}{\hbar^2/2I}\left[\frac{3M_J^2 - J(J+1)}{J(J+1)(2J-1)(2J+3)}\right] \tag{44}$$

In this case, the deflection $s(J,M_J)$ suffered by a molecule in the rotational state $(J,M_J)$ is

$$s(J,M_J) = \frac{\mu^2 E}{2m(\hbar^2/2I)}\left[\frac{3M_J^2 - J(J+1)}{J(J+1)(2J-1)(2J+3)}\right]\frac{\partial E}{\partial z}\frac{l^2}{v^2} \tag{45}$$

The probability that the molecule has rotational energy $W_r$ is

$$P_{J,M_J} = \frac{\exp(-W_r/kT)}{\sum_{J,M_J}\exp(-W_r/kT)} \tag{46}$$

where the summation is taken over all the states accessible to the system, and energy differences of states with the same $J$ but different $M_J$ have been neglected.

Since the angular momentum $J$ can assume only definite orientations $\phi$ relative to the field axis such that $\cos\phi = M_J/\sqrt{J(J+1)}$, then in Case 1, the only continuously varying quantity is the distribution in the translational energy. For Case 2, no distribution in $W_v$ is present, and only the lower rotational states are significantly populated. Thus, for low temperatures,

Case 2 allows a relatively simple experimental determination of the dipole moment by a deflection analysis. The experimental arrangement for such an analysis would involve moving the surface ionization detector a measured amount $s(J,M_J)$ off the beam axis, and measuring the voltage required to refocus the individual rotational states.

For Case 1, the effect of the translational distribution on a deflection $s_o(J,M_J)$ must be considered for each rotational state $(J,M_J)$. Hence, for each $(J,M_J)$ state, $s_o(J,M_J)$ is defined as the deflection corresponding to the most probable source velocity $\alpha$. Once again, the probability that a molecule with a velocity in the source between $v$ and $v + dv$ will arrive at the detector with a velocity between $v$ and $v + dv$ is

$$P(v)\,dv = \frac{2}{\alpha^4} v^3 \exp(-v^2/\alpha^2)\,dv \tag{47}$$

The deflection $s$ experienced by a molecule is

$$s = s_o \frac{\alpha^2}{v^2}$$

$$2v^3\,dv = -\left(\frac{s_o^2}{s^3}\right)\alpha^4\,ds$$

For the state $(J,M_J)$

$$2v^3\,dv = -\frac{[s_o(J,M_J)]^2}{[s(J,M_J)]^3}\,\alpha^4\,ds(J,M_J) \tag{48}$$

Upon substituting Eq. (48) into Eq. (47)

$$[P(s)\,ds]_{J,M_J} = -\frac{[s_o(J,M_J)]^2}{[s(J,M_J)]^3}\exp\left(-\frac{s_o(J,M_J)}{s(J,M_J)}\right)ds(J,M_J) \quad (49)$$

Then, if $\sigma$ is defined as

$$\sigma = s(J,M_J)/s_o(J,M_J) \quad (50)$$

it results that

$$P(\sigma)\,d\sigma = \pm\frac{1}{\sigma^3}\exp(-1/\sigma)\,d\sigma \quad (51)$$

The $\pm$ sign is introduced to enable $P(\sigma)$ to be always positive, since it would be negative for $\sigma > 0$. Upon introducing the weighting factor $P_{J,M_J}$, $P(\sigma)$ becomes

$$P(\sigma) = \pm P_{J,M_J}\frac{1}{\sigma^3}\exp(-1/\sigma) \quad (52)$$

Estermann and Fraser,[3] in an experiment on HCl, observed that even at low temperatures, there is still a single maximum present in the $P(\sigma)$ distribution. Consequently, it is expected that the results of a deflection analysis without a velocity selector, will yield only semi-quantitative information.

Case 4: Correctional terms--Polarizability, Transmission of The Velocity Selector

Polarizability. Since the electronic structure of a molecule is not rigid, an electric field may induce a dipole moment in the molecule which tends to be directed along the field axis. The magnitude of this induced dipole depends on the field strength. It is the

effect on the $P(\sigma)$ curves, of the deflection due to this induced dipole, which is now considered.

For Case 1, if $s$ is defined as the deflection of a molecule due to polarizability $\alpha_E$ and induced moment $\mu_\alpha$, then

$$s = 1/2 \frac{\mu_\alpha}{m} \left(\frac{\partial E}{\partial z}\right) \frac{l^2}{v^2} \tag{53}$$

In the same manner in which Eq. (51) was derived,

$$P_\alpha(\sigma)\, d\sigma = \pm \frac{1}{\sigma^3} \exp(-1/\sigma)\, d\sigma \tag{54}$$

where $P_\alpha(\sigma)\, d\sigma$ is the probability of the occurrence of deflections (due to $\mu_\alpha$) between $\sigma$ and $\sigma + d\sigma$,

$$\sigma = s/s_o \tag{55}$$

and $s_o$ is the deflection corresponding to $W_v = kT$. Hence, an additional distribution due to the deflection of the induced dipole must be added to the distribution due to the deflection of the permanent dipole. The effect of the deflection due to the polarizability is to shift the $P(\sigma)$ curves toward the right.

For Case 2, the effect of the polarizability is the same. This effect may be incorporated into the calculation of $s_o$ in both cases. Then,

$$s_o' = s_o + 1/2 \frac{\mu_\alpha}{m} \left(\frac{\partial E}{\partial z}\right) \frac{l^2}{v^2} \tag{56}$$

The method of accounting for the effect of the polarizability in the above manner may be used for the low temperature case.

Transmission of the Velocity Selector. Although the presence of a velocity selector eliminates uncertainty in the trajectory of the deflected beam arising from a thermal velocity distribution, there is still a small velocity spread due to the transmission of the velocity selector. This effect is small and calculations indicate that it is negligible.

## 4. Determination of Dipole Moments

The manner of determining the dipole moment of linear polar molecules by deflecting a velocity selected molecular beam will be demonstrated in this section. The theoretical deflected beam shape applicable to the present experiments has been outlined in Case 2 of Sect. IV-B. So far, the beam and detector widths have been assumed to be infinitesimal. It is necessary, therefore, to integrate the theoretical expression for the deflected beam shape over the undeflected beam shape. The undeflected beam shape used here is the beam profile which is calculated from the equations on page 78. As illustrated in Fig. 15, the calculated profile is close to the experimental profile. Of course, the actual beam width is determined by the detector width.

In terms of $\sigma$ units, the equations which describe the undeflected beam are

$$f(\sigma \pm \sigma_o) = \frac{d/s_o + (\sigma \pm \sigma_o)}{d/s_o - p/s_o} \quad ; \quad -d/s_o \leq (\sigma \pm \sigma_o) \leq -p/s_o \qquad (57)$$

$$f(\sigma \pm \sigma_o) = 1 \quad ; \quad -p/s_o \leq (\sigma \pm \sigma_o) \leq p/s_o \tag{58}$$

$$f(\sigma \pm \sigma_o) = \frac{d/s_o - (\sigma \pm \sigma_o)}{d/s_o - p/s_o} \quad ; \quad p/s_o \leq (\sigma \pm \sigma_o) \leq d/s_o \tag{59}$$

where $s_o \cdot \sigma_o$ is the detector position in centimeters. The equation which defines the deflected beam shape is then

$$F(\sigma_o) = \int f(\sigma \pm \sigma_o)\, P(\sigma)\, d\sigma \tag{60}$$

where the center of the beam is assumed to be coincident with the center position of the detector at $\sigma_o = 0$. After numerical integration of Eq. (60), $F(\sigma_o)$ vs $\sigma_o$ is plotted for each value of $s_o$ used. The area under each curve corresponds to the detected intensity $I$ after deflection in the electric field region. The area under the trapezoidal beam shape, cut off by the width of the detector, corresponds to the detected intensity $I_o$ with the field off. A plot of $I/I_o$ vs $s_o$ is given in Fig. 20. This plot demonstrates the manner in which the dipole moment may be determined. It is only nececessary to measure the undeflected and the deflected beam intensity and calculate the dipole moment from the corresponding value of $s_o$.

## C. Deflection of Triatomic Molecules

### 1. The Stark Effect

The theory for the deflection of linear molecules applies generally for diatomic molecules without further clarification. However, in the case of triatomic and other linear polyatomic molecules, the effect of bending vibrational modes signals the need for an additional picture of the details of the dipole-field interaction. The linear triatomic molecule lends itself to the simplest explanation, and it will be discussed here in detail.

A linear triatomic molecule possesses three vibrational modes in the form of two stretching modes along the internuclear axis, and a doubly degenerate off-axis bending mode. The stretching modes introduce nothing new insofar as the theory of the deflection experiments is concerned, but the effect of the bending mode may alter the situation considerably.[43] When the bending vibration introduces angular momentum about the internuclear axis, the total rotational angular momentum J becomes the sum of the angular momentum due to the end-over-end rotational motion of the molecule and the angular momentum which is derived from the bending vibration. Classically, this additional angular momentum arises from a phasing of the degenerate vibrational motions such that the resulting motion is that of the nuclei executing a circular or elliptical orbit which is perpendicular to a straight line joining the centers of the nuclei. A quantum mechanical analysis of such a system shows that the energy associated with this "internal angular momentum l" is $h\nu_2(v+1)$, where $\nu_2$ is the bending vibrational

frequency and $v$ is the total vibrational quantum number in the bending mode. The angular momentum $l$ (units of $\hbar$) can take on values

$$l = v, v-2, v-4, \ldots, -v$$

where $|l| \leq J$.

The effect of angular momentum about the symmetry axis of a linear molecule, due to the degenerate vibration, is to cause the molecule to behave in a manner very similar to a symmetric top. For the present purposes of determining dipole moments of linear triatomic molecules from deflection experiments, it is sufficient to observe that only a fractional number of the molecules which are present in the beam at a particular temperature behave in a manner similar to a symmetric top. These consist of those molecules whose vibrational quantum states have vibrational angular momentum $l \neq 0$. It is obvious that if the vibrational energy is very large in comparison to kT, the states with $l \neq 0$ will not be sufficiently populated to contribute to the beam. In this case the theory outlined for linear molecules is applicable. When the vibrational energy is small in comparison to kT, the population of the excited states may be of sufficient magnitude as to warrant taking them into account. It is this latter effect which is now considered. Here, we also need an expression for the effective dipole moment.

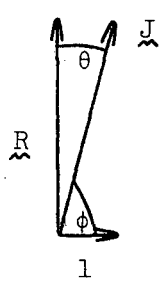

From the diagram above, the total angular momentum squared is given as

$$\underset{\sim}{J}^2 = \underset{\sim}{R}^2 + \underset{\sim}{l}^2$$

The component of the dipole moment along $J$ is then

$$\mu_J = \mu \cos \phi$$

but since $\cos \theta \simeq \frac{l}{J} \simeq \frac{l}{R}$ at high temperatures, then

$$\mu_J = \mu \frac{l}{R}$$

and the effective dipole moment $\bar{\mu}$ is given as

$$\bar{\mu} = \mu_J \cos \theta = \mu \frac{l}{R} \cos \theta$$

In order to obtain an expression for $R$, consider the following equations:

$$W_r = 1/2\ I\omega^2 = \frac{\hbar^2}{2I} R^2$$

where $\omega$ is the rotational frequency and $I$ is the moment of inertia. Hence,

$$R = \frac{l}{\hbar} \sqrt{2IW_r}$$

and finally $\bar{\mu} = \mu \frac{l\hbar}{\sqrt{2IW_r}} \cos \theta$ (61)

which is the desired expression--the effective dipole moment in terms of the permanent dipole moment and the vibrational angular momentum l. It is now only necessary to see what effect the bending vibration has on the intensity distribution in the deflected beam.

## 2. Intensity Distribution in the Deflected Beam

As before, the force exerted on a molecule in an inhomogeneous electric field is

$$F_x = + \bar{\mu} \frac{\partial E}{\partial x}$$

The deflection of the molecule in the field is then

$$s = 1/2\ at^2 = \frac{\bar{\mu}}{m} \frac{\partial E}{\partial x} \frac{l_B(l_B+2l_l)}{2v^2} \tag{62}$$

Upon substituting Eq. (61) into Eq. (62), s becomes

$$s = \frac{l_B(l_B+2l_l)}{2v^2} \frac{\partial E}{\partial x} \frac{\mu\ l \cos}{m \sqrt{2IW_r}}$$

$$= C \frac{l \cos \theta}{\sqrt{W_r}}$$

where

$$C = \frac{l_B(l_B+2l_l)}{2v^2} \frac{\partial E}{\partial x} \frac{\mu}{m \sqrt{2I}}$$

The intensity distribution in the deflected beam will, in this case, depend on orientational, rotational, translational, and vibrational effects. It was demonstrated in Sect. IV-B that quantitative

results could not be expected when the beam was not velocity selected. In this section, a theoretical expression is derived for the intensity distribution in the deflected beam for a velocity selected beam when the bending vibrational energy is small in comparison to kT. The theory for the deflection of diatomic molecules is applicable when the experimental conditions imply that the vibrational energy is large in comparison to kT. When the diatomic theory is applicable, the previous treatment of the low temperature case again applies. The correctional terms, the effect of the polarizability, and the transmission of the velocity selector, are the same as in Sect. IV-B. Once again, the widths of the beam and detector are assumed to be infinitesimal. In passing, it must be remarked that the following treatment assumes that the deflection of those molecules with $l = 0$, which exhibit a second-order Stark effect, is negligible in comparison to the deflection of those molecules with $l \neq 0$, which exhibit a first-order Stark effect.[44] We shall see in part 3 the details of this assumption.

1) The probability $P(W_r)\, dW_r$ that a molecule will arrive at the detector with a rotational energy between $W_r$ and $W_r + dW_r$ is, in the case of high temperatures,

$$P(W_r)\, dW_r = \exp(-W_r/kT)\, d(W_r/kT)$$

2) The probability $P(\theta)\, d\theta$ that $\theta$ lies between $\theta$ and $\theta + d\theta$ is

$$P(\theta)\, d\theta = 1/2 \sin\theta\, d\theta = -\, 1/2\, d(\cos\theta) = -\, 1/2\, dp$$

where $p = \cos\theta$.

If $s_o$ is defined as the deflection corresponding to $\nu = \nu$, $\cos\theta = 1$, $W_r = kT$, and $l = 1$, then the expression $s$ for the deflection becomes

$$s_o = C/\sqrt{kT}$$

and in terms of the dimensionless quantity $\sigma$,

$$\sigma = s/s_o = lp\sqrt{\frac{kT}{W_r}}$$

since $W_r/kT = \frac{l^2p^2}{\sigma^2}$ ,

and $d(W_r/kT) = -\frac{2l^2p^2}{\sigma^3}\,d\sigma$ ,

it results that

$$P(\sigma,l)\,d\sigma = \int_0^l \exp -\left(\frac{l^2p^2}{\sigma^2}\right)\ \frac{l^2p^2}{\sigma^3}\ dp\ d\sigma$$

Upon setting $y^2 = \frac{l^2p^2}{\sigma^2}$ , the probability $P(\sigma,l)$ that a molecule will be deflected through a distance $\sigma$ is

$$P(\sigma,l) = \frac{1}{l}\int_0^{l/\sigma} y^2 \exp(-y^2)\,dy$$

When the above expression is integrated, the final expression for $P(\sigma,l)$ is

$$P(\sigma,l) = \frac{1}{2l}\left[\frac{\sqrt{\pi}}{2}\,\mathrm{erf}(l/\sigma) - \exp(-l/\sigma)^2\right] \quad ; \quad l \neq 0 \qquad (63)$$

The expression $P(\sigma,l)$ must be weighted according to the populations of the various states with a given value of l. The fractional number of molecules with a given value of l is

$$p_l = d \exp(-|l|x) \left[\frac{1 - \exp(-x)}{1 + \exp(-x)}\right]$$

where $d = 1$, when $l = 0$

$d = 2$, when $l \neq 0$

$x = h\nu_2/kT$

and $\nu_2$ = bending vibrational frequency.

When $P_l$ is included in Eq. (63), we obtain

$$P(\sigma) = P_l \, P(\sigma,l) \, , \tag{64}$$

which gives the intensity distribution in the deflected beam.

## 3. Determination of Dipole Moments

The manner of including the effect of finite beam and detector widths follows the same procedure as in the case for diatomic molecules. As remarked earlier, it is assumed that the deflection of those molecules with $l = 0$ is negligible in comparison to those with $l \neq 0$. This assumption derives from 1) the fact that the molecules with $l \neq 0$ exhibit a first-order Stark effect which is much larger than the second-order Stark effect exhibited by the molecules with $l = 0$, and 2) the population of the $l \neq 0$ states, which depends on the Boltzman factor $\exp(-h\nu_2/kT)$, may constitute an appreciable fraction of the total

molecules in the beam. The theoretical calculations from the considerations outlined in part 2 yield values of $I/I_o$ which are due to the molecules with $l \neq 0$. The total $I/I_o$ which is to be compared with experimental results is

$$(I/I_o)_{calc} = (I/I_o)_{l\neq 0} + P_o$$

where $P_o = \frac{1 - \exp(-x)}{1 + \exp(-x)}$, and is the fractional number of molecules in the beam with $l = 0$; these are assumed to be undeflected. The experimental $I/I_o$ takes the form

$$(I/I_o)_{exp} = (I/I_o)_{l\neq 0} + (I/I_o)_{l=0}$$

Since the deflection of those molecules with $l = 0$ may not be completely negligible in comparison to those with $l \neq 0$, then

$$(I/I_o)_{l=0} \leq P_o$$

and

$$(I/I_o)_{exp} \leq (I/I_o)_{calc}, \text{ for a given value of } s_o.$$

The magnitude of the inequality will be determined by the particular molecule investigated and the experimental conditions. The final results, leading to the $I/I_o$ vs $s_o$ curves as in the diatomic case, depend on the particular molecule of interest. The purpose here has been to delineate the theoretical basis for such an experiment. An experiment on CsOH, which has a known value of $\mu$ and $\nu_2$, has been performed and the results are presented here along with the results of the experiments on the alkali halides.

## D. Experimental Techniques

### 1. The Apparatus

The experimental arrangement for the deflection experiments is the same as that described in Sect. III. The 30.48 cm long stainless steel deflecting field has a field configuration conjugate to that of two parallel line charges of opposite sign, separated by a distance 2a.[6] Figures 18 and 19 give end views of the electrodes and critical dimensions. From Fig. 18, the field and field gradient are given by

$$E = 4\ aq/r_1\ r_2$$

$$\frac{\partial E}{\partial x} = -\ 4\ aqx\ (r_1^2 + r_2^2)/r_1^3\ r_2^3$$

where $q$ is the magnitude of either line charge per unit length. Upon evaluation of $\Delta V$, the potential difference between the electrodes, by taking the line integral of the electric field along the median plane, we obtain

$$E = 3.9\ \Delta V\ (\text{esu or V/cm}) \tag{61}$$

$$\frac{1}{E}\frac{\partial E}{\partial x} = 3.1\ (\text{cm}^{-1}) \tag{62}$$

and

$$E\frac{\partial E}{\partial x} = 47.151\ (\Delta V)^2 \tag{63}$$

then,

$$(\text{applied voltage})^2 = (\Delta V)^2 = \frac{1}{47.151}\ E\frac{\partial E}{\partial x} \tag{64}$$

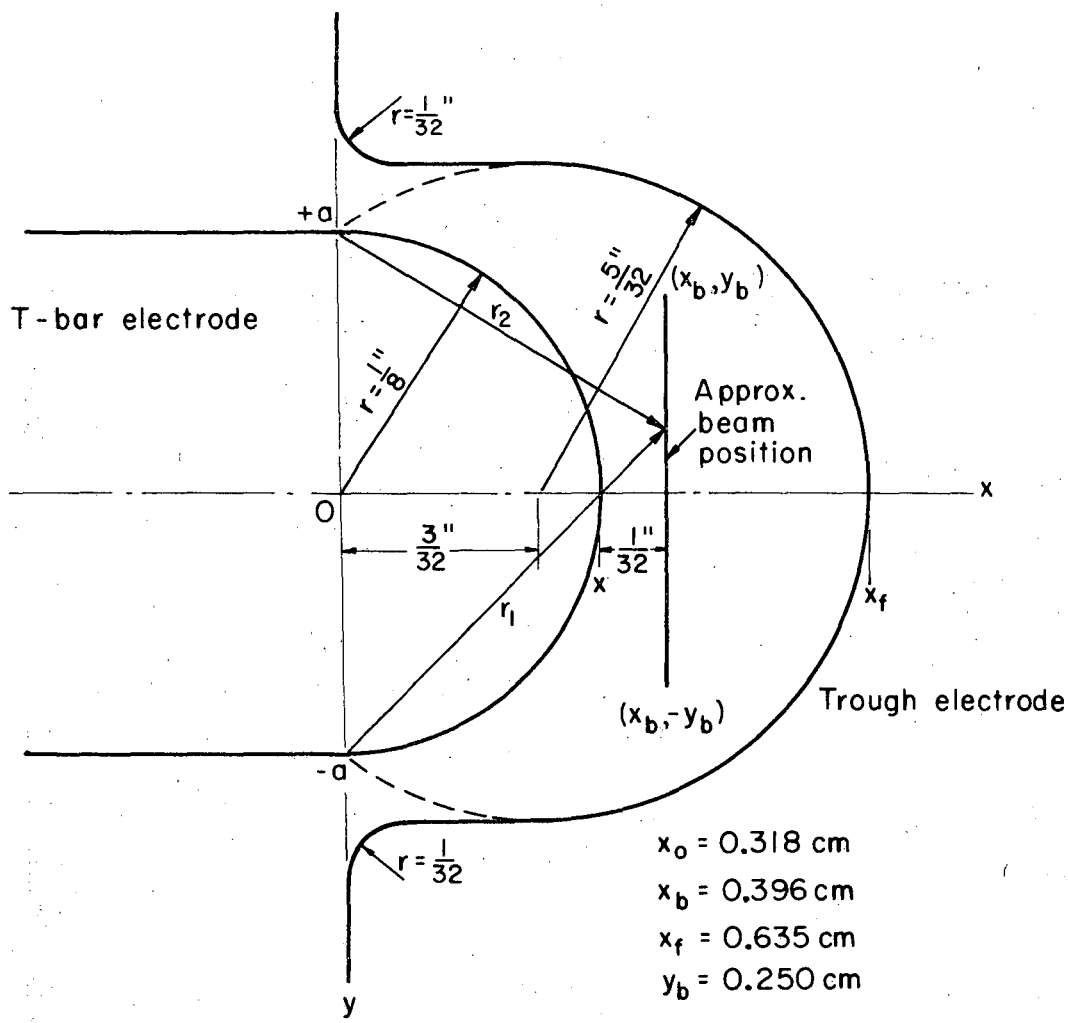


Fig. 18. Deflecting-field electrodes (end view).

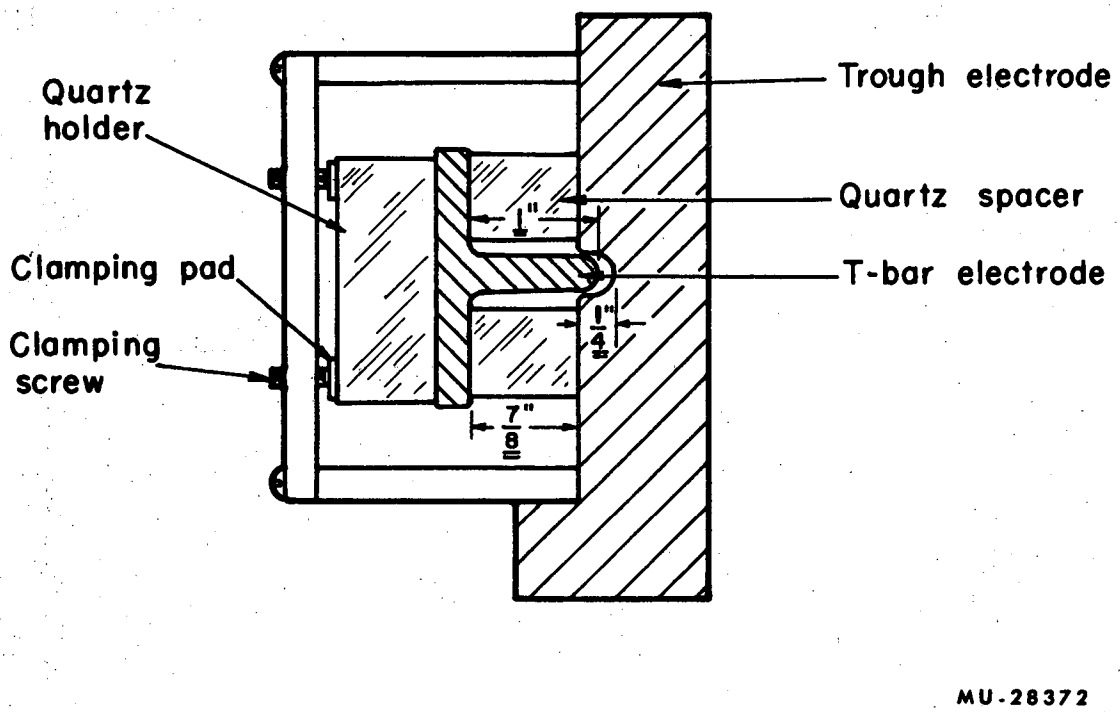


Fig. 19. Deflecting-field assembly (end view).

A (0-10) kV range voltage power supply, with a 20 position switch, was used to supply the potential across the field plates. Calibration was accomplished with a series of different electrostatic voltmeters at the Lawrence Radiation Laboratory meter shop. Voltages at the different switch positions are accurate to better than 1% and are reproducible to better than 0.1%.

In order to calculate the field and field gradient directly from the applied voltage, and thus know the absolute deflection suffered by a molecule, it is necessary that the axis of the beam and the assumed field axis coincide. Since it was not expected that the alignment was perfect, the absolute determination of dipole moments from the theoretical curve, Fig. 20, was not possible. Consequently, dipole moments were determined from experimentally constructed curves.

A single silver oven was used for all CsOH experiments, and the same stainless steel oven was used for all alkali halide experiments. Temperature measurements were taken in the same manner as in Sect. III. Figure 9 is a schematic diagram of the experimental arrangement for the deflection experiments. The beam geometry is defined by three slits--a 0.0127 cm wide × 0.396875 cm high × 0.00254 cm thick buffer slit, a 0.0127 cm wide razor edge main chamber slit, and a detector slit of the same dimensions as the buffer slit located 2.54 cm in front of the hot wire detector. Molecules are detected in the manner described in Sect. II with the positive ion pulses counted by means of a system which includes a fast-count linear amplifier and single channel analyzer, and a H-P 5245L - 5253B electronic counter.

2. The Experiment

Data for the deflection experiments was taken in the following manner. With the velocity selector rotating at a speed corresponding to the transmission of a velocity of $6.06 \times 10^4$ cm/sec, a 60 second count is taken of the undeflected intensity $I_o$, then, the field is turned on and a 60 second count is taken of the deflected intensity $I$; the field is turned off and another 60 second count is taken of the undeflected intensity. If the initial and final values of $I_o$ differ by more than 1% (due to beam fluctuations), the numbers are rejected. Hot wire background counts are measured with the beam flag in (Fig. 3) and subtracted from the measured values of $I$ and $I_o$. Several measurements are taken in this manner, and averaged.

According to the expression for $s_o$ (Eq. 30), the same deflection curve should be obtained under different conditions of oven temperature, beam velocity, and field strength. Preliminary experiments on CsCl indicate that the deflection curve is the same if the temperature is changed and the experiment is run at constant velocity while varying the field strength. If the velocity is changed by at least 9%, and the experiment is run at constant temperature while varying the field strength, the deflection curve is again constant over the region investigated. It is estimated from the many series of deflection experiments performed in this thesis that the dipole moments determined are accurate to ±2%.

Alkali Halides. Experimental deflection curves were determined by deflecting beams of CsCl and RbCl under conditions of constant

velocity and temperature, and at different field strengths. CsCl and RbCl were chosen because accurate values of their equilibrium dipole moments are known from electric-resonance experiments,[16] and because velocity distribution and mass spectrometric experiments[22,39] have indicated the components present in the vapor phase for these compounds. Cesium chloride data was used for dipole determinations of cesium halides, and RbCl data was used for dipole determinations of rubidium halides and potassium halides. Rubidium chloride data was used for KI because the KCl results were complicated by a considerable amount of dimer at the operating velocity.[22] The CsCl curve and the RbCl curve differ slightly due to a change in the beam geometry. Experiments on molecules with known dipoles were performed before and after the "unknowns" in order to be sure that there were no systematic changes in geometry occurring.

Due to the fact that experimental deflection curves are used for dipole moment determinations, the effects of polarizability are expected to be negligible. This is expected since the differences in the polarizabilities of the molecules which are investigated, are not so great as to effect relative dipole moment determinations.[45] At the field strengths used, no polarizability effects are discernible. Table XVIII gives the results of calculations of alkali halide polarizabilities by Herschbach.[45]

Previous electric deflection studies[46] have indicated that all the lithium halide dimers are non-polar. It is assumed here that all the rubidium halide dimers and potassium halide dimers are non-polar, and will not be deflected. The fact that 1) the dipole moment

determinations of KCl from the RbCl data give results which are in good agreement with MBER results,[16] and 2) the fact that there is good internal consistency in the RbCl deflection experiments at different concentrations of $(RbCl)_2$, seems to justify this assumption. At the beam velocity and oven temperatures which were used for all of the deflection experiments, polymer corrections to the observed $I/I_o$ values were necessary for only RbCl and KCl. CsCl beams contain less than 2% dimer, and at a beam velocity of $6.06 \times 10^4$ cm/sec, no dimers are expected to be present in the beam.[22,39] Beams of the heavier Cs halides, CsBr and CsI, are expected to contain even less dimer, and dimer corrections were deemed unnecessary for these molecules also. The ratio of dimer to monomer, $a_2$, which was determined in this thesis, was used for the RbCl dimer corrections. A value of $a_2 = 0.079$ at 872°K for KCl was taken from the work of Miller and Kusch[22] in order to make dimer corrections for KCl. Corrections amounted to about 1/2% at $I/I_o = 0.806$ for RbCl, and about 2.75% at $I/I_o = 0.811$ for KCl. For KI, the results of Miller and Kusch[22] indicate that dimer corrections are unnecessary at the beam temperatures and velocity used here. Beams of the heavier Rb halides, RbBr and RbI, are expected to contain less dimer than RbCl under the present experimental conditions. Corrections for dimer were made using the following equation:

$$(I/I_o)_{\substack{\text{Corrected} \\ \text{for dimer}}} = (I/I_o)_{exp} \frac{1}{1 - f} - \frac{f}{1 - f}$$

where $f$ is the fraction of the total undeflected beam intensity which is dimer, and

$$f = 1 - \frac{1}{1 - 8\, a_2 \exp(-\nu^2/\alpha^2)}$$

Least squares fits of the RbCl and the CsCl data are represented in Fig. 20 by the solid and dashed curves, respectively. $I/I_o$ is the experimentally determined quantity, and $s_o$ is calculated from Eq. (34) by using the known mass and equilibrium dipole moments of CsCl and RbCl[16] and by using the measured values of the temperature, beam velocity, and deflecting field voltage. The solid line in Fig. 20 is also the theoretical curve which was calculated with the present assumed undeflected beam shape. Although the theoretical and experimental curves are very close, dipole moments were determined from the experimental deflection curves. For a particular experimental value of $I/I_o$, the corresponding $s_o$ value is determined from the appropriate experimental curve and the dipole is calculated from Eq. (34). The final results of the experiments are summarized in Tables XIX through XXVIII.

CsOH. Cesium hydroxide deflection data was taken with the same apparatus geometry which was set-up for RbCl. The beam profile which was assumed for the theoretical calculations in the linear case, gave theoretical $I/I_o$ vs $s_o$ curves which were in good agreement with experimental RbCl curves. Hence, it is expected that the linear triatomic model calculations, with this same assumed profile, would yield theoretical $I/I_o$ vs $s_o$ curves which are in good agreement with experimental deflection curves for a prototype linear triatomic molecule.

As in the alkali halide deflection experiments, the oven source used for CsOH had a 0.1778 cm wide slit. Rao and Schoonmaker,[28] in a velocity analysis of NaOH beams, indicated that creepage of beam material through the source slit appears to cause spurious results when conducting effusive studies with molten alkali hydroxides. Creepage of CsOH was observed in the present case. Hence, for reasons of wide slit width and beam creepage, no reliable information about the vapor species above molten CsOH could be expected from a velocity analysis of CsOH beams, under the present conditions. In order to make corrections for dimer, a value of $a_2 = 0.617$ for CsOH was calculated from the mass spectrometric results of Porter and Schoonmaker.[47] This number was calculated by using 1.75 as the relative ionization cross section of dimer to monomer.[39]

A high-temperature microwave spectroscopic investigation of CsOH has been previously reported.[48,49] The experimental results led the authors to conclude that CsOH is linear, at least in an average sense, although they could not conclude whether the equilibrium configuration is linear or not. From the above conclusions, it seemed likely that deflection data for CsOH would fit the linear triatomic model which was derived here.

When the linear triatomic model is used to interpret the experimental data for CsOH, and $s_o$ is calculated by using a CsOH dipole moment of 7.1 Debye (taken from the results of Lide and Kuczkowski),[48,49] the experimental deflection curve in Fig. 21 is obtained. The closest "fit" with the theoretical linear triatomic

model is obtained at a bending vibrational frequency of about 400 $cm^{-1}$, whereas Lide and Kuczkowski report a value of 300 ± 50 $cm^{-1}$. The differences in the slopes of the experimental and the theoretical curves cannot be accounted for by making the dimer correction with any value of $a_2$ when the dipole is varied between the upper and lower limits which are cited by Lide and Kuczkowski. According to the deflection results of Buchler, Stauffer, and Klemperer on $Cs_2(OH)_2$,[50] cesium hydroxide dimer is non-polar, and hence, the differences in the curves cannot be due to deflection of dimer molecules. Indeed, the CsOH configuration which was preferred by Lide and Kuczkowski when interpreting their microwave results, does not appear to be a suitable model for interpreting the present CsOH deflection data.

$LaF_3$. Crystalline $LaF_3$ was placed in a stainless steel tubular oven (of the type used for LiCl) and a suitable beam intensity was obtained at a temperature of about 1200°K. After selecting a beam velocity of $6.06 \times 10^4$ cm/sec, the deflecting field was turned on. No decrease in beam intensity was observed when the field strength was varied up to 8000 V/cm.

Electron diffraction experiments have indicated that the La trihalides have a planar symmetric structure.[51] Mass spectrometric studies have indicated that $LaF_3$ is the major vapor species above crystalline $LaF_3$.[52] The same oven and oven load that was used in the $LaF_3$ deflection experiment was placed in a quadrupole mass spectrometer, and $LaF_3$ was observed to be the major species under the present conditions. The absence of an observable decrease in the $LaF_3$ beam intensity in the

present experiment indicates that $LaF_3$ has a small or vanishing dipole moment. This result implies that $LaF_3$ has a planar or near planar structure.

Previous geometry studies on closely related sequences of molecules such as the alkaline earth dihalides (where some molecules are linear and some are bent), have revealed variations in molecular structure within the series[5,49,53] which were explained in terms of the simple polarizable ion model. Since electron diffraction experiments suffer some limitations when carried out at high temperatures,[54] it appeared worthwhile to reexamine the La halides by a different method. The simple polarizable ion model would predict that in the series of La halides, $LaF_3$ would be the most likely to assume a trigonal pyramidal shape, in contrast to a planar structure. For this reason, it was examined here.

Table XVIII. Polarizabilities of alkali halides.[45]

| Alkali Halide | Polarizability ($Å^3$) | Alkali Halide | Polarizability ($Å^3$) |
|---|---|---|---|
| LiF | 1.1 | RbF | 2.5 |
| LiCl | 3.7 | RbCl | 5.1 |
| LiBr | 4.8 | RbBr | 6.2 |
| LiI | 7.2 | RbI | 8.6 |
| NaF | 1.2 | CsF | 3.5 |
| NaCl | 3.9 | CsCl | 6.1 |
| NaBr | 5.0 | CsBr | 7.2 |
| NaI | 7.3 | CsI | 9.6 |
| KF | 1.9 | | |
| KCl | 4.5 | | |
| KBr | 5.7 | | |
| KI | 8.0 | | |

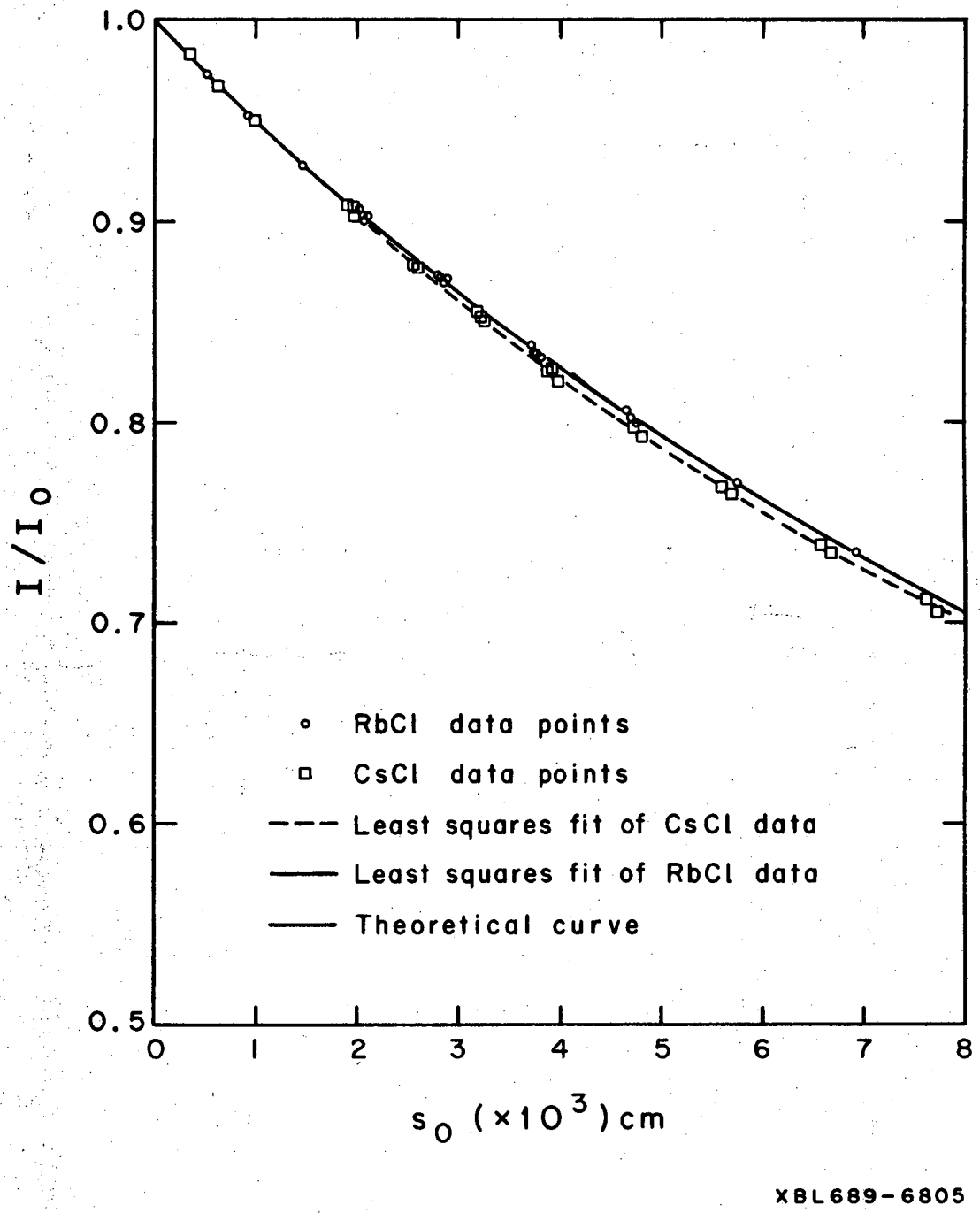


Fig. 20. Theoretical and experimental deflection curves for the diatomic model.

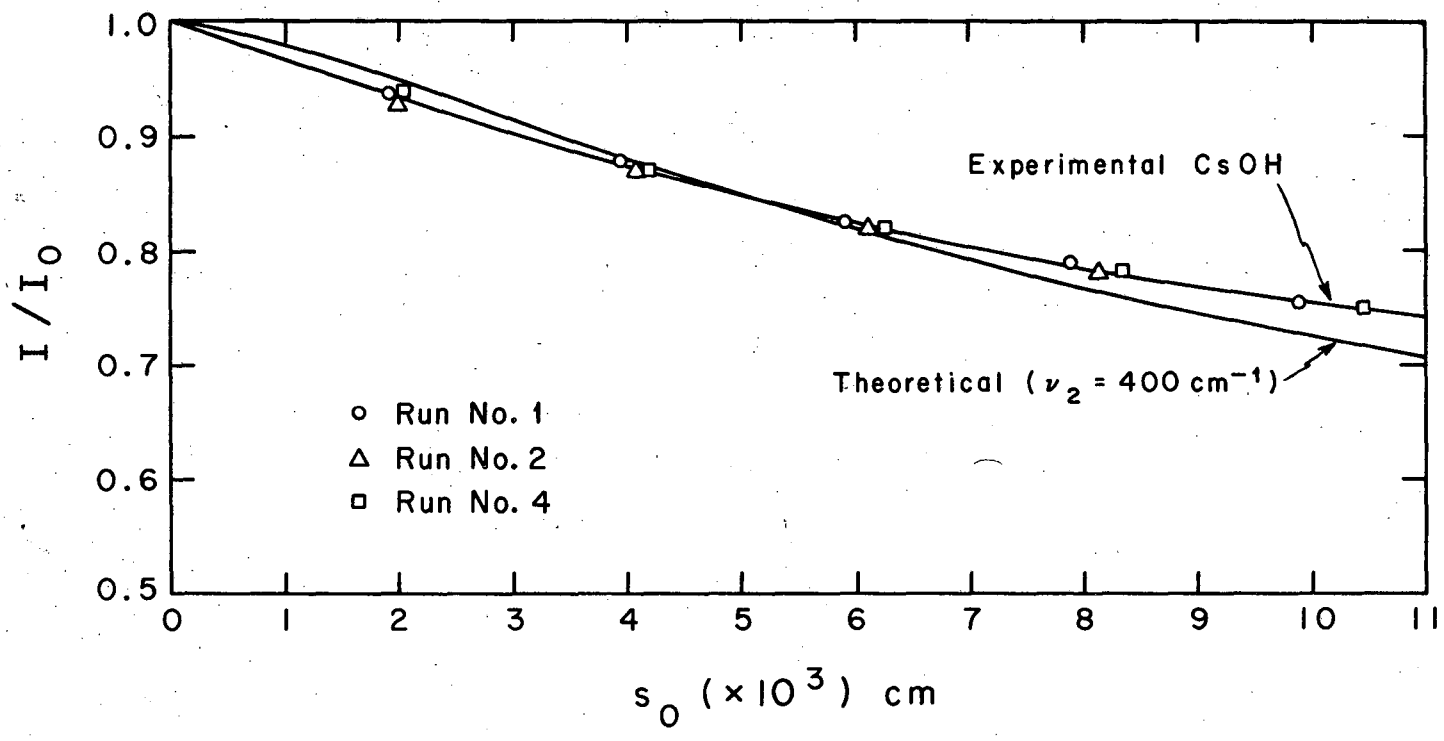


Fig. 21. Theoretical and experimental deflection curves for the linear triatomic model.

Table XIX. Summary of dipole moments (Debye units).

$\mu_e$ = equilibrium dipole moment

| | $\mu_e$ ionic model[1,2] | $\mu_e$ deflection exp. | Differences |
|---|---|---|---|
| | | From CsCl curve | |
| CsI | 11.53±0.2 | 11.69±0.1 | +0.16 |
| CsBr | 10.75±0.2 | 10.82±0.1 | +0.07 |
| | | From RbCl curve | |
| RbI | 11.36±0.2 | 11.48±0.2 | +0.12 |
| RbBr | 10.74±0.2 | 10.86±0.1 | +0.12 |
| KI | 10.99±0.2 | 10.82±0.1 | -0.17 |
| | $\mu_e$ MBER[16] | | |
| KCl | 10.238±0.001 | 10.18±0.2 | -0.06 |

Table XX. Cesium chloride deflection data.

| Run | Velocity (cm/sec) | T°K | Voltage (kV) | $I/I_o$ | $s_o$ ($10^3$ cm) |
|---|---|---|---|---|---|
| 3 | $6.06 \times 10^4$ | 857.4 | 1.506 | .982 | .356 |
| | | 857.4 | 2.008 | .967 | .634 |
| | | 858.0 | 2.520 | .950 | .997 |
| | | 857.4 | 3.520 | .906 | 1.947 |
| | | 857.4 | 4.050 | .877 | 2.578 |
| | | 857.4 | 4.530 | .852 | 3.225 |
| | | 857.4 | 5.000 | .827 | 3.929 |
| | | 856.7 | 5.490 | .798 | 4.740 |
| | | 858.2 | 5.970 | .768 | 5.595 |
| | | 858.2 | 6.470 | .739 | 6.572 |
| | | 858.2 | 6.960 | .712 | 7.605 |
| 9 | $6.06 \times 10^4$ | 845.9 | 3.520 | .903 | 1.974 |
| | | 845.9 | 4.050 | .878 | 2.613 |
| | | 845.6 | 4.530 | .850 | 3.270 |
| | | 845.6 | 5.000 | .821 | 3.983 |
| | | 845.6 | 5.490 | .793 | 4.802 |
| | | 845.6 | 5.970 | .764 | 5.679 |
| | | 846.0 | 6.470 | .735 | 6.667 |
| | | 846.0 | 6.960 | .706 | 7.715 |
| 12 | $6.06 \times 10^4$ | 870.7 | 3.520 | .907 | 1.917 |
| | | 870.7 | 4.050 | .878 | 2.538 |
| | | 870.7 | 4.530 | .855 | 3.175 |
| | | 870.7 | 5.000 | .826 | 3.869 |

Table XXI. Rubidium chloride deflection data.

| Run | Velocity (cm/sec) | T°K | Voltage (kV) | $I/I_o$ | $s_o$ ($10^3$ cm) |
|---|---|---|---|---|---|
| 3 | $6.06 \times 10^4$ | 842.1 | 3.000 | .904 | 2.063 |
| | | | 3.520 | .873 | 2.840 |
| | | | 4.050 | .837 | 3.759 |
| | | | 4.530 | .805 | 4.703 |
| 5 | $6.07 \times 10^4$ | 851.2 | 3.000 | .906 | 2.041 |
| | | | 3.520 | .875 | 2.809 |
| | | | 4.050 | .841 | 3.719 |
| | | | 4.530 | .809 | 4.653 |
| 6 | $6.07 \times 10^4$ | 828.6 | 3.000 | .903 | 2.089 |
| | | | 3.520 | .873 | 2.876 |
| | | | 4.050 | .836 | 3.808 |
| | | | 4.530 | .801 | 4.764 |
| 7,8,9 | $6.06 \times 10^4$ | 840.2 | 1.506 | .973 | .521 |
| | | | 2.008 | .953 | .926 |
| | | | 2.520 | .928 | 1.459 |
| | | | 3.000 | .903 | 2.067 |
| | | | 3.520 | .873 | 2.846 |
| | | | 4.050 | .837 | 3.768 |
| | | | 4.530 | .806 | 4.714 |
| | | | 5.000 | .773 | 5.743 |
| | | | 5.490 | .740 | 6.923 |

Table XXII. Dipole moment of cesium bromide calculated from cesium chloride deflection curve.

| T°K | Voltage (kV) | $I/I_o$ | $s_o$ ($10^3$ cm) | $\mu_e$ (Debye units) |
|---|---|---|---|---|
| | | Run #2 | | |
| | | $v = 6.06 \times 10^4$ cm/sec | | |
| 804.8 | 4.050 | .887 | 2.367 | 10.81 |
| 806.3 | 4.530 | .861 | 2.990 | 10.87 |
| 805.3 | 5.000 | .835 | 3.654 | 10.88 |
| 805.3 | 5.490 | .810 | 4.337 | 10.80 |
| | | Run #4 | | |
| | | $v = 6.06 \times 10^4$ cm/sec | | |
| 830.1 | 3.520 | .915 | 1.736 | 10.82 |
| 829.2 | 4.050 | .890 | 2.298 | 10.81 |
| 829.6 | 4.530 | .867 | 2.847 | 10.76 |
| 829.8 | 5.000 | .840 | 3.523 | 10.85 |
| 830.0 | 5.490 | .817 | 4.141 | 10.71 |

Table XXIII. Dipole moment of cesium iodide calculated from cesium chloride deflection curve.

| T°K | Voltage (kV) | $I/I_o$ | $s_o$ ($10^3$ cm) | $\mu_e$ (Debye units) |
|---|---|---|---|---|
| | | Run #2 | | |
| | | $v = 6.05 \times 10^4$ cm/sec | | |
| 851.2 | 3.520 | .919 | 1.649 | 11.78 |
| 851.2 | 4.050 | .896 | 2.160 | 11.72 |
| 850.1 | 4.530 | .872 | 2.722 | 11.75 |
| 850.1 | 5.000 | .849 | 3.291 | 11.71 |
| 849.8 | 5.490 | .824 | 3.949 | 11.68 |
| | | Run #7 | | |
| | | $v = 6.05 \times 10^4$ cm/sec | | |
| 853.6 | 3.520 | .921 | 1.606 | 11.64 |
| 852.9 | 4.050 | .897 | 2.137 | 11.67 |
| 853.2 | 4.530 | .874 | 2.674 | 11.67 |
| 853.4 | 5.000 | .849 | 3.291 | 11.73 |
| 853.6 | 5.490 | .825 | 3.921 | 11.66 |
| 854.1 | 5.970 | .799 | 4.652 | 11.68 |

Table XXIV. Dipole moment of rubidium bromide calculated from rubidium chloride deflection curve.

| T°K | Voltage (kV) | $I/I_o$ | $s_o$ ($10^3$ cm) | $\mu_e$ (Debye units) |
|---|---|---|---|---|
| | | Run #1, 2, 3 | | |
| | | $\nu = 6.06 \times 10^4$ cm/sec | | |
| 849.5 | 3.520 | .894 | 2.254 | 10.98 |
| | 4.050 | .867 | 2.921 | 10.86 |
| | 4.530 | .838 | 3.687 | 10.91 |
| | 5.000 | .810 | 4.482 | 10.90 |
| | | Run #4, 5, 6 | | |
| | | $\nu = 6.05 \times 10^4$ cm/sec | | |
| 871.1 | 3.520 | .898 | 2.159 | 10.88 |
| | 4.050 | .872 | 2.794 | 10.76 |
| | 4.530 | .844 | 3.524 | 10.80 |
| | 5.000 | .816 | 4.307 | 10.82 |

Table XXV. Dipole moment of rubidium iodide calculated from rubidium chloride deflection curve.

| T°K | Voltage (kV) | $I/I_o$ | $s_o$ ($10^3$ cm) | $\mu_e$ (Debye units) |
|---|---|---|---|---|
| | | Run #1, 2, 3 | | |
| | | $v = 6.06 \times 10^4$ cm/sec | | |
| 854.7 | 3.520 | .909 | 1.902 | 11.46 |
| | 4.050 | .881 | 2.570 | 11.58 |
| | 4.530 | .859 | 3.127 | 11.42 |
| | 5.000 | .830 | 3.909 | 11.57 |
| | | Run #4, 5, 6 | | |
| | | $v = 6.07 \times 10^4$ cm/sec | | |
| 890.2 | 3.520 | .912 | 1.833 | 11.50 |
| | 4.050 | .886 | 2.447 | 11.55 |
| | 4.530 | .866 | 2.946 | 11.33 |
| | 5.000 | .839 | 3.660 | 11.45 |

Table XXVI. Dipole moment of potassium iodide calculated from rubidium chloride deflection curve.

| T°K | Voltage (kV) | $I/I_o$ | $s_o$ ($10^3$ cm) | $\mu_e$ (Debye units) |
|---|---|---|---|---|
| | | Run #1, 2, 3 | | |
| | | $v = 6.06 \times 10^4$ cm/sec | | |
| 900.6 | 3.520 | .902 | 2.065 | 10.85 |
| | 4.050 | .873 | 2.769 | 10.92 |
| | 4.530 | .851 | 3.337 | 10.76 |
| | 5.000 | .825 | 4.049 | 10.73 |
| | | Run #4, 5, 6 | | |
| | | $v = 6.07 \times 10^4$ cm/sec | | |
| 911.3 | 3.520 | .902 | 2.065 | 10.93 |
| | 4.050 | .877 | 2.669 | 10.80 |
| | 4.530 | .853 | 3.284 | 10.76 |
| | 5.000 | .824 | 4.078 | 10.85 |

Table XXVII. Dipole moment of potassium chloride calculated from rubidium chloride deflection curve.

| T°K | Voltage (kV) | $I/I_o$ (corrected for dimer) | $s_o$ ($10^3$ cm) | $\mu_e$ (Debye units) |
|---|---|---|---|---|
| | | Run #1 $v = 6.06 \times 10^4$ cm/sec | | |
| 836.2 | 2.520 | .897 | 2.1827 | 10.058 |
| | 3.000 | .860 | 3.1009 | 10.070 |
| | 3.520 | .813 | 4.3939 | 10.216 |
| | | Run #2 $v = 6.07 \times 10^4$ cm/sec | | |
| 825.4 | 2.520 | .895 | 2.2303 | 10.109 |
| | 3.000 | .860 | 3.1009 | 10.013 |
| | 3.520 | .811 | 4.4523 | 10.225 |
| | | Run #3 $v = 6.06 \times 10^4$ cm/sec | | |
| 850.1 | 2.520 | .892 | 2.3021 | 10.414 |
| | 3.000 | .859 | 3.1269 | 10.196 |
| | 3.520 | .817 | 4.2778 | 10.163 |
| | | Run #4 $v = 6.07 \times 10^4$ cm/sec | | |
| 865.3 | 2.520 | .896 | 2.2065 | 10.295 |
| | 3.000 | .862 | 3.0491 | 10.166 |
| | 3.520 | .819 | 4.2203 | 10.193 |

Table XXVIII. Cesium hydroxide deflection data.

| Run | Velocity (cm/sec) | T°K | Voltage (kV) | $I/I_o$ | $s_o$ ($10^3$ cm) |
|---|---|---|---|---|---|
| 1 | $6.06 \times 10^4$ | 777.7 | .4885 | .937 | 1.916 |
| | | | 1.004 | .878 | 3.938 |
| | | | 1.506 | .825 | 5.907 |
| | | | 2.008 | .790 | 7.876 |
| | | | 2.520 | .754 | 9.884 |
| 2 | $6.07 \times 10^4$ | 724.8 | .4885 | .928 | 1.978 |
| | | | 1.004 | .869 | 4.066 |
| | | | 1.506 | .820 | 6.099 |
| | | | 2.008 | .781 | 8.132 |
| 4 | $6.06 \times 10^4$ | 694.9 | .4885 | .937 | 2.027 |
| | | | 1.004 | .870 | 4.166 |
| | | | 1.506 | .821 | 6.249 |
| | | | 2.008 | .782 | 8.332 |
| | | | 2.520 | .751 | 10.456 |

## APPENDIX

List of Drawings for Velocity Selector*

| | | |
|---|---|---|
| 1. | Bearing housing | 14K1302A |
| 2. | Rotor shaft | 14K1344A |
| 3. | Locking nut | 14K1292A |
| 4. | Motor mount - A | 14K5183 |
| 5. | Spacer | 14K1333 |
| 6. | End spacer | 14k1312 |
| 7. | Alignment blocks | 14K1323 |
| 8. | Slotted disk | 14J9363A |
| 9. | Frame | 14K5174 |

*These drawings are on file at the Lawrence Radiation Laboratory.

ACKNOWLEDGMENTS

I would like to thank Professor Kenneth Street, Jr. for his helpful guidance and encouragement throughout the course of this work.

The advice and assistance of Drs. Alvin J. Hebert and Carlos A. Melendres was especially helpful in the experimental work.

To my parents, I would like to express my deepest appreciation for their help and encouragement throughout the years.

This work was performed under the auspices of the U. S. Atomic Energy Commission.

REFERENCES

1. K. Street, Jr. (unpublished).
2. K. Street, Jr., C. D. Hollowell, and F. J. Lovas (unpublished).
3. I. Estermann and R. G. J. Fraser, J. Chem. Phys. 1, 390 (1933).
4. W. H. Rodebush, L. A. Murray, Jr., and M. E. Bixler, J. Chem. Phys. 4, 372 (1936).
5. A. Buchler, J. L. Stauffer, W. Kelmperer, and L. Wharton, J. Chem. Phys. 39, 2299 (1963).
6. A. J. Hebert, A Molecular-Beam Electric-Resonance Spectrometer and the Radio-Frequency Spectra of Lithium Fluoride (Ph.D. Thesis), UCRL-10482, September 1962.
7. N. F. Ramsey, Molecular Beams (Clarendon Press, Oxford, 1956).
8. P. Kusch and V. W. Hughes, "Atomic and Molecular Beam Spectroscopy," in Handbuch der Physik, ed. by S. Flugge, 37/1 (Springer-Verlag, Berlin, 1959).
9. F. W. Breivogel, Jr., The Radio-Frequency and Microwave Spectra of LiBr and LiI (Ph.D. Thesis), UCRL-11665, September 1964.
10. W. Klemperer, W. G. Norris, A. Buchler, and A. G. Emslie, J. Chem. Phys. 33, 1534 (1960).
11. J. L. Dunham, Phys. Rev. 41, 721 (1932).
12. D. T. F. Marple and J. W. Trischka, Phys. Rev. 103, 597 (1956).
13. D. R. Lide, Jr., P. Cahill, and L. P. Gold, J. Chem. Phys. 40, 156 (1964).
14. L. P. Gold (Ph.D. Thesis), Department of Chemistry, Harvard University, Cambridge, Massachusetts, November 1961.

15. N. F. Ramsey, Ref. 7, p. 80.

16. A. J. Hebert, F. J. Lovas, C. A. Melendres, C. D. Hollowell, T. L. Story, Jr., and K. Street, Jr., J. Chem. Phys. 48, 2824 (1968).

17. R. K. Bauer and H. Lew, Can. J. Phys. 41, 1461 (1963); R. K. Bauer and H. Lew, Can. J. Phys. 42, 830 (1964); G. Graff and G. Werth, private communication, 1964.

18. Ch. Schlier, Zeitschrift für Physik 154, 460 (1959).

19. T. C. Wang, C. H. Townes, A. L. Schawlow, and A. N. Holden, Phys. Rev. 86, 809 (1952).

20. Marple and Trischka, Ref. 12, p. 610.

21. R. C. Miller and P. Kusch, Phys. Rev. 99, 1314 (1955).

22. R. C. Miller and P. Kusch, J. Chem. Phys. 25, 860 (1956).

23. N. F. Ramsey, Ref. 10, pp. 11-50.

24. A. N. Nesmeyanov, Vapor Pressure of the Chemical Elements (Elsevier Publishing Company, New York, 1963), pp. 47-52.

25. C. I. Whitman, J. Chem. Phys. 20, 161 (1952).

26. C. I. Whitman, J. Chem. Phys. 21, 1407 (1953).

27. R. S. Bradley and P. Volans, Proc. Roy. Soc. (London) 217, 508 (1953).

28. V. S. Rao and R. C. Schoonmaker, J. Chem. Phys. 33, 1718 (1960).

29. H. U. Hostettler and R. B. Berstein, Rev. Sci. Instr. 31, 872 (1960).

30. S. M. Trujillo, P. K. Rol, and E. W. Rothe, Rev. Sci. Instr. 33, 841 (1962).

31. A. E. Grosser, Rev. Sci. Instr. 38, 257 (1967).

32. J. G. Dash and H. S. Sommers, Jr., Rev. Sci. Instr. 24, 91 (1953).

33. M. Eisenstadt, G. M. Rothberg, and P. Kusch, J. Chem. Phys. 29, 797 (1958).

34. M. A. Platkov and S. V. Illarionov, Pribory i Tekhnika 'Eksperimenta 2, 133 (1962).

35. J. L. Kinsey, Rev. Sci. Instr. 37, 61 (1966).

36. E. E. Bisson and W. J. Anderson, Advanced Bearing Technology (NASA, Washington, D. C., 1964), pp. 259-285.

37. T. Baumeister, Mechanical Engineer's Handbook (McGraw-Hill Book Company, Inc., New York, 1958), 6th edition, pp. 5-106.

38. P. Kusch, J. Chem. Phys. 28, 1075 (1958).

39. J. Berkowitz and W. A. Chupka, J. Chem. Phys. 29, 653 (1958).

40. R. G. J. Fraser, Molecular Rays (University Press, Cambridge, 1931) pp. 154-169.

41. Ramsey, Ref. 7, pp. 18, 19.

42. Kusch and Hughes, Ref. 8, pp. 18, 19.

43. C. H. Townes and A. L. Schawlow, Microwave Spectroscopy (McGraw-Hill Book Company, Inc., New York, 1955), pp. 31-35.

44. Townes and Schawlow, Ref. 43, pp. 248-283.

45. R. R. Herm and D. R. Herschbach, Inhomogeneous Electric Deflecting Field for Analysis of Rotational Excitation in Reactive Scattering of Molecular Beams, UCRL-16039, July 1965.

46. A. Buchler, J. L. Stauffer, and W. Klemperer, J. Phys. Chem. 86, 4544 (1964).

47. R. C. Schoonmaker and R. F. Perter, J. Chem. Phys. 31, 830 (1959).

48. R. L. Kuczkowski, D. R. Lide, and L. C. Krisher, J. Chem. Phys. 44, 3131 (1966).

49. D. R. Lide and R. L. Kuczkowski, J. Chem. Phys. 46, 4768 (1967).

50. A. Buchler, J. L. Stauffer, and W. Klemperer, J. Chem. Phys. 46, 605 (1967).

51. P. A. Akishin, V. A. Naumov, and V. M. Tatevskii, Vestnik Moskov. Univ., Ser. Mat., Mekh., Astron., Fiz., Khim. 14, 229 (1959); P. A. Akishin and V. A. Naumov, Nauch. Doklady Vysshei Shkoly, Khim. i Khim. Tekhnol. No. 1, 5 (1959).

52. R. W. Mar and A. W. Searcy, J. Inorg. Nucl. Chem. 28, 1419 (1966).

53. L. Wharton, R. A. Berg, and W. Klemperer, J. Chem. Phys. 39, 2023 (1963).

54. D. E. Mann, G. V. Calder, K. S. Seshadri, D. White, and M. J. Linevsky, J. Chem. Phys. 46, 1138 (1967).

55. F. J. Lovas, Radio-Frequency Stark Spectra of RbF, RbCl, CsF, CsCl, and NaI (Ph.D. Thesis), UCRL-17909, November 1967.

56. C. A. Melendres, Radio-Frequency Stark Spectra of NaCl, NaBr, and BaS by the Molecular-Beam Electric-Resonance Method (Ph.D. Thesis), UCRL-18344, June 1968.